NANOPORE ARCHITECTURE AND ELASTIC VELOCITIES IN THE MISSISSIPPIAN-AGE CARBONATE-SILICICLASTIC RESERVOIRS OF THE US MID-CONTINENT

By

ROHIT RAJ

Integrated Master of Technology in
Geophysical Technology
Indian Institute of Technology Roorkee
Roorkee, Uttarakhand, India
2016

Submitted to the Faculty of the
Graduate College of the
Oklahoma State University
in partial fulfillment of
the requirements for
the Degree of
DOCTOR OF PHILOSOPHY
December, 2021

NANOPORE ARCHITECTURE AND ELASTIC VELOCITIES IN THE MISSISSIPPIAN-AGE CARBONATE-SILICICLASTIC RESERVOIRS OF THE US MID-CONTINENT

Dissertation Approved:

Dr. Priyank Jaiswal

Dissertation Adviser

Dr. G. Michael Grammer

Dr. James O. Puckette

Dr. Prem Kumar Bikkina

ACKNOWLEDGEMENTS

I express my sincere gratitude to my Ph.D. advisor and chair, Dr. Priyank Jaiswal, for introducing and guiding me in frontier projects throughout my Ph.D. I thank him for his patience, support, encouragement, advice, and belief in me.

I thank my committee members Dr. G. Michael Grammer, Dr. James O. Puckette, and Dr. Prem Kumar Bikkina for their guidance and support during my Ph.D. I am thankful to Boone Pickens School of Geology faculty and staff, and in particular, Dr. Mohamed Abdelsalam (Graduate Coordinator) and Dr. Camelia Knapp (Head of Department) without their support this degree would not have been possible.

I thank Dr. Ralf Weger (University of Miami) for his invaluable mentoring during my visit. I also thank Beth Vanden Berg (Ph.D.) and Yulun Wang (Ph.D.) for their technical assistance.

I am grateful to Khemraj Shukla (Ph.D.), Salman, Sundeep, and Avinash for their constant guidance, various discussions, and technical pointers; and to the wonderful lab and department colleagues - Md Iftekhar Alam (Ph.D.), Afshin Aghayan (Ph.D.), Micah, Nathan, Brandon, Luel, Leye, and Kevin.

I extend my sincere thanks to my friends for their untiring support, throughout and especially during the toughest times during my Ph.D. Particularly, I express my cordial gratitude to Prakash, Thakur, Dr. Bhandari, Harsh, and Ayush for their unparalleled presence and encouragements; and Ayan, Surya, Vernon, Ajeeth, Mishra, Ali, and Vishesh for making Stillwater joyful.

Finally, I would like to thank my family for their unconditional understanding and countless sacrifices, without which this journey would not have started and was not possible.

Name: ROHIT RAJ

Date of Degree: DECEMBER, 2021

Title of Study: NANOPORE ARCHITECTURE AND ELASTIC VELOCITIES IN THE MISSISSIPPIAN-AGE CARBONATE-SILICICLASTIC RESERVOIRS OF THE US MID-CONTINENT

Major Field: GEOLOGY

Abstract: The overarching research objective of this dissertation is to understand the effect that nanopore distribution has on elastic velocities in a geological setting. The study is conducted on the Mississippian-age "Miss Lime" and Meramec rocks that constitute an unconventional reservoir system in the Sooner Trend, Anadarko, Canadian, and Kingfisher (STACK) play of the US mid-continent. These reservoirs are low porosity (ϕ), low permeability (κ) and are compositionally mixed carbonate-siliciclastic with sporadic clay abundance. Multiple sediment deposition episodes coupled with diagenesis and tectonics that has resulted in lateral and vertical facies and composition variability and created various pore-types of different shapes and geometries, that dominate and obscures/complicates diagnostic rock relationships, e.g., inverse ϕ–P-wave velocity (V_P). This dissertation explores how pore architecture influences the elastic velocities in these reservoirs.

The working hypothesis is that pore becomes increasingly isolated as pore-size decreases and at nanopore scale (10^{-9}-10^{-6} m), an increase in the confining stress, due to seismic wave propagation or geology, causes a dynamic increase in the elastic modulus of the fluid trapped in the nanopores. A dual goal of this research is to study the effects clay diagenesis has on elastic velocities and build predictive models. The hypothesis testing and the dual goal is achieved using a set of laboratory-measured properties comprising of X-ray diffraction-based mineralogy, bulk ϕ from He-gas porosimetry, dry ultrasonic elastic velocities, and pore architectural parameters (area, perimeter, length, and width) generated from photomicrographs using digital image analysis; and well-logs (density porosity, neutron porosity, compressional and shear sonic).

Finding suggests that (1) V_P increases as dominant pore-size decreases within samples belonging to same facies and composition subgroups; and pore-size plays a dominant role in influencing V_P and shows a better trend with V_P than ϕ in Miss Lime reservoir; (2) V_P pressure-sensitivity increases with a decrease in dominant pore size in the nanopore scale in the complex pore and fracture free samples belonging to similar facies and pore-shape distribution groups in Meramec reservoir; and (3) clay-diagenesis based physics-driven model explains all the elastic velocities under saturated and dry conditions in a Meramec reservoir well.

TABLE OF CONTENTS

Chapter Page

Chapter Page

LIST OF TABLES

LIST OF FIGURES

Figure Page

Paper 1

CHAPTER I

INTRODUCTION

1.1 Research Motivation

The Sooner Trend, Anadarko, Canadian, and Kingfisher (STACK) play in the Anadarko Basin is comprised of unconventional tight oil and gas producing reservoirs in the US mid-continent. Among all, the Mississippian-age "Miss Lime" and Meramec reservoirs are unconventional mixed carbonate-siliciclastic systems in the STACK play that are the prospective target for production by different operators. They are predominantly low porosity (ϕ) and low permeability (κ) reservoir system that shows high lateral and vertical variability in the reservoir facies and production capabilities (Childress and Grammer (2017), Price and Grammer (2017), Price and Grammer, (2019), Vanden Berg and Grammer (2016)). A series of coupled depositional, diagenesis, and tectonic events shaped these reservoirs that led to compositional as well as pore-type variability (Buggisch et al. (2008), Childress and Grammer (2015), Haq and Schutter (2008), Mazzullo et al. (2011), Price et al. (2017), Watney et al. (2001), Vanden Berg and Grammer (2016)), that obscured diagnostic relationships, e.g., inverse linear ϕ–P-wave velocity (V_P) (Vanden Berg et al. (2018)).

From elementary rock physics, V_P is primarily driven by the changes in grain composition and porosity. Different grain minerals have different elastic moduli that proportionately and directly change V_P, e.g., clay in carbonate or sandstone rocks reduces V_P given ϕ remains the same (Mavko

et al. (2020)). V_P increases as the pore volume decreases from its critical value. Pore volume decrease could happen due to either solid occluding the pore volume, or due to a reduction in pore size during deposition and compaction. Besides, other factors also greatly or proportionately influence V_P, e.g., cement (Avseth et al. (2000)), Dvorkin and Nur (1996)), sorting (Xu and Payne (2009)) and pore architecture (Weger et al. (2009), Verwer et al. (2010)). In Mississippian-age mid-continents rocks, Vanden Berg and Grammer (2016) showed that pore-type distribution could be an influencing factor on V_P. Most recently, Vanden Berg et al. (2018) highlighted that ϕ-V_P relation is modified in micro-to-nanopore (1-62.5 μm to 1nm-1μm [Loucks et al. (2012)]) dominated system, and deviates from the inverse linear trend with large scatter. Understanding in what way and how pore architecture influences V_P is a knowledge gap addressed in this dissertation.

The hypothesis in this dissertation is that pores become progressively isolated due to decrement in pore size as a result of which nanopores remain largely unconnected. Seismic wave-induced pressure causes a dynamic increase in the bulk modulus of the fluid in a response to the stress field, which consequently increases V_P. A dual goal of this dissertation focuses on understanding the effects that clay diagenesis has on the elastic velocities (V_P, V_{S1}, and V_{S2}) and build geology, physics, and mathematical-based predictive models that explain it. A set of laboratory-based measurements on rock samples that includes composition from X-ray diffractometry, helium gas ϕ, ultrasonic elastic velocities (V_P, V_{S1}, and V_{S2}) under dry condition, pore architectural parameters (pore area, perimeter, length, and width) obtained from the digital image analysis of photomicrographs, and borehole measured well log (neutron porosity, density porosity, compressional and shear sonic slowness) are used to test the hypothesis and the dual objective. Simultaneous visualization of the pore architectural parameters using 2D contoured histogram crossplots are used in understanding and exploring the relationship between pore size and V_P, and rock physics-based models are used in transforming composition, ϕ and well log information into predictive velocity models.

1.2 Objectives

The overarching objectives of this research are as follows:

- Study the effect of pore-size distribution on V_P.
- Study how nanopores influence V_P pressure sensitivity.
- Study the effect of clay diagenesis and build a predictive velocity model using physical properties measured on the core and logs.

The above objectives were accomplished through three research projects. Outcomes of these projects were peer-reviewed publications in reputed journals which are listed as follows:

- Raj, R., Jaiswal, P., Vanden Berg, B., & Grammer, G.M. (2019). Pore Size and Ultrasonic Velocity: Lessons from Miss Lime Reservoirs. SEPM (Society for Sedimentary Geology), 18(2), 183-195. DOI: 10.2110/sepmsp.112.04
- Raj, R., Jaiswal, P., Wang, Y., Grammer, G.M., & Weger, R.J. (2021). How Nanopores Influence Dry Frame V_P Pressure Sensitivity. Frontiers in Earth Science: 9:641815, pp. 89. DOI: 10.3389/feart.2021.641815
- Raj, R., & Jaiswal, P. (2021). Clay diagenesis in Meramec Formation, Oklahoma: Insights from rock physics modeling. In *First International Meeting for Applied Geoscience & Energy* (pp. 2358-2362). Society of Exploration Geophysicists. DOI: 10.1190/segam2021-3584548.1

1.3 Chapter Outline

Chapters of this dissertation are organized as follows. Chapter II describes how pore size distribution could drive V_P. Laboratory-based measurements on core plugs were used to compile a database comprised of mineralogical composition, porosity, ultrasonic elastic velocities (V_P and V_S), and facies interpretation. A thin portion cut-out from an end of the core plugs was used in the light microscope (LM) and scanning electron microscope (SEM) photomicrography to image pores. Then, digital image processing of LM and SEM photomicrographs was done to generate pore size

information. A hierarchical analysis of samples based on the same facies and composition subgroups revealed an increment in V_P when dominant pore size decreases. The chapter highlights that pore size can play a dominant role in V_P and could show a better trend than ϕ.

Chapter III describes how nanopores influence dry-frame V_P pressure sensitivity. For this study, different laboratory experiments were conducted on core plugs to create a database consisting of mineralogical composition, facies interpretation, He-gas porosity (Φ_{He}), and dry-frame ultrasonic V_P and V_S. A thin portion cut-out from the core plugs were used for SEM photomicrography. Individual pore shape and size information was acquired through digital image analysis of these photomicrographs, that showed the bulk of the pores in the nanopore range (10^{-9}-10^{-6} m). A fracture and complex pore-free hierarchical analysis unveiled that pressure sensitivity of V_P increased with a decrement in dominant pore size within similar facies and pore-shape distribution groups. Chapter details out possible causative mechanisms and proposes the use of a dual-fluid model in modeling V_P.

Chapter IV focuses on unraveling the role and effect of clay diagenesis (smectite-to-illite transformation) on the elastic velocities under saturated and dry conditions. A common physics-driven model based on Gassmann (1951) fluid substituted constant-cement model (Dvorkin et al. (2021)) was used to model and explain all the elastic velocities under both saturation conditions. The chapter highlights how a common rock physics model could be used to explain a geological process instead of the end products.

Chapter V summarizes the research presented in chapters II-IV of this dissertation with prospective scope for future work.

1.4 References

Avseth P, Dvorkin J, Mavko G, Rykkje J. 2000. Rock physics diagnostic of North Sea sands: Link between microstructure and seismic properties. Geophysical Research Letters 27:2761–2764.

Buggisch, W., Joachimski, M. M., Sevastopulo, G., and Morrow, J. R., 2008, Mississippian $\delta^{13}C_{carb}$ and conodont apatite $\delta^{18}O$ records—their relation to the Late Palaeozoic Glaciation: Palaeogeography, Palaeoclimatology, Palaeoecology, v. 268, no. 3-4, p. 273-292.

Childress M, Grammer GM. 2015. High resolution sequence stratigraphic architecture of a Mid-Continent Mississippian outcrop in southwest Missouri. Shale Shaker 66:206–234.

Childress M, Grammer GM. 2017. Characteristics of debris flows and outrunner blocks—Evidence for Mississippian deposition on a distally steepened ramp. In Grammer GM, Gregg JM, Puckette JO, Jaiswal P, Mazzullo SJ, Pranter MJ, Goldstein RH (Editors). Mississippian Reservoirs of the Midcontinent, Memoir 116: American Association of Petroleum Geologists, Tulsa, Oklahoma.

Dvorkin, J. and Nur, A., 1996. Elasticity of high-porosity sandstones: Theory for two North Sea data sets. *Geophysics*, *61*(5), pp.1363-1370.

Dvorkin, J., Walls, J., and Davalos, G., 2021, Velocity-Porosity-Mineralogy Model for Unconventional Shale and Its Applications to Digital Rock Physics: Frontiers in Earth Science, v. 8, p. 654.

Gassmann, F., 1951, Uber die elastizitat poroser medien: Vierteljahrsschrift der Naturforschenden Gesellschaft in Zurich, v. 96, p. 1-23.

Haq, B. U., and Schutter, S. R., 2008, A chronology of Paleozoic sea-level changes: Science, v. 322, no. 5898, p. 64-68.

Loucks, R.G., Reed, R.M., Ruppel, S.C. and Hammes, U., 2012. Spectrum of pore types and networks in mudrocks and a descriptive classification for matrix-related mudrock pores. *AAPG bulletin*, *96*(6), pp.1071-1098.

Mavko, G., Mukerji, T. and Dvorkin, J., 2020. The rock physics handbook. Cambridge university press.

Mazzullo, S. J., Wilhite, B. W., and Boardman II, D. R., 2011, Lithostratigraphic architecture of the Mississippian reeds spring formation (middle Osagean) in southwest Missouri, northwest Arkansas, and northeast Oklahoma: Outcrop analog of subsurface petroleum reservoirs.

Price B. J., Grammer G.M., 2017. High resolution sequence stratigraphic architecture and reservoir characterization of the Mississippian Burlington/Keokuk Formation, northwestern Arkansas. In Grammer GM, Gregg JM, Puckette JO, Jaiswal P, Mazzullo SJ, Pranter MJ, Goldstein RH (Editors). Mississippian Reservoirs of the Midcontinent, Memoir 116: American Association of Petroleum Geologists, Tulsa, Oklahoma.

Price, B.J., Haustveit, K., and Lamb, A., 2017. Influence of Stratigraphy on Barriers to Fracture Growth and Completion Optimization in the Meramec Stack Play, Anadarko Basin, Oklahoma, *in* Proceedings Unconventional Resources Technology Conference, Austin, Texas, 24-26 July 2017, Society of Exploration Geophysicists, American Association of Petroleum Geologists, p. 3453-3460.

Price, B.J., and Grammer, G.M., 2019. High-resolution sequence stratigraphic architecture and reservoir characterization of the Mississippian Burlington-Keokuk Formation, northwestern Arkansas, In Grammer G.M., Gregg J.M., Puckette J.O., Jaiswal P., Mazzullo S.J., Pranter M.J., Goldstein R.H. (Editors), Mississippian Reservoirs of the Midcontinent: AAPG Memoir 122, p. 179–206.

Vanden Berg BV, Grammer GM. 2016. 2-D pore architecture characterization of a carbonate mudrock reservoir: Insights from the Mid-Continent ‘‘Mississippi Lime.’’ In Olson T (Editor). Imaging Unconventional Reservoir Pore Systems, Memoir 112: American Association of Petroleum Geologists, Tulsa, Oklahoma. p. 185–231.

Vanden Berg, B., Nussbaumer, C., Noack, A., Thornton, J., Weger, R. J., Eberli, G. P., and Grammer, G. M., 2018, A comparison of the relationship between measured acoustic response and porosity in carbonates across different geologic periods, depositional basins, and with variable mineral composition: Interpretation, v. 6, no. 2, p. T245-T256.

Watney, W. L., Guy, W. J., and Byrnes, A. P., 2001, Characterization of the Mississippian chat in south-central Kansas: AAPG bulletin, v. 85, no. 1, p. 85-113.

Weger, R.J., Eberli, G.P., Baechle, G.T., Massaferro, J.L. and Sun, Y.F., 2009. Quantification of pore structure and its effect on sonic velocity and permeability in carbonates. *AAPG bulletin*, *93*(10), pp.1297-1317.

Verwer, K., Eberli, G., Baechle, G. and Weger, R., 2010. Effect of carbonate pore structure on dynamic shear moduli. *Geophysics*, *75*(1), pp.E1-E8.

Xu, S. and Payne, M.A., 2009. Modeling elastic properties in carbonate rocks. *The Leading Edge*, *28*(1), pp.66-74.

CHAPTER II

PORE SIZE AND ULTRASONIC VELOCITY: LESSONS FROM MISS LIME RESERVOIRS

2.1 Abstract

This article investigates the relationship between rock properties (composition, porosity, and pore architecture) and dry ultrasonic P-wave velocity (V_P) of 14 samples representing three facies of the Mid-Continent Mississippian-age Limestone (Miss Lime) units of North–Central Oklahoma. Generally, in carbonate rocks, what drives V_P, in addition to bulk porosity (ϕ) and composition, is not straightforward to determine. In this data set, when samples are categorized based on their facies and composition (quartz fraction), V_P shows a better trend with dominant pore size rather than ϕ. Results show the dependence of elastic properties on texture and highlight a need for incorporating pore-size distribution in seismic models used for seismic interpretation of low-permeability reservoirs such as the Miss Lime.

Key Words: unconventional carbonate reservoir, digital image analysis, pore size, ultrasonic velocity

2.2 Introduction

The Mississippian-age limestone (Miss Lime) rocks are low porosity (ϕ) and low permeability (κ) mixed carbonate–siliciclastic reservoirs and represent a valuable exploration target

in the US Mid-Continent. Just between northern Oklahoma to southern Kansas, the Miss Lime play presents approximately 30 million acres of area that potentially contains up to 31 Million barrels (MMB) of oil equivalent and 663 billion cubic feet (BCF) of gas-in-place for drilling and resource development (Higley et al. 2014). Although Miss Lime's presence and distribution have been well known from decades of vertical drilling into its highly altered zones (Rogers 2001; Matson 2013, 2015), it is only in the past decade that its exploration has spiked (Evans and Newell 2013). Due in part to the perceived potential of their petroleum system and in part to the success of horizontal drilling technology in other tight rock plays, Miss Lime was initially seen as a ''high-reward'' target. However, soon after the exploration began, the realization that well-to-well water cut and payzone thickness variations can be severe also labeled Miss Lime as a ''high-risk'' target (Vandervoort 2011; Dick 2012; Watney 2014, 2015). After a brief hiatus following the 2014 oil downturn, interest in Miss Lime exploration has seen a cautious revival in tandem with operators trying to gain a better appreciation of its heterogeneity.

The exploration challenges in the Miss Lime are in part reflective of the general nature of uncertainties associated with the seismic exploration of carbonate systems worldwide. Presently, about half the world's oil and gas is produced from carbonate rocks (Roehl and Choquette 2012), but appreciation of their seismic response remains limited, largely due to difficulties in accounting for their complex composition and fabric in elastic/acoustic modeling (Doyen 2007, Xu and Payne 2009, Vanden Berg et al. 2018). In addition to the bulk of carbonate rocks being organically created, which induces heterogeneity in their primary facies, diagenesis continues to alter their pore structure, all of which often result in non-intuitive reservoir architecture (Wardlaw 1976, Ahr 2011). As carbonate systems get tighter (as ϕ and κ decreases) and as their composition becomes more heterogeneous, their elastic response also becomes more and more difficult to interpret (Todorovic-Marinic et al. 2011, Reijenstein et al. 2014, Rashid et al. 2017). The Miss Lime is an example of such a reservoir type.

From vintage surface and subsurface data, the Miss Lime reservoirs are broadly interpreted to have been created through the interaction of deposition and diagenesis with eustasy (Elrick and Read 1991, Elebiju et al. 2011, Mazzullo et al. 2011), along with sporadic alterations from basinal hydrothermal fluids (Jaiswal et al. 2017). Newer core data and analytical techniques have recently brought to light the role of high frequency sea-level changes (probable Milankovitch band) in shaping the Miss Lime reservoir architecture and their facies distribution (Wilson et al. 2017). This is relevant to exploration because higher ϕ–κ zones in Miss Lime seem to be tied to their facies, which change rapidly both laterally and vertically (Childress and Grammer 2017, Price and Grammer 2017). This might seemingly also imply that Miss Lime exploration can be readily achieved through seismic methods, as seismic data are sensitive to both facies (compositional heterogeneity and grain arrangement) and ϕ. However, this is not completely true. Seismically mapping facies in carbonate systems in general (Gao 2011), and in Miss Lime in particular (Yenugu et al. 2010, Turnini et al. 2017), has been possible to an extent, but inferring ϕ has been extremely difficult. This is likely because deviation of pore architecture in carbonates from uniform and simple geometries, which is typical of siliciclastic systems, deviates ϕ–dry ultrasonic P-wave velocity (V_P) relation from the simple trends (e.g., Wyllie et al. [1956] and Wood [1941]) that are routinely used in quantitative seismic interpretation (Eberli et al. 2003, Baechle et al. 2006).

Vanden Berg et al. (2018) have shown that ϕ–V_P relation in a rock becomes more and more difficult to interpret as pore sizes start to vary widely (e.g., from macro [>4-mm] to nano [<1-μm] pore ranges in the Miss Lime). In particular, their findings, which also build upon the work of Vanden Berg and Grammer (2016), regarding Miss Lime pore characteristics relevant to this article are as follows. First, they correlated variations in pore sizes to scatter in V_P, indicating that pore distribution might play a strong role in determining elastic velocities in the Miss Lime. Second, they found that different Miss Lime facies have different diagenetic fingerprints. They attributed the pore network evolution within individual facies to localized diagenesis, implying that the pore-

size distribution in Miss Lime is facies dependent, and, finally, they indicated that low V_P in the Miss Lime does not necessarily imply high bulk ϕ, which also happens to be Miss Lime's main exploration conundrum.

Composition and ϕ are nominally considered to be the two most important driving factors for elastic velocities. However, an evolving understanding of the subject shows that a number of other factors, such as sorting (Xu and White 1995), cementation (Avseth et al. 2000), and pore architecture (Weger et al. 2009), can exert equally or more significantly influence V_P. The possibility of other, previously unemphasized driving factors always exists. To develop a rock specific elastic model, the hierarchy of its driving factors (i.e., which dominates over others and to what extent) needs to be understood. The lack of such information is the main knowledge gap in term of Miss Lime. For example, it is not known to what extent pore architecture influences V_P over bulk ϕ or composition and whether there are other factors that should also be considered. This article begins to address that knowledge gap using a small rock property database comprising ϕ, composition, and pore architectural elements (perimeter [P], area [A], and aspect ratio [R]) generated from 14 samples representing three facies of the Miss Lime. The novelty of this article lies in the fact that it begins to decipher the dependencies of ultrasonic velocities by providing a tentative hierarchy of the parameters that may influence dry-rock V_P in the Miss Lime and shows that pore-size distribution may have greater importance in these low-porosity reservoirs.

2.3 Study Area

During the Mississippian Epoch (358.9 ± 0.4 to 323.2 ± 0.4 Ma), present-day Oklahoma and Kansas were situated close to the equator in the southern hemisphere (Lane and De Keyser 1980, Mazzullo et al. 2011). The regressing coastline in the Anadarko Basin led to the development of an extensive east–west-trending carbonate shelf on top of the Devonian-age Woodford Shale near the present-day Oklahoma–Kansas border. The shelf development ended with a period of uplift and erosion in the late Mississippian accompanying the collision between Gondwana and

Euramerica. Two kinds of sediments, limestones and silicified limestone (with abundant chert), dominated the Mississippian-age shelf, with their depositions jointly controlled by higher-order eustatic sea-level changes and tectonism (Childress and Grammer 2015). These sediments eventually formed the ‘‘Miss Lime’’ reservoirs, sourced by the Devonian-age Woodford shale and sealed by the overlying Pennsylvanian-age transgressive shaley units.

2.4 Rock Properties Dataset

A summary of the data set generation is presented below, and the reader is guided to Vanden Berg and Grammer (2016) for details. Samples in this study were drawn from three cores, identified as C1, C2, and C3 (Figure 2.1), located in Payne and Logan counties in North– Central Oklahoma. Approximately 2-inch- (5-cm)-long plugs were extracted at multiple locations along cores C1 to C3 based on facies interpretation (Vanden Berg and Grammer 2016). A portion of individual core plugs was sawed and separated for measuring composition and microscopy, and the remainder were used for porosity and sonic arrival times. Restricted access to testing of core material allowed generation of a complete data set (elastic velocities, composition, ϕ, and pore architecture) only at 14 locations. Composition was measured using X-Ray Diffraction (XRD); bulk ϕ was measured using gas injection under reservoir pressure (15 MPa); pore P, A, and R were determined from Digital Image Analysis (DIA) of Light Microscopy (LM) and Scanning Electron Microscopy (SEM) images; and the P-wave transit times were measured on 1.5-inch-(~3.8-cm)-diameter core plugs using the standard pulse-echo method. Measured data are presented in Table 2.1. The motivations for DIA for understanding pore architecture come from peer studies such as those of Anselmetti et al. (1998) and Weger et al. (2009). In Table 2.1, bulk porosity data were generated at Devon Coproration, Oklahoma City, USA, facies and pore architecture data were generated at Oklahoma State University, Stillwater, USA, and sonic measurements were done at University of Miami, Miami, USA.

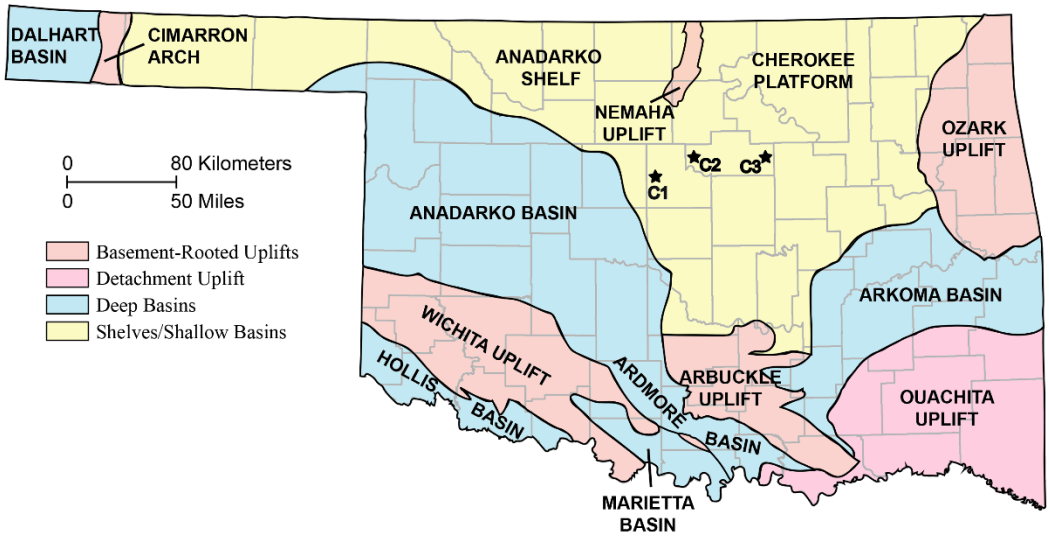

Figure 2.1 Base map. Major geological features are labeled on the map of Oklahoma. Core locations are indicated with the star symbol and labeled. Core C1 is from Logan County. Cores C2 and C3 are from Payne County (after Northcutt and Campbell 1995).

2.4.1 Composition

Samples were powdered using a SPEX ball mill and then analyzed in a Philips PW3020 Diffractometer operated at 45 kV and 40 mA. Prior to the analysis, the machine was calibrated with a quartz sample. Elements were identified by matching the XRD response with a standard Powder Diffraction File in Xpert High Score software.

2.4.2 Pore Architecture

Pore P, A, and R were generated from DIA of LM and SEM photomicrographs that were acquired at magnifications ranging from 5× to 150,000× (Figure 2.2). For LM imaging sample billets were epoxy impregnated, mounted on 1 by 3-inch slides, and polished to 20- to 30-µm thickness. The photomicrographs were captured using a Leica DM 2700P optical microscope. For SEM imaging sample billets were polished using JEOL IB-19500 CP argon–ion mill (to avoid the milling artifacts), kept under vacuum for 2 hours, and sputter-coated with gold/palladium for 20 seconds using Balzers MED 010. The photomicrographs were then captured using a FEI Quanta

600F field emission SEM. Both LM and SEM samples were optimally oriented such that the cross-sectional views were perpendicular to the lamination.

Table 2.1: Sample composition and properties

Core Facies	Depth (ft)	ϕ (%)	V_P (m/s)	Silicate (%)			Carbonate (%)			Clay (%)			Others (%)	
				Quartz	Orthoclase	Plagioclase	Calcite	Dolomite	Siderite	Kaolinite	Illite	Mix Illite/ Smectite	Pyrite	Apatite
C1-A	5581.70	1.83	5157	46	2	3	43	3	0	0	1	1	1	0
C1-A	5701.65	1.18	5269	39	1	3	51	3	0	0	1	1	1	0
C1-B	5599.40	2.75	5121	54	3	6	19	1	0	0	8	3	3	3
C1-B	5705.30	2.91	5210	38	1	6	34	13	0	0	4	1	2	1
C1-B	5624.20	4.93	5493	36	1	2	59	1	0	0	1	0	0	0
C2-C	5258.50	5.56	5578	22	1	3	61	10	0	0	2	1	0	0
C2-C	5234.60	0.93	5668	22	1	3	73	0	0	0	1	0	0	0
C1-C	5526.05	2.03	5770	22	1	4	71	1	0	0	1	0	0	0
C2-C	5126.80	4.72	5419	39	1	1	53	0	1	1	2	0	0	2
C2-C	5129.75	6.64	5451	43	1	2	52	0	0	1	1	0	0	0
C3-C	4446.55	3.35	5737	40	0	1	54	4	0	0	0	1	0	0
C1-C	5728.80	1.56	4740	71	1	0	21	7	0	0	0	0	0	0
C2-C	5124.10	9.67	5086	85	2	2	0	0	1	1	6	0	1	2
C1-C	5628.50	1.93	5885	80	2	1	16	1	0	0	0	0	0	0

Leica's propriety software LAS Application Suite was used for analysis of the photomicrographs (Figure 2.2). Image processing was used to recognize two types of pores: (1) blue-epoxy-impregnated and (2) oil-filled pores. Photomicrographs were binarized using the in-built structuring elements of the software for separating pores and grains followed by application of a smoothing filter to sharpen the pore–grain contacts as needed. Image segmentation for pore selection was achieved by setting thresholds in color scale (hue, saturation, and intensity) and grayscale (white to black) for LM (color) and SEM (grayscale) photomicrographs, respectively. Analysis of every image was carefully monitored, and, as a clarification, none of the image

processing steps were conducted in a batch mode. Pores were manually outlined when wedge effects were strong.

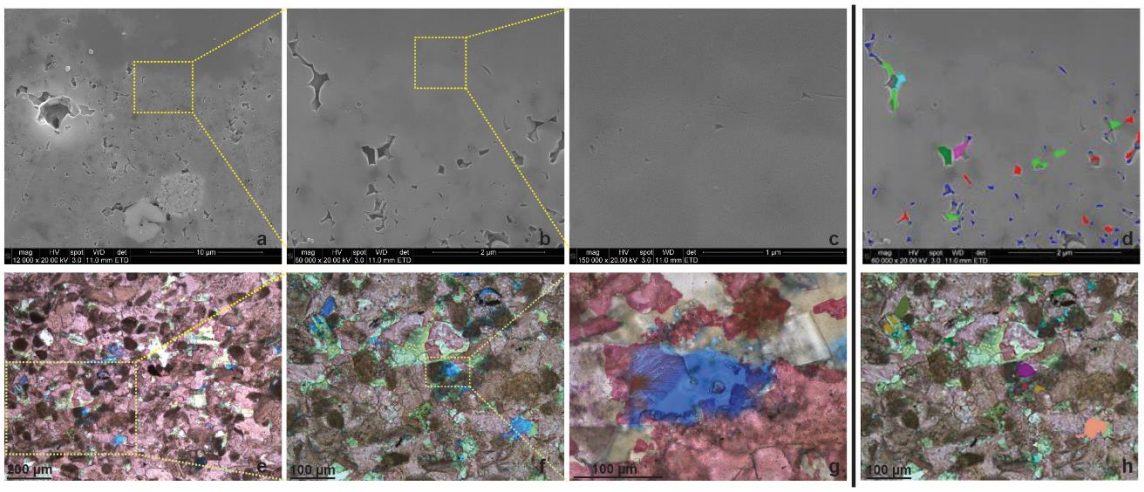

Figure 2.2 Digital Image Analysis (DIA). Images in **(A)** through **(C)** and **(E)** through **(G)** are, respectively, representative of scanning electron microscope (SEM) and light microscope (LM) photomicrographs at progressively higher magnifications. Images in **(D)** and **(H)** showing colored pores are from image processing of the SEM and LM photomicrographs by the Leica algorithm.

To ensure proper merging of results across different magnifications both the measurement frame (image area to be analyzed) and the scale bar were provided as inputs. Heuristically, 0.5 µm and 1.5 nm were set as the smallest pore sizes that could be reliably identified in LM and SEM photomicrographs, respectively. For P, all pixels along the periphery of a feature identified as pore were counted, accounting for projections and compensating for edge orientation. For A, all pixels lying within the periphery were counted. The length was defined as the largest distance between two points on the periphery along a straight line through the pore, and width was defined as the shortest. The R value was computed as the ratio of the length to the width, regardless of their spatial orientation.

Pore architecture data were generated using both LM and SEM images, but as a result of the higher abundance of pores that were beyond the resolution of the LM images, the contribution of SEM images in the overall pore population was significantly higher (as much as 95%).

Regardless, by capturing a multitude of images at varying magnification, an effort was made to ensure that the pore populations used in this study are reflective of at least 80% of sample porosity.

2.4.3 Facies Interpretation

The Miss Lime stratigraphic units in all three cores, C1 through C3, were interpreted as the section between two key transitions—the underlying Devonian and the overlying Pennsylvanian shales (LeBlanc 2014, Vanden Berg and Grammer 2016). A summary is provided below. Transitions were visually identified as a change in rock texture and type. In total, 202 m (657 ft) of the Miss Lime core was included in the analysis: 100 m (324 ft) in C1, 58 m (187 ft) in C2, and 44 m (143 ft) in C3. Facies were defined by trace fossils, composition, texture, color, and sedimentary structures, following the Dunham (1962) scheme that relates facies to depositional environments. Bioturbation intensity was interpreted following Miller and Smail (1997) guidelines, trace fossils were identified following MacEachern et al. (2009) indexing, and colors were interpreted using the Geological Society of America chart (GSA 1995). Overall, facies in cores C1 through C3 (located ~50 miles apart) were interpreted as transitioning from an inner ramp setting below storm wave base to a proximal location above fair-weather wave base in a high-energy shoal environment.

The three main facies, A, B, and C, represented by samples in this study were present in all three cores. Facies A was dusky yellowish brown in color, with crinoids, brachiopod fragments, and sponge spicules. It was identified as a bioturbated wackestone to packstone deposited in a middle ramp setting with burrows and local thin bedding (Figure 2.3A), with interparticle primary and matrix and intraparticle secondary ϕ. Facies B was olive-gray in color, with peloids, crinoids, sponge spicules, and brachiopod fragments. It was identified as a peloidal packstone to grainstone with massive bedding and bioturbation deposited in a midproximal ramp setting (Figure 2.3B), with the same primary and secondary ϕ as Facies A. Facies C was medium to dark gray and dark yellowish-brown in color, with peloids, crinoids, sponge spicules, brachiopods, and bryozoan fragments. It was identified as a skeletal packstone to grainstone with cross-bedded skeletal debris

deposited mostly on a high-energy shoal in the proximal ramp and above fair-weather wave base (Figure 2.3C), with the same primary and secondary ϕ as Facies A and B. In terms of overall grain size, facies transitions from clay/mud (<4 µm) in the middle ramp to silt (<63 µm) in more proximal positions. In general, Core C1 was dominated by peloidal packstone–grainstone facies, while Core C3 was dominated by skeletal packstone–grainstone facies, which suggested a shallowing-upwards environment from C1 to C3 (LeBlanc 2014, Vanden Berg and Grammer 2016).

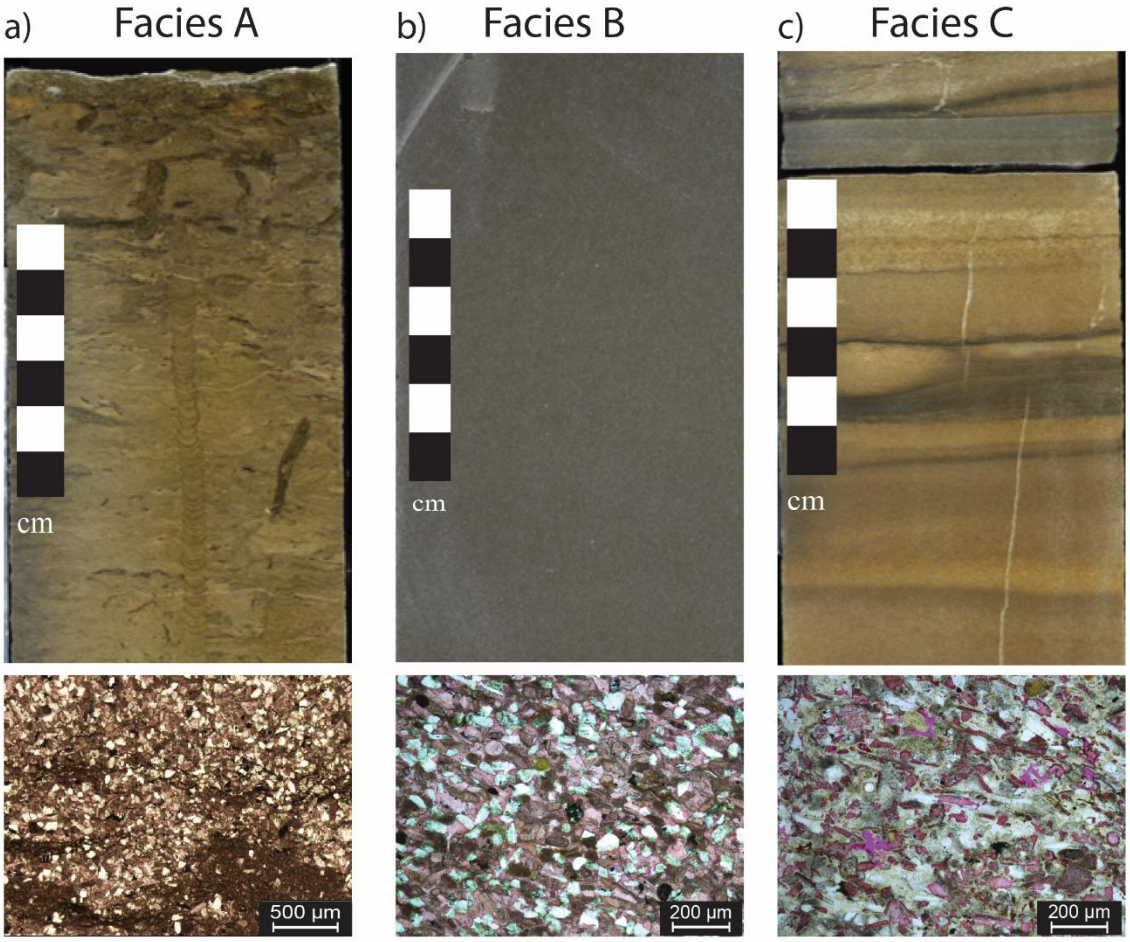

Figure 2.3 Facies Interpretation. Core scale and LM images of **(A)** Facies A, which is a bioturbated wackestone-packstone; **(B)** Facies B, which is a peloidal packstone-grainstone; and **(C)** Facies C, which is a skeletal packstone-grainstone. Change of facies from **(A)** through **(C)** represents a change from proximal shelf to middle-inner ramp depositional environment (LeBlanc 2014).

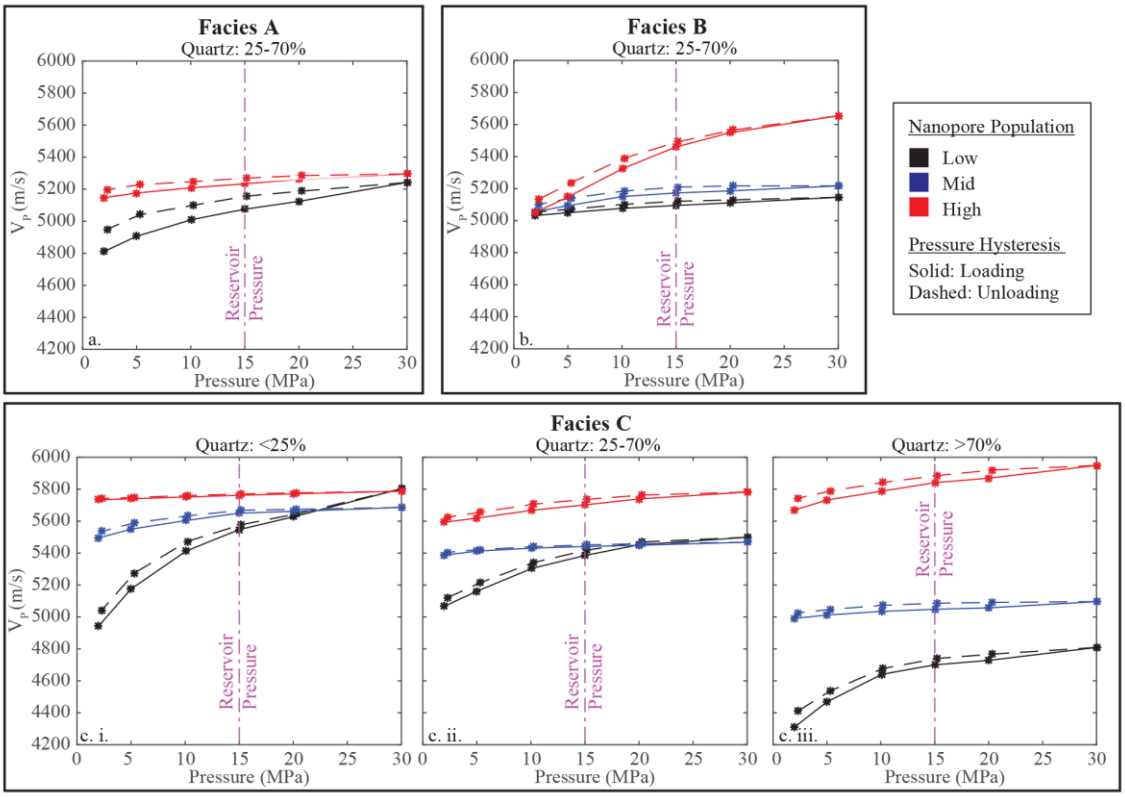

Figure 2.4 Dry P-wave velocity (V_P) versus pressure. Hysteresis loops for samples are classified according to facies composition subgroup. In **(A)** through **(C)**, the average reservoir pressure, 15 MPa, is indicated; solid and dashed lines represent, respectively, the loading and unloading part of the loop; and red, blue, and black color codes indicate samples classified as having higher, mid, and lower nanopore population, respectively, in Figure 2.7.

2.4.4 Sonic Velocities

One P-wave and two mutually perpendicular S-wave transit times were recorded on each sample plug with a New England Research Autolab 1000 machine. This article uses P-wave transit times only. Individual plugs were enclosed in a rubber jacket, secured between a transducer and receiver, and placed in a pressure chamber that was filled with mineral oil. Arrival times were recorded in both dry and brine-saturated conditions at incrementally increasing and decreasing pressures from 2 MPa to 30 MPa over a full hysteresis loop, simulating burial depth conditions of 640 to 9600 ft (195–2920 m), assuming a 3.102-kPa/ft (10.18-kPa/m) hydrostatic gradient. In this article only the dry-rock values are used to avoid the influence of partial saturation (Figure 2.4).

Samples in this study range between 4446.55 ft (1355 m) and 5728.80 ft (1746 m) in depth (Table 2.1), which corresponds to an effective pressure range of 13.82 to 17.81 MPa. In the entire hysteresis data set, only one measurement (15 MPa; Figure 2.4) falls within this range, making the corresponding V_P most relevant for rock property analysis. Further, only the unloading part of the hysteresis loop is used to avoid the effect of open stress-cracks. Hereafter, the term V_P automatically assumes dry-rock and unloading.

2.5. Results

In total, data from 14 samples were analyzed in this article, with the goal of understanding the causation of their V_P. First, to understand the effect of composition and ϕ on V_P of a grain pack, which is how the Wyllie et al. (1956) model views the rock, consider a system comprising 25% quartz, 25% calcite, 25% dolomite, 25% clay, and 10% air-filled porosity. The mechanistic behavior of such a grain pack is elegantly described by the Raymer et al. (1980) model (see Appendix A). Accordingly, Figure 2.5A shows the effect of changing different compositional constituents and ϕ of this grain pack on its V_P. As expected, in Figure 2.5A, compositionally induced V_P changes are proportional to the moduli of the minerals (Table 2.2), and, for the same composition, V_P varies inversely with ϕ (Figure 2.5A). Next, assuming that samples in this study are Wyllie-type grain packs, an expected V_P can be computed for each of them using the Raymer model based on their known composition and ϕ. As a clarification, the intent here is not to imply that the Raymer model is the actual mechanistic model of the Miss Lime reservoirs but to rather examine how the samples in this study deviate from a Wyllie-type system. Figure 2.5B compares the expected V_P (solid red dots) and the measured V_P (solid blue stars).

In Figure 2.5B, the misfit between the observed and the expected V_P is fairly variable, ranging from <1% to >20%, and is generally higher at lower ϕ. Two lines of reasoning can be envisioned to explain this. First, different samples are being governed by different mechanistic models. For example, some samples have contact cements or microgeometries that create grain

boundary traction that is not accounted for by the Raymer model. Second, there are other drivers of V_P besides composition and ϕ. While the possibility of 14 different mechanistic models cannot be ruled out, samples within the same facies are more likely to have a common mechanistic model, which is driven by its grain arrangement. To account for the potential difference in mechanistic models, the samples are analyzed ‘‘facies wise.’’ This, however, limits the number of samples per facies (two, three, and nine samples in Facies A, B, and C, respectively). Furthermore, Figure 2.5A implies that it is possible to have multiple combinations of composition and ϕ that can yield similar V_P values. Therefore, to understand ϕ-only–induced V_P changes, samples with similar composition are grouped together. Therefore, in addition to facies-wise grouping, categorizing samples into three groups of quartz: <25%, 25 to 70%, and >70%, creates facies-composition subgroups with the most comparable mineralogy (Table 2.1).

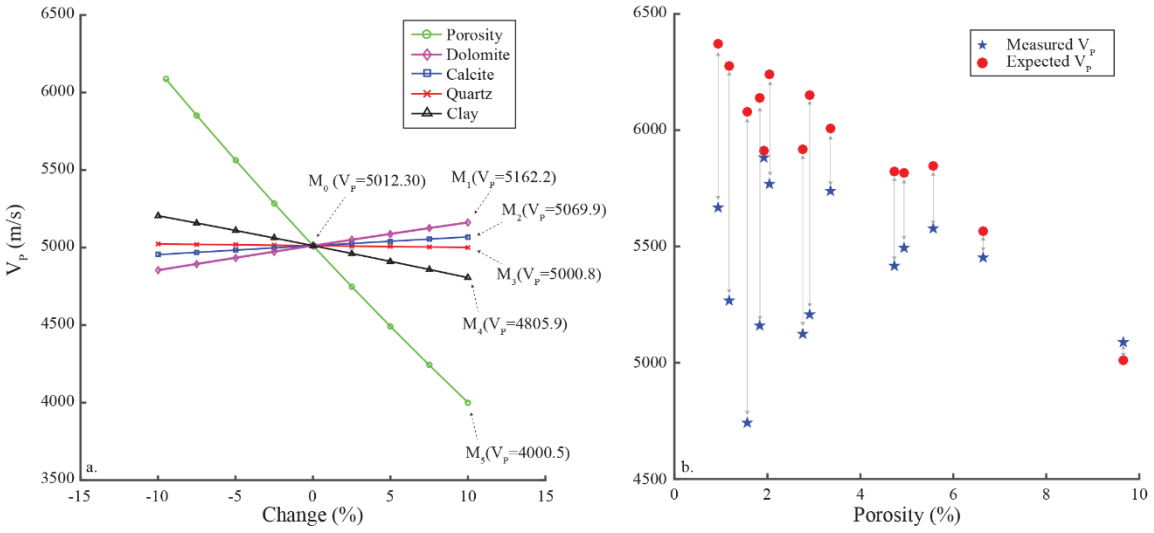

Figure 2.5 Raymer et al. (1980) model. **(A)** Figure shows dependence of V_P of a grain pack on composition and bulk porosity (ϕ). In the reference model, M_0, calcite (C) = dolomite (D) = quartz (Q) = clay (Cl) = 25% and ϕ = 10%. The V_P trajectory due to a change in ϕ (composition same as M_0) is marked with a green circle. The V_P trajectory due to a change in D, C, Q and Cl (ϕ same as M_0) are marked correspondingly with a purple diamond, blue square, red cross, and black triangle. When the proportion of any one mineral is changed, the proportions of the other three minerals are equally compensated. For example, in M_1, D = 35% and C = Q = Cl = 21.67%; accordingly, in M_2, C = 35% and D = Q = Cl = 21.67%; in M_3, Q = 35% and D = C = Cl = 21.67%; and in M_4, Cl = 35% and D = C = Q = 21.67%. In M_1 through M4, ϕ = 10%. In M_5, C = D = Q = Cl = 25% and ϕ = 20%. **(B)** Solid blue star indicates measured V_P, and solid red dots indicated the corresponding

V_P predicted using the Raymer model. Light-gray arrows are used to identify observed and predicted V_P pairs for the same sample. Figure shows that the deviation between the observed and predicted V_P is generally higher at lower ϕ.

Table 2.2: Rock Properties

Constituents	Bulk Modulus (K) (in GPa)	Shear Modulus (μ) (in GPa)	Density (ρ) (in g/cc)
Quartz	38	44	2.65
Calcite	77	32	2.71
Dolomite	95	45	2.87
Clay	21	7	2.54
Air	0.000131	0	0.00119

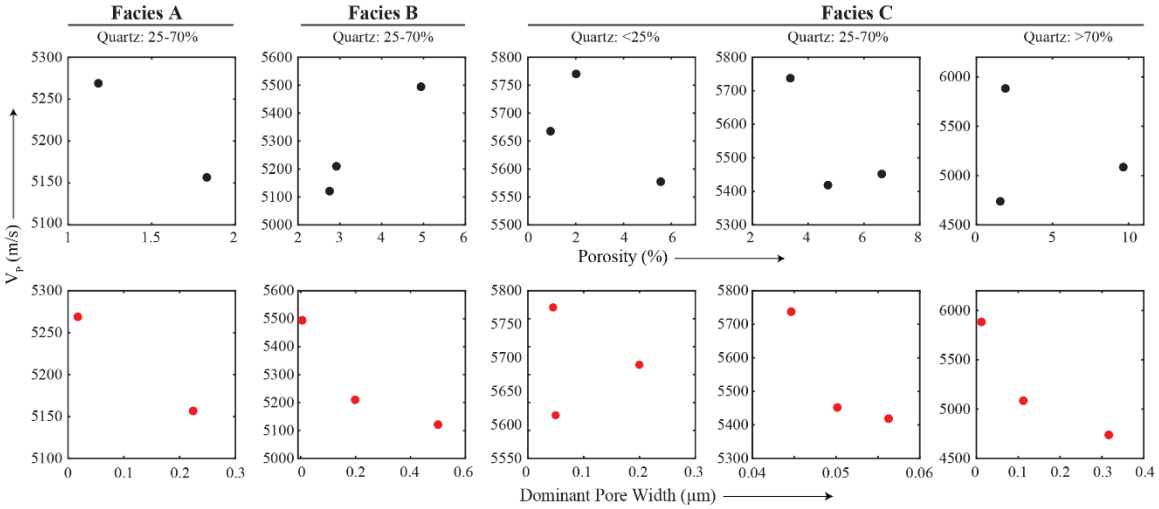

Figure 2.6 Crossplot of dry V_P versus **(A)** bulk ϕ and **(B)** dominant pore width (S_ϕ). Samples are categorized into facies-composition subgroups, with the exception that in **(A)** V_P will change inversely with ϕ. The figure shows that the inverse relationship, however, is more apparent with **(B)**, the dominant pore width (S_ϕ), suggesting that in this data set, pore size exerts a strong influence on V_P, in addition to ϕ.

Plots of V_P versus ϕ for all the facies-composition subgroups are shown in Figure 2.6A.I to Figure 2.6A.V, where, unlike what was expected, V_P does not seem to be varying inversely with ϕ. Again, a multitude of grain arrangement–based reasons can be postulated to explain Figure 2.6A, but interestingly, when the V_P is plotted against the dominant pore width, S_ϕ, (Figure 2.6B), obtained from DIA, V_P exhibits the kind of trend it was expected to exhibit for ϕ, with an exception of Facies C, the <25% quartz subgroup. Pore width rather than pore length is chosen in Figure 2.6B

because it provides a sense of the minimum pore opening, which is relevant to the seismic strain. In any case, Figure 2.6 suggests that in this data set, pore size might also be exerting control on V_P in addition to, or instead of, ϕ.

To better appreciate the pore-size distribution in the samples, simultaneous visualization of the distribution of pore A and pore P through contoured two-dimensional (2D) histograms is shown in Figure 2.7. In Figure 2.7, the warmer colors represent higher count, and the pore population most closely associated with S_ϕ in Figure 2.6B is indicated with a solid black star in the corresponding samples. Figure 2.7 drives the point home that within each facies-compositional subgroup, as the dominant S_ϕ decreases (i.e., as the peak population [warmer colors] shifts toward smaller P–A values), V_P increases. The reader may note that the peak pore-population distributions in Figure 2.7C.I and 2.7C.II overlap, and, therefore, the behavior of Facies C (<25% quartz subgroup in Figure 2.6B) may be within the arena of data uncertainty.

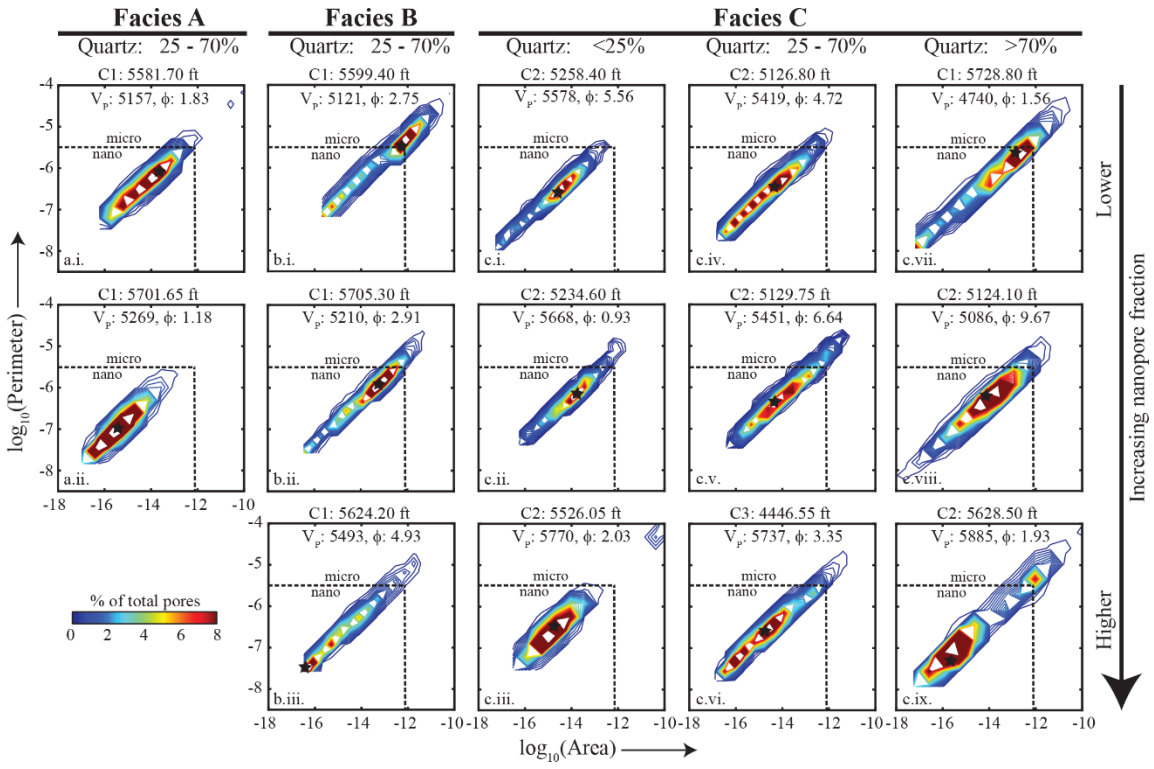

Figure 2.7 Dry V_P versus pore size. Pore perimeter (P), area (A) data generated using DIA are binned and presented as contour plots in a log-log scale for **(A)** Facies A, **(B)** Facies B, and **(C)**

Facies C. Facies-composition subgrouping is the same as in Figure 2.6. Sample depth, measured dry V_P, and ϕ are mentioned, and the range for micro-(>1-µm) and nano-(<1-nm) pores (Loucks et al. 2012) are indicated. In **(A)** through **(C)**, warm contour colors indicate higher pore proportion, and the pores get smaller toward the lower left. Arrow indicates increasing nanopore proportion. Figure indicates that within facies-composition subgroups, V_P increases as the dominant pore size decreases.

Figure 2.7 only shows the effect of changing pore size on V_P. To examine the effect of changing pore shape (elongation, complexity, etc.), R–P/A pairs of pore population within individual samples are binned in the same fashion as in Figure 2.7, and their contoured 2D histograms are examined within the same facies-composition subgroup in Figure 2.8. In Figure 2.8, the abscissa ranges from 6 (equivalent to P/A ~1 μm^{-1}) to 9.5 (equivalent to P/A ~3200 μm^{-1}), and the ordinate ranges from 0 (equivalent to R = 1, representing a circle) to 1.2 (equivalent to R ~ 16, representing an ellipse with major axis 16 times longer than the minor axis). Figure 2.8 shows that increasing V_P is accompanied by a shift in the pore population, mainly along the abscissa rather than the ordinate. A shift along the abscissa in Figure 2.8 implies a general decrease in pore size, much like what is conveyed by Figure 2.7. In Figure 2.8, the number of complex pores (pores inferred to be nonelliptical from P/A values [e.g., arbitrary pore shape such as ‘‘C’’]) is also mentioned for individual samples. Figure 2.8 reemphasizes that in this data set, pore size exerts a strong influence on V_P.

2.6 Discussion

This article presents various types of data measured using different instruments. Consequently, their uncertainties are bound to be variable, reflective of both instrument and sample quality. For example, ϕ uncertainties depend on the magnitude of the ϕ itself (the lower the ϕ, the higher the uncertainty), grain-surface chemistry, pore geometry, and measurement method. Similarly, ultrasonic wave arrival-time uncertainties also depend on sample finishing (flatter, smoother end surfaces ensure better instrument coupling), sample dimension (a ratio of 1:2 for diameter and length is ideal for laboratory measurements), and damage (cracks, etc.). Composition

uncertainties depend on the element's concentration and its natural diffraction strength, and defining pore geometry can be interpretive.

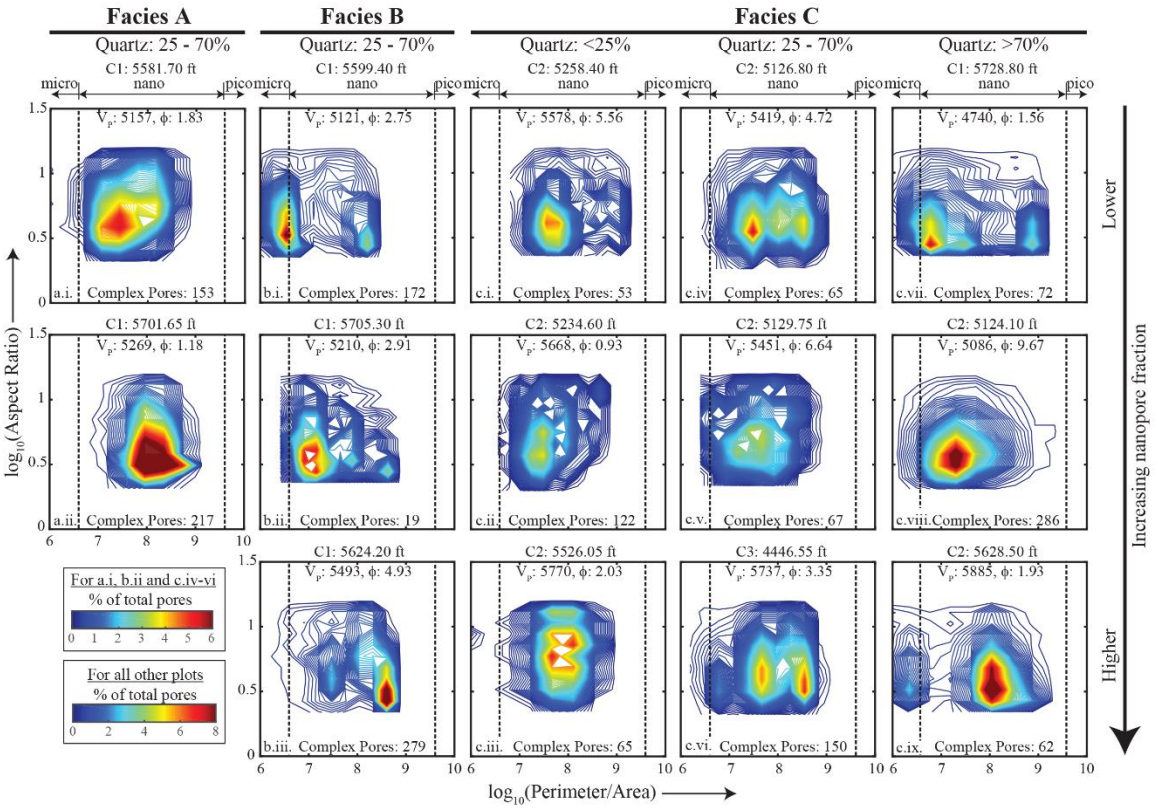

Figure 2.8 Dry V_P versus pore aspect ratio (R). R versus P/A pairs are binned and presented as contour plots in a log–log scale for samples drawn from **(A)** Facies A, **(B)** Facies B, and **(C)** Facies C. Facies-composition subgrouping, colors, and symbols are the same as in Figure 2.7. Sample depth, measured dry V_P, ϕ, and the number of complex pores are listed. Figure shows that within the same facies-composition subgroups as Figure 2.7, VP increases with increasing P/A (decrease in pore size) rather than with changes in R. The reader may note that as the area of the ellipse decreases, its P/A will increase if R is held constant.

The gas injection method used for ϕ measurement in this article is typically accurate to within ±0.5% porosity units (Espinal 2002), and even then it is most effective when ϕ is connected. In these samples, as previously noted, the ϕ is also intraparticle in nature, not all of which might be connected. The accuracy of the correlation method used for calculating the ultrasonic arrival times in this article varies between ±0.3% and ±1.5% and mainly depends on background conditions

(Molyneux and Schmitt 1999). The reader may note that in the hysteresis data (Figure 2.4), V_P only differs by 20 m/s between the loading and unloading cycles. Further, the unloading cycle is consistently higher than the loading cycle and follows it closely, which suggests that the overall sonic measurement errors in this data set should be within 20 m/s or else the trends may have intersected. The accuracy of the diffraction patterns for mineralogical composition depends on the nature of the element being detected. For quartz, which has high diffraction intensity, the measurement accuracy is high, possibly within ±3% (Norrish and Taylor 1962). Finally, uncertainty associated with individual pore dimensions is difficult to estimate, and, therefore, in this article the geometrical properties of a large number of pores within an individual sample are statistically examined.

Uncertainties related to representativeness are inherent to data sets like the one described in this article, for which rock property is generated using limited samples. Questions relative to how representative the individual SEM or LM images for each sample are in terms of volume coverage and heterogeneity are difficult to address. Additionally, because this is a 2D data set, it is understood that some finer details of the pore shapes that could only be captured in three dimensions (3D) would have remained unaccounted for. Short of 3D pore imaging (Desbois et al. 2009), some of these issues cannot be quantitatively addressed with this small data set, and even then, uncertainties in representativeness cannot be completely avoided. However, despite the inherent limitations, the authors are confident that from the large number of images analyzed in the study over a varied range of magnifications (Vanden Berg and Grammer 2016), the pore-size distribution of all samples have been effectively captured.

It is notable that V_P of the samples in Figure 2.7C.I and 2.7C.II, 5578 m/s and 5668 m/s, respectively, are close, and so are their pore distributions. The measured porosities of the same samples, on the other hand, 5.56% and 0.93%, respectively, are significantly different from each other. A somewhat similar scenario exists for Figure 2.7C.IV and 2.7C.V. These examples support

that V_P is likely related to pore distribution more than the bulk ϕ. The reader may also note that the composition from one subgroup to another (e.g., Figure 2.7C.I–III. versus 2.7C.IV–VI versus 2.7C.VII–IX) is sufficiently different, but V_P variations are comparable (the difference between minimum V_P of the first two subgroups is within ~150 m/s and maximum V_P of all three subgroups is within 100 m/s). However, and as a clarification, the article does not intend to undermine the effect of ϕ or the composition on V_P but instead argues that the effect of rock texture could be equally significant, especially in low-porosity regimes. Furthermore, the hierarchy of sample classification in Figure 2.7 suggests that for understanding the elastic properties of ‘‘Miss Lime,’’ a facies-wise approach, as opposed to the whole-rock approach, might be advantageous.

In Figures 2.7 and 2.8 samples are classified into high-, mid-, and low nanopore groups. This classification is relative but helps in appreciating the hysteresis data in Figure 2.4, in which the V_P of all samples generally increased with pressure but in which the rate of increase is different. In Figure 2.4, samples with a relatively higher fraction of nanopores tended to have higher V_P across the entire pressure range, with three exceptions: Facies B at 2 MPa (Figure 2.4B) and Facies C at 30 MPa (Figure 2.4C.I and 2.4C.II). In Facies C, the difference in V_P over the pressure range for samples identified as having mid (Figure 2.7C.II, C.V, and C.VIII) and low (Figure 2.7C.I, C.IV, and C.VII) nanopores is more complicated. In at least two instances, for the low-quartz and the mid-quartz compositional subgroups in Figure 2.7C, the low nanopore V_P rapidly approaches the mid nanopore V_P and exceeds it at a pressure greater than reservoir pressure (Figure 2.4C.I and C.II, respectively). Nonetheless, Figures 2.4 through 2.8 generally show that higher nanopore proportions are consistent with higher V_P. On a related note, it is possible that depending on the composition and diagenetic history of a carbonate rock, DIA results at atmospheric pressure may or may not represent in situ conditions, and in general it is difficult to speculate how pressure will change pore architecture (e.g., whether pore deformation is a linear [e.g., Castagna et al. 1985], nonlinear [e.g., Jones and Nur 1984], or a step function of pressure).

As is the case in this article, Weger et al. (2009) also used DIA to measure pore architecture, such as pore shape and size distribution. However, they concluded that for comparable bulk ϕ, V_P was higher when the dominant pore sizes were larger and pore geometries were simpler. While their findings seem to be contradicting those of this article, key differences between the two data sets need to be appreciated. The Weger et al. (2009) samples span across multiple facies in multiple basins, as opposed to the samples in this study, which focuses on a single low-permeability mixed siliciclastic–carbonate unconventional system. Further, the Weger et al. (2009) samples seem to dominantly have macro- to mesopores, while samples in this study are dominantly nanopores.

Why samples with dominant macropores (e.g., Weger et al. 2009) should differ in their elastic behavior from samples with dominant nanopores (e.g., Vanden Berg and Grammer 2016, Vanden Berg et al. 2018) is difficult to understand. One possible mechanism that might distinguish macropore and nanopore systems is pore closure due to seismic strain (<1μm at MHz frequency range [Tutuncu et al. 1998]), which will dynamically increase the grain-to-grain contact stiffness and, in turn, increase the dynamic moduli of the system. The term ‘‘dynamic’’ explicitly implies a transitionary state that is only associated with the harmonic pressure changes during the wave propagation. This can also explain Figures 2.6B.III, 2.7, and 2.8, in which the V_P increase within every facies-composition subgroup appears to be consistent with a decrease in the dominant pore size. Assuming that pores and pore throats are proportionately abundant, a higher nanopore population in a sample will present more opportunity for the propagating seismic waveforms to induce changes in the medium.

If the pore throat–closure mechanism indeed happens to be one of the V_P drivers in these samples, it is worth exploring how to incorporate this physical phenomenon in seismic modeling. Directly incorporating the speculated pore throat closure in wave-equation modeling is difficult given that accounting for pore heterogeneity, even with state-of-the-art algorithms, is still a challenge. Pores are nominally accounted for through the Kuster and Toksöz (1974) KT model,

which views the rock as a mixture of matrix and inclusions (circular or elliptical pores). For the KT model to work well, the inclusions need to be disconnected and dilute in distribution. The Differential Effective Medium (DEM) model (Norris 1985, Christensen 1990) can overcome the dilute distribution to some extent but cannot adequately account for the partial saturation, complex connectivity, and capillary effects that are characteristics of low permeability formations. Nonetheless, both KT and DEM models have been able to explain a large number of field and laboratory data sets within reasonable error tolerances (Rossebø et al. 2005, Baechle et al. 2007, Smith et al. 2009, Xu and Payne 2009, Misaghi et al. 2010). However, both KT and DEM models assume a static pore distribution (i.e., pore shapes and sizes do not change as a result of harmonic pressure changes).

It might be possible to account for dynamic pore-size changes indirectly. One approach could be to define an empirical relationship between the pore-size distribution (probability function of pore area and perimeter) and V_P along the lines of Kittridge (2014) and Zhang and Li (2017). The other approach could be to use an apparent ϕ instead of bulk ϕ, proportionate to the dominant pore size in mechanistic models such as that of Nur et al. (1998). A more comprehensive approach could be achieved through use of the Sun (1994) and Sun and Goldberg (1997) wave equation formulation, which is an extension of the Biot (1956) model to make imperfections (voids, fractures, etc.) a part of the effective medium rather than a boundary value problem. Two free parameters introduced by Sun (1994) and Sun and Goldberg (1997), representing solid–solid and fluid–solid coupling (referred as the frame flexibility coefficients), could be of significance to this article. The fluid–solid coefficient accounts for wettability, and the solid–solid coefficient appears to be representing the contact stiffness. Thus, V_P in Figures 2.7 and 2.8 could, in principle, be modeled by making the solid–solid coefficient inversely proportional to the dominant pore size. The frame flexibility coefficients have been previously used by Zhang et al. (2012) and Wang et

al. (2014) for relating pore architecture to elastic velocities in carbonate rocks, but without invoking the concept of dynamic contact stiffness.

To exhaustively test how pore-size distribution affects elastic velocities, more advanced microscopy and imaging, as compared to what is being presented in this article, are needed. For example, first, how representative pore geometries gathered from 2D SEM photomicrographs are of the actual 3D distribution needs to be examined. The authors do not believe that 2D SEM imaging followed by image analysis can be completely replaced by direct 3D pore network imaging because of practicality when large numbers of samples are involved. Instead, it might be more practical to infer pore-size distribution in three dimensions by nuclear magnetic resonance and to understand the pore geometry through 2D SEM images. Another key aspect that needs to be explored is how pore distribution changes under external stress. Whether intraparticle pores close before interparticle pores and whether pores associated with quartz grains respond differently to stress than do pores associated with organic matter, calcite, or dolomite grains are relevant problems that should be pursued in future studies.

2.7 Conclusion

This article relates rock properties (composition, ϕ, and pore A, P, and R from DIA of LM and SEM photomicrographs) to ultrasonic V_P in 14 samples representing three facies of the Miss Lime. At the outset, the relationship between bulk ϕ or composition and dry-rock V_P is not easily explained, but when the samples are categorized according to the quartz content (<25%, 25–75%, and >75%) within individual facies, there seems to be a relationship between V_P and pore distribution. Within the individual facies-composition subgroups, V_P increases as the dominant pore size progressively decreases below 1μm. Results from this study highlight the need for accounting for pore distribution in elastic modeling. At the very least, the hierarchy of sample classification suggests that a facies-wise rather than a whole rock approach might be better for understanding the Miss Lime elastic properties.

2.8 References

Ahr WM. 2011. Geology of Carbonate Reservoirs: The Identification, Description and Characterization of Hydrocarbon Reservoirs in Carbonate Rocks: John Wiley & Sons, Hoboken, New Jersey. 296 p.

Anselmetti FS, Luthi S, Eberli GP. 1998. Quantitative characterization of carbonate pore systems by digital image analysis. American Association of Petroleum Geologists Bulletin 82:1815–1836.

Avseth P, Dvorkin J, Mavko G, Rykkje J. 2000. Rock physics diagnostic of North Sea sands: Link between microstructure and seismic properties. Geophysical Research Letters 27:2761–2764.

Baechle GT, Colpaert A, Eberli GP, Weger RJ. 2007. Modeling velocity in carbonates using a dual-porosity DEM model, SEG Technical Program Expanded Abstracts 2007: Society of Exploration Geophysicists, Tulsa, Oklahoma. p. 1589–1593.

Baechle GT, Weger R, Eberli GP, Colpaert A. 2006. Pore size and pore type effects on velocity—Implication for carbonate rock physic models, Workshop ‘‘Sound of Geology.’’ http:://mgg.rsmas.miami.edu/students/greg/cipr_baechle-final.pdf. Accessed December 10, 2017.

Biot MA. 1956. Theory of propagation of elastic waves in a fluid-saturated porous solid. I. Low-frequency range. The Journal of the Acoustical Society of America 28:168–178.

Castagna JP, Batzle ML, Eastwood RL. 1985. Relationships between compressional-wave and shear-wave velocities in clastic silicate rocks. Geophysics 50:571–581.

Childress M, Grammer GM. 2015. High resolution sequence stratigraphic architecture of a Mid-Continent Mississippian outcrop in southwest Missouri. Shale Shaker 66:206–234.

Childress M, Grammer GM. 2017. Characteristics of debris flows and outrunner blocks—Evidence for Mississippian deposition on a distally steepened ramp. In Grammer GM, Gregg JM,

Puckette JO, Jaiswal P, Mazzullo SJ, Pranter MJ, Goldstein RH (Editors). Mississippian Reservoirs of the Midcontinent, Memoir 116: American Association of Petroleum Geologists, Tulsa, Oklahoma. DOI:10.1306/13632145M1163786

Christensen RM. 1990. A critical evaluation for a class of micro-mechanics models. Journal of the Mechanics and Physics of Solids 38:379–404. Desbois G, Urai J, Kukla P. 2009. Morphology of the pore space in claystones—Evidence from BIB/FIB ion beam sectioning and cryo-SEM observations. eEarth Discussions 4:15–22.

Dick J. 2012. The Unconventional Mississippian Play Early Producing and Completion Statistics (& Observations), Mississippian and Arbuckle Workshop: Oklahoma Geological Survey, Norman, Oklahoma. http://ogs.ou.edu/docs/meetings/OGS-workshop-mississippian_arbuckle_2012-dick.pdf. Accessed December 10, 2017.

Doyen P. 2007. Seismic Reservoir Characterization: An Earth Modelling Perspective, Vol. 2: EAGE (European Association of Geoscientists and Engineers) Publications, Houten, The Netherlands. 255 p.

Dunham RJ. 1962. Classification of carbonate rocks according to depositional textures. In Ham WE (Editor). Classification of Carbonate Rocks—A Symposium, Memoir 1: American Association of Petroleum Geologists, Tulsa, Oklahoma. p. 108–121.

Eberli GP, Baechle GT, Anselmetti FS, Incze ML. 2003. Factors controlling elastic properties in carbonate sediments and rocks. The Leading Edge 22:654–660.

Elebiju OO, Matson S, Keller GR, Marfurt KJ. 2011. Integrated geophysical studies of the basement structures, the Mississippi chert, and the Arbuckle Group of Osage County region, Oklahoma. American Association of Petroleum Geologists Bulletin 95:371–393.

Elrick M, Read JF. 1991. Cyclic ramp-to-basin carbonate deposits, Lower Mississippian, Wyoming and Montana; A combined field and computer modeling study. Journal of Sedimentary Research 61:1194–1224.

Espinal L. 2002. Porosity and its measurement. In Kaufmann EN (Editor). Characterization of Materials: John Wiley & Sons, Hoboken, New Jersey. DOI:10.1002/0471266965Evans CS, Newell KD. 2013. The Mississippian Limestone Play in Kansas: Oil and gas in a complex geologic setting, Public Information Circular 33: Kansas Geological Survey, Lawrence, Kansas. http://www.kgs.ku.edu/Publications/PIC/pic33.html. Accessed December 10, 2017.

Gao D. 2011. Latest developments in seismic texture analysis for subsurface structure, facies, and reservoir characterization: A review. Geophysics 76:W1–W13.

Geological Society of America (GSA). 1995. Rock-Color Chart with Genuine Munsell Color Chips, Vol. 8: Geological Society of America, Boulder, Colorado. 8 charts.

Higley DK, Cook TA, Pawlewicz MJ. 2014. Woodford Shale Assessment Units. In Higley DK (Editor). Petroleum Systems and Assessment of Undiscovered Oil and Gas in the Anadarko Basin Province, Colorado, Kansas, Oklahoma, and Texas—USGS Province 58, US Geological Survey Digital Data Series DDS–69–EE: US Geological Survey, Reston, Virginia. p.24.

Jaiswal P, Gregg JM, Parks S, Holman R, Mohammadi S, Grammer GM. 2017. Evidence of fault/fracture ‘‘hydrothermal’’ reservoirs in the southern midcontinent Mississippian carbonates. In Grammer GM, Gregg JM, Puckette JO, Jaiswal P, Mazzullo SJ, Pranter MJ, Goldstein RH (Editors). Mississippian Reservoirs of the Midcontinent, Memoir 116: American Association of Petroleum Geologists, Tulsa, Oklahoma. DOI:10.1306/13632145M1163786

Jones TD, Nur A. 1984. The nature of seismic reflections from deep crustal fault zones. Journal of Geophysical Research: Solid Earth 89:3153–3171.

Kittridge MG. 2014. Investigating the influence of mineralogy and pore shape on the velocity of carbonate rocks: Insights from extant global data sets. Interpretation 3:SA15–SA31.

Kuster GT, Toksöz MN. 1974. Velocity and attenuation of seismic waves in two-phase media: Part I. Theoretical formulations. Geophysics 39:587–606.

Lane HR, De Keyser T. 1980. Paleogeography of the late Early Mississippian (Tournaisian 3) in the central and southwestern United States. In Fouch TD, Magathan ER (Editors). Paleozoic Paleogeography of the West-Central United States, Rocky Mountain Symposium 1: Rocky Mountain Section SEPM, Denver, Colorado. p. 149–162.

LeBlanc SL. 2014. High resolution sequence stratigraphy and reservoir characterization of the ‘‘Mississippian Limestone’’ in North-Central Oklahoma [MS thesis]: Oklahoma State University, Stillwater,. 455 p.

Loucks RG, Reed RM, Ruppel SC, Hammes U. 2012. Spectrum of pore types and networks in mudrocks and a descriptive classification for matrix-related mudrock pores: American Association of Petroleum Geologists Bulletin 96:1071–1098.

MacEachern JA, Bann KL, Gingras MK, Pemberton SG. 2009. Applied Ichnology, Short Course Notes 52: SEPM (Society for Sedimentary Geology), Tulsa, Oklahoma. 380 p.

Matson S. 2015. The Mississippian Lime: Kinematics of a play—Structure, reservoir characterization and production performance of the horizontal Mississippian play: AAPG Search and Discovery Article 110184.

Matson SE. 2013. AV Mississippi Lime Play: From outcrop to subsurface— The evolution of a play: AAPG Search and Discovery Article 110170. Mazzullo SJ, Wilhite BW, Boardman DR II. 2011. Lithostratigraphic architecture of the Mississippian Reeds Spring Formation (Middle Osagean) in Southwest Missouri, Northwest Arkansas, and Northeast Oklahoma: Outcrop analog of subsurface petroleum reservoirs. Shale Shaker 61:254–269.

Miller MF, Smail SE. 1997. A semiquantitative field method for evaluating bioturbation on bedding planes. Palaios 12:391–396.

Misaghi A, Negahban S, Landrø M, Javaherian A. 2010. A comparison of rock physics models for fluid substitution in carbonate rocks. Exploration Geophysics 41:146–154.

Molyneux JB, Schmitt DR. 1999. First-break timing: Arrival onset times by direct correlation. Geophysics 64:1492–1501.

Norris A. 1985. A differential scheme for the effective moduli of composites. Mechanics of Materials 4:1–16.

Norrish K, Taylor RM. 1962. Quantitative analysis by X-ray diffraction. ClayMinerals Bulletin 5:98–109.

Northcutt R, Campbell J. 1995. Geological Provinces of Oklahoma: Oklahoma Geological Survey, Norman, Oklahoma. http://www.ogs.ou.edu/geolmapping/Geologic_Provinces_OF5-95.pdf. Accessed December 10, 2017.

Nur A, Mavko G, Dvorkin J, Galmudi D. 1998. Critical porosity: A key to relating physical properties to porosity in rocks. The Leading Edge 17:357–362.

Price BJ, Grammer GM. 2017. High resolution sequence stratigraphic architecture and reservoir characterization of the Mississippian Burlington/Keokuk Formation, northwestern Arkansas. In Grammer GM, Gregg JM, Puckette JO, Jaiswal P, Mazzullo SJ, Pranter MJ, Goldstein RH (Editors). Mississippian Reservoirs of the Midcontinent, Memoir 116: American Association of Petroleum Geologists, Tulsa, Oklahoma. DOI:10.1306/13632145M1163786

Rashid F, Glover PWJ, Lorinczi P, Hussein D, Lawrence JA. 2017. Microstructural controls on reservoir quality in tight oil carbonate reservoir rocks. Journal of Petroleum Science and Engineering 156:814–826.

Raymer LL, Hunt ER, Gardner JS. 1980. An improved sonic transit time-to-porosity transform. In Proceedings of the SPWLA 21st Annual Logging Symposium, July 8–11, Lafayette, Louisiana: Society of Petrophysicists and Well-Log Analysts, Houston, Texas. p. 1–12.

Reijenstein HM, Posamentier HW, Fantin M, Gonza´lez Tomassini F, Lipinski C. 2014. Vaca Muerta seismic stratigraphy and geomorphology: Regional architectural trends for

unconventional exploration. In Proceedings of the IX Congreso de Exploraci´on y Desarrollo de Hidrocarburos IAPG, November 3–7, Mendoza, Argentina. 8 p.

Roehl PO, Choquette PW. 2012. Carbonate Petroleum Reservoirs: Springer Science & Business Media, New York. 658 p. Rogers SM. 2001. Deposition and diagenesis of Mississippian chat reservoirs, north-central Oklahoma. Association of Petroleum Geologists Bulletin 85:115–129.

Rossebø ØH, Brevik I, Ahmadi GR, Adam L. 2005. Modeling of acoustic properties in carbonate rocks, SEG Technical Program Expanded Abstracts 2005: Society of Exploration Geophysicists, Tulsa, Oklahoma. p. 1505–1508.

Smith TM, Sayers CM, Sondergeld CH. 2009. Rock properties in low-porosity/ low-permeability sandstones. The Leading Edge 28:48–59.

Sun Y, Goldberg D. 1997. Estimation of aspect-ratio changes with pressure from seismic velocities. In Lovell MA, Harvey PK (Editors). Developments in Petrophysics, Special Publications 122: Geological Society, London. p.131–139.

Sun Y-F. 1994. On the foundations of the Dynamical Theory of fractured porous media and the gravity variations caused by dilatancies [PhD dissertation]: Columbia University, New York, 378 p.

Todorovic-Marinic D, Chopra S, Edmonds M. 2011. Advanced seismic techniques help in characterizing a challenging Jean Marie carbonate play, NE British Columbia, Canada—A case study. CSEG Recorder 37:50–59.

Turnini AM, Pranter MJ, Marfurt KJ. 2017. Mississippian limestone and chert reservoirs, Tonkawa Field, north-central Oklahoma. In Grammer GM, Gregg JM, Puckette JO, Jaiswal P, Mazzullo SJ, Pranter MJ, Goldstein RH (Editors). Mississippian Reservoirs of the Midcontinent, Memoir 116: American Association of Petroleum Geologists, Tulsa, Oklahoma. DOI:10.1306/13632145M1163786

Tutuncu AN, Podio AL, Gregory AR, Sharma MM. 1998. Nonlinear viscoelastic behavior of sedimentary rocks, Part I: Effect of frequency and strain amplitude. Geophysics 63:184–194.

Vanden Berg B. 2016. An integrated analysis of carbonate mudrocks and mixed carbonate–siliciclastic reservoirs to define the effects of micro- to nanometer scale pore architecture on the ability to predict porosity or permeability [PhD dissertation]: Oklahoma State University, Stillwater.

Vanden Berg B, Nussbaumer C, Noack A, Thornton J, Weger RJ, Eberli GP, Grammer GM. 2018. A comparison of the relationship between measured acoustic response and porosity in carbonates across different geologic periods, depositional basins, and with variable mineral composition. Interpretation 6:T245–T256.

Vanden Berg BV, Grammer GM. 2016. 2-D pore architecture characterization of a carbonate mudrock reservoir: Insights from the Mid-Continent ‘‘Mississippi Lime.’’ In Olson T (Editor). Imaging Unconventional Reservoir Pore Systems, Memoir 112: American Association of Petroleum Geologists, Tulsa, Oklahoma. p. 185–231.

Vandervoort C. 2011. Data & Drilling Methods from Horizontal Mississippian Reservoirs Across Northern Oklahoma, Workshop on Mississippian Play: Oklahoma Geological Survey, Norman. http://ogs.ou.edu/docs/meetings/OGS-workshop-mississippian_play_2011-vandervoort.pdf. Accessed December 10, 2017.

Wang Z, Wang R, Weger RJ, Li T,Wang F. 2014. Pore-scale modeling of elastic wave propagation in carbonate rocks. Geophysics 80:D51–D63.

Wardlaw N. 1976. Pore geometry of carbonate rocks as revealed by pore casts and capillary pressure. Association of Petroleum Geologists Bulletin 60:245–257.

Watney WL. 2014. Fluid migration and accumulation within the Mississippian: Why 2% oil cut here, 15% oil cut one mile away: AAPG Search and Discovery Article 50953.

Watney WL. 2015. A maturing Mississippian Lime play in the Midcontinent—A perspective on what we know and need to know: AAPG Search and Discovery Article 80445.

Weger RJ, Eberli GP, Baechle GT, Massaferro JL, Sun Y-F. 2009. Quantification of pore structure and its effect on sonic velocity and permeability in carbonates. Association of Petroleum Geologists Bulletin 93:1297–1317.

Wilson EN, Watney WL, Grammer GM. 2017. An overview of the giant heterogeneous Mississippian carbonate system of the midcontinent: Ancient structure, complex stratigraphy, conventional traps and unconventional technology in a high fluid volume world. In Grammer GM, Gregg JM, Puckette JO, Jaiswal P, Mazzullo SJ, Pranter MJ, Goldstein RH (Editors). Mississippian Reservoirs of theMidcontinent,Memoir 116:AmericanAssociation of Petroleum Geologists, Tulsa, Oklahoma. DOI:10.1306/13632145M1163786

Wood A. 1941. A Textbook of Sound: Bell, London. 578 p.

Wyllie MRJ, Gregory AR, Gardner LW. 1956. Elastic wave velocities in heterogeneous and porous media. Geophysics 21:41–70.

Xu S, Payne MA. 2009. Modeling elastic properties in carbonate rocks. The Leading Edge 28:66–74.

Xu SY, White RE. 1995. A new velocity model for clay–sand mixtures. Geophysical Prospecting 43:91–118.

Yenugu M, Marfurt KJ, Matson S. 2010. Seismic texture analysis for reservoir prediction and characterization. The Leading Edge 29:1116–1121.

Zhang J, Li H. 2017. Pore-shape substitution: Separating the effect of microstructure on P- and S-wave velocities, SEG Technical Program Expanded Abstracts 2017: Society of Exploration Geophysicists, Tulsa, Oklahoma. p. 3740–3744.

Zhang T, Dou Q, Sun Y, Zhang H. 2012. Improving porosity-velocity relations using carbonate pore types, SEG Technical Program Expanded Abstracts 2012: Society of Exploration Geophysicists, Tulsa, Oklahoma. p. 1–5.

CHAPTER III

HOW NANOPORES INFLUENCE DRY-FRAME V_P PRESSURE SENSITIVITY

3.1 Abstract

This paper investigates how nanopore size distribution influences dry-frame P-wave velocity (V_P) pressure sensitivity. The study uses a set of twenty-three samples belonging to a single vertical core from the Mississippian-age Meramec formation of the mid-continent US. Individual samples had their facies interpreted, composition estimated, He-gas porosity (Φ_{He}) determined, and P-wave and S-wave transit times systematically measured for dry core-plugs in a 5–40 MPa loading and unloading cycle. Data from the unloading cycle were linearized in the log scale, and the slope of the best fitting line was considered as a representative of the dry-frame V_P pressure sensitivity. A series of photomicrographs from each sample were analyzed using image processing methods to obtain the shape and size of the individual pores, which were mostly in the nanopore (10^{-6}–10^{-9} m) scale. At the outset, the pore-shape distribution plots were used to identify and discard samples with excessive cracks and complex pores. When the remaining samples were compared, it was found that within the same facies and pore-shape distribution subgroups V_P pressure sensitivity increased as the dominant pore-size became smaller. This was largely independent of Φ_{He} and composition. The paper postulates that at the nanopore scale in the Meramec formation, pores are mostly isolated, and an increase in the confining pressure increased the bulk moduli of the fluids in

the isolated pores, which in turn increased the V_P pressure sensitivity. The study proposes incorporating this effect quantitatively through a dual-fluid model where the part of the fluid in unconnected pores is considered compressible while the remaining is considered incompressible. Results start to explain the universal observation of why the presence of microporosity quintessentially enhances V_P pressure sensitivity.

Key Words: digital image analysis, nanopore, p-wave, pressure sensitivity, pore structure

3.2 Introduction

Rocks resist bulk deformation against pressure. This property, known as the bulk modulus (K), is a measure of the volume change with respect to a change in the confining pressure. In a porous material, the change of K is not linear with pressure (Robin (1973); Hart and Wang (1995); Zhang et al. (2019)). Why and how K changes with loading can provide critical insights into the drainage and injection behavior of reservoir rocks, which in turn is necessary for production and sequestration (Angerer et al. (2002); Vanorio et al. (2011); Vanorio (2015)). Volumetric strain can be measured directly in axial loading experiments yielding what is referred to as the "static" modulus. However, measuring small strains in static loading can be difficult and the experiments are often destructive. A common practice is to instead measure the P-wave (V_P) and S-wave (V_s) velocities at ultrasonic frequencies over loading and unloading cycles and, using standard relationships, obtain what is referred to as the "dynamic" modulus (Nur and Simmons (1969); Martínez-Martínez et al. (2012); Asef and Najibi (2013)). For elastic material such as steel, the static and dynamic moduli are essentially the same. For dry porous rocks, however, one reason of the difference between the two is due to a difference in how rock responds to rate and magnitude of loading (Mashinsky (2003); Fjær et al. (2013); Fjær (2019)). For example, the strain rate induced by axial loading (typically, 10^{-6} s^{-1}) is much lower than that induced by ultrasonic frequencies (typically, 10^{-1} s^{-1}) (Fjær et al. (2013); Fjær (2019)) while the strain amplitude in axial loading is higher, e.g., 10^{-2} to 10^{-1} versus 10^{-7} to 10^{-6} (Batzle et al. (2006); Fjær (2019); Muqtadir et al. (2020)).

Likewise, parts of the rock that accommodate that static stress, e.g., compliant features such as a crack (Han et al. (2016)), are different than the parts that contribute to the elastic stress propagation, e.g., grain contacts. Other experimental conditions such as dispersion and drainage can also set dynamic and static moduli apart. Regardless, the goal of geomechanical measurements is not as much to reconcile the two kinds of moduli as to use them for understanding different aspects of the rock and gain predictability of its behavior. This paper focuses on understanding how the pore-size distribution affects the rate at which V_P changes with confining pressure, hereafter referred to as pressure sensitivity.

Static measurements provide stress-strain relationships that can be used for investigating fatigue, relaxation, creep, and rupture. Dynamic measurements provide elastic velocities that can be in turn related to the rock texture and fluid dynamics. Several elastic and elastoplastic models that formulate moduli and velocity in terms of measurable properties such as bulk porosity (Φ) and composition can be explored to explain both static and dynamic modulus and gain insights into the mechanistic nature of the rock (Mavko et al. (2020)). However, challenges remain. Why stress-strain relationships in static experiments with simple Hookean porous rocks are often more non-linear than what is expected from their moduli and texture, remains debated (Morgenstern and Phukan (1969); Biot (1973); Darling et al. (2004)). Similarly, while velocities at a given pressure can be modeled under a set of mechanistic assumptions, being able to explain the entire hysteresis with the same mechanistic model has been rarely done. In dynamic measurements, empirical relationships most commonly emerge between V_P pressure sensitivity, and pore topology (Eberhart-Phillips et al. (1989); Prasad and Manghnani (1997); Kirstetter and MacBeth (2001); David and Zimmerman (2012)). Static experiments also indicate that the nature of the stress-strain curve can be strongly influenced by the pore topology (Fredrich et al. (1993); Davis et al. (2017)). To date, however, for explaining both the dynamic and static results the emphasis has been on using the bulk value of porosity rather than the pore architecture, distribution, or connectivity.

In general, both moduli and velocity of a porous material have several dependencies. Closed-form expressions that view rock as a continuous medium with an even distribution of regular pores can explain the role of key causations such as the composition (grains and fluids) and Φ. Cracks, grain boundaries, and geometrical irregularities are difficult to include in a continuum and are therefore often treated as boundary conditions or an end member problem (Pyrak-Nolte et al. (1990); Liu et al. (2000); Pyrak-Nolte and Morris (2000)). Interestingly, when it comes to the V_P pressure sensitivity, end members might outweigh the contribution of composition and Φ. Assuming that the grains remain intact, it is commonly accepted that increase in V_P due to loading is mainly due to the closure of cracks and grain boundaries (Darot and Reuschlé (2000); Freund (1992); Prasad and Manghnani (1997)) or change in grain arrangement (Kitamura et al. (2010)). In this context, the role of microporosity (pores smaller than what Optical Light Microscopy can discern; ~30 μm; Baechle et al. (2008)) seems to be critical. Despite constituting only a small fraction of Φ their presence is known to strongly influence V_P pressure sensitivity (de Oliveira et al. (2016); Wang et al. (2015)) and possibly both strain rate and amplitude during loading. Microporosity makes the rock behave differently at low and high pressure naturally prompting researchers to conceive dual-porosity models, e.g., Ba et al. (2008), to explain the rock behavior across the entire range of confining pressure. Why and how the presence of pores that are smaller than a certain dimension should affect static or dynamic moduli differently than the rest of the porosity remains unclear.

Unlike that of composition and Φ, understanding the effect of pore shape and size on static or dynamic moduli is not straightforward. Pore aspect ratio (major (l) over minor (w) axis), their orientation, and complexity (perimeter (P_e) over area (A_r)) are theoretically expected to explain how stress accumulates and the material is strained (Zimmerman et al. (1986)). Although, their experimental confirmation is widely available (Weger et al. (2009); Weibo et al. (2020)), the extent of their exclusivity remains unclear. For example, compressibility might not always be tied to

geometry, i.e., the set of compliant features could have a large intersection with the set of features that have a high aspect ratio, but they are not identical. The role of the size distribution probably remains even less explored. With a set of synthetic carbonate samples, Wang et al. (2015) have shown how size affects velocity, which may be a function of the dominant wavelength. In the meso-to-micro range (4 mm – 1μm) , Weger et al. (2009) found that ultrasonic V_P increased as the pores became larger and less complex. On the other hand, in the micro-to-nano range (62.5 μm – 1 nm), Raj et al. (2019) discovered the opposite; they noted that the ultrasonic V_P increased as the dominant pore size decreased. A key difference between the two experiments was that Weger et al. (2009) samples were saturated while Raj et al. (2019) samples were dry. Another difference was that while Weger et al. (2009) compared samples of vastly different pore architectures, Raj et al. (2019) first classified their sample facies-wise and then composition-wise, ensuring that samples of similar pore architecture are compared. Regardless, both studies showed that, at least in the carbonate rocks, the pore-size distribution might play an equally important role in determining the V_P as does Φ.

Almost all existing studies on V_P pressure sensitivity have used rocks with pore-size dominantly in the meso- or larger scale. This paper extends the line of inquiry started by Raj et al. (2019) and fills the knowledge gap of examining how nanopores affect dry-frame V_P pressure sensitivity. Raj et al. (2019) demonstrated the effect of pore-size distribution on V_P with samples from the Mississippian age mixed carbonate-siliciclastic reservoir rocks from the mid-continent, USA, commonly known as the "Miss Lime" formation. This paper uses samples from the distal equivalent of Miss Lime, known as the Meramec formation. The dataset in this paper comprises X-ray diffraction (XRD)-based composition, Φ_{He} from helium injection porosimetry, ultrasonic velocities of ~1.5-inch dry core plugs over 5 - 40 MPa loading and unloading cycle, and pore-size distribution from Digital Image Analysis (DIA) of Scanning Electron Microscopy (SEM)

photomicrographs of twenty-three samples. Although the results are presented in the context of dynamic modulus, the idea can be extended to understand static measurements as well.

3.3 Study Area

The study area, which is in present-day Oklahoma, was situated 10°-15° south of the paleo equator in the Mississippian epoch (359-323 Ma) (Lane and De Keyser (1980); Blakey (2013); Mazzullo et al. (2011)). The Mississippian epoch was a transitional period moving from a greenhouse to an icehouse environmental condition that resulted in an overall regressive coastline (Buggisch et al. (2008); Haq and Schutter (2008)). This led to the development of an extensive east-west trending carbonate shelf on a shallow tropical epeiric sea over Devonian-age Woodford Shale (Gutschick and Sandberg (1983)). The architecture of this shelf was dominated by both tectonism and higher-order eustatic sea-level changes resulting in high-frequency transgressive-regressive shallowing upward cycles (Childress and Grammer (2015); Mazzullo et al. (2011); Watney et al. (2001)). The shelf development ceased in the late Mississippian due to uplift and erosion associated with Gondwana and Euramerica collision. The Mississippian strata record a transition in composition from the shallow-water Miss Lime carbonates in the north (Watney et al. (2001)) to deep-water mixed carbonate-siliciclastic sediments in the Anadarko and Ardmore basin in the south (Price et al. (2017)). Currently, from north to south, several laterally and vertically varying proximal and distal facies comprising various permutations of limestones, chert, and silicified limestone with depositional and diagenetic pore systems are found with a gradation in grain size and mineral chemistry depending on their distance from the shoreline.

The Mississippian-age reservoirs are mainly sourced by the underlying Devonian-age Woodford shale and ultimately capped by the overlying Pennsylvanian-age transgressive shale. The core used in this study lies in the Meramec formation of the Sooner Trend Anadarko Canadian and Kingfisher (STACK) play in the Anadarko Basin. At the core location (Figure 3.1), the Meramec formation is located above the Devonian-age Woodford (shale) formation and is overlain

by Pennsylvanian-age Morrow (carbonate) formation (Miller et al. (2019)). Compositionally, the Meramec formation is a mixed carbonate-siliciclastic system with Φ in the range of 1-6% and permeability in the range of 0.1 to 10 mD (Almasoodi et al. (2020)). The main reason why the Meramec formation is gaining popularity with the operators is its overpressured nature and low water content that resulting in high initial production (IP) rate (Chopra et al. (2018)). The sustained production, such as in the other tight reservoirs, however, requires a detailed understanding of the pore architecture and connectivity.

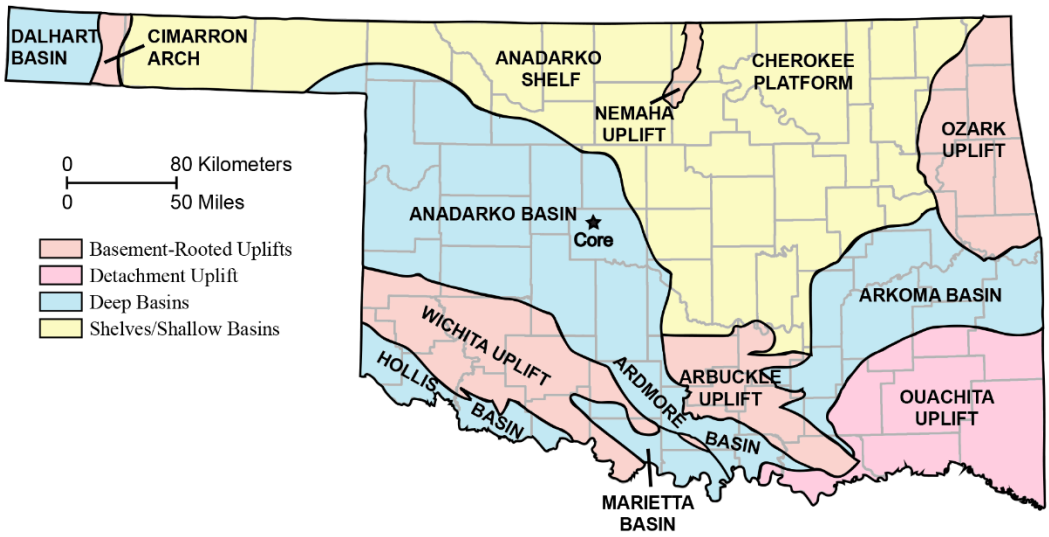

Figure 3.1 Base Map. Major geological features within the state boundary of Oklahoma are labeled (after Northcutt and Campbell (1996)). Solid star is the core location.

3.4 Dataset

The core used for this study is located in Canadian County, Oklahoma, and contained ~152.5 m (500 ft) thick Meramec formation. First, the Meramec facies were interpreted. Then, within the access restrictions, 23 core plugs with 1.5-inch (3.8 cm) diameter and ~2 in (5.1 cm) length were extracted ensuring that the key facies were adequately sampled. A small (~0.5 cm) portion from one end was sawed and separated for XRD and SEM photomicrography, and the

remainder of the core plug was used for ultrasonic transit-time measurement under loading and unloading conditions and Φ_{He} measurement using helium gas porosimetry.

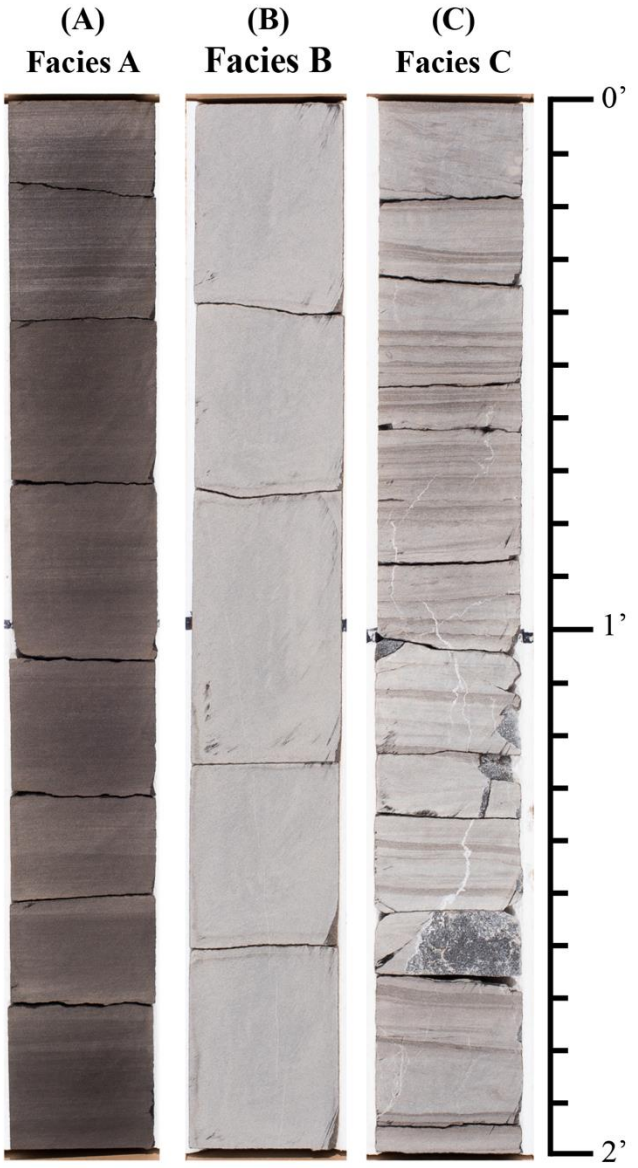

Figure 3.2 Facies. **(A)** A: mudstone to siltstone with scattered sedimentary features such as lamination, burrowing and bioturbation, **(B)** B: massive bedded packstone to grainstone, and **(C)** C: hummocky cross-stratified-planar laminated packstone to grainstone. Transitions from Facies A – C represent a change from distal to proximal shelf depositional environment.

3.4.1 Facies Interpretation

In the core, the start and end of the Meramec formation was identified using color change from the bounding Devonian and the Pennsylvanian shales (LeBlanc (2014); Vanden Berg and

Grammer (2016)). Within the Meramec Formation, the facies interpretation was based on differences in texture, composition, sedimentary structures, trace fossils (MacEachern et al. (2009)) and color (Geological Society of America (1995)). Three facies, hereafter referred to as A, B, and C, were dominant in the core (Figure 3.2). Facies A (Figure 3.2A) was laminated siltstone and had millimeter thick black dark brown mud rich and gray calcite-rich layering. It had scattered trace fossils with a variable abundance of brachiopods and crinoids. Facies B (Figure 3.2B) was a massive-bedded packstone-grainstone. It was grayish with a dominant massive-bedded structure and had abundant skeletal trace fossil fragments of brachiopods, crinoids, and peloids. Facies C (Figure 3.2C) was a hummocky cross-stratified and planar-laminated packstone-grainstone. It was darker than Facies B and was abundant in skeletal trace fossil fragments of brachiopods, crinoids, and peloids.

3.4.2 Digital Image Analysis

For DIA, a small portion from the 0.5 cm disk was cut and polished using a JEOL IB-19500 CP argon-ion mill machine. The ion-milled samples were kept in a vacuum for 2 hours and sputter-coated with gold/palladium coating using a Balzers MED 010 machine for 20 seconds. The photomicrographs were captured with FEI Quanta 600F field emission SEM (Figure 3.3A). The photomicrographs were then analyzed in grayscale using the Leica's Application Suite (LAS). Typically, pores and organic matters appear as darker features whereas grains appear as lighter features in SEM photomicrographs. At core location, it is unlikely to contain organic matter (Miller et. al (2019)). So, whenever possible, as a rule of thumb, the darker features were interpreted as "pores" while the lighter features were considered as "grains" (Figure 3.3B). Occasionally, when the distinction of boundary between pores and grains was not obvious, coherency filters were used to make the parts of the image clearer. All photomicrographs were analyzed individually, and every step of DIA was carefully monitored to avoid imaging and interpretational artifacts.

The software measured P_e, A_r, l and w of an individual pore in terms of pixels (inset; Figure 3.3B). All pixels along the periphery of a pore contributed to P_e, and all pixels lying within and on the pore-periphery contributed to A_r. The l and w of the pore were the length and width of a rectangle that tightly enclosed the pore. The spatial orientation of the rectangle was not relevant to the analysis in this paper. After counting the pixels, the software assigned a metric length or size to individual features using the magnification set by the user. In this application, 1.5 nm was heuristically set as the limit of resolution of the SEM photomicrographs, and features below this size were not interpreted. Finally, for every sample, a database with the architectural parameters of all the pores interpreted in its photomicrographs was created.

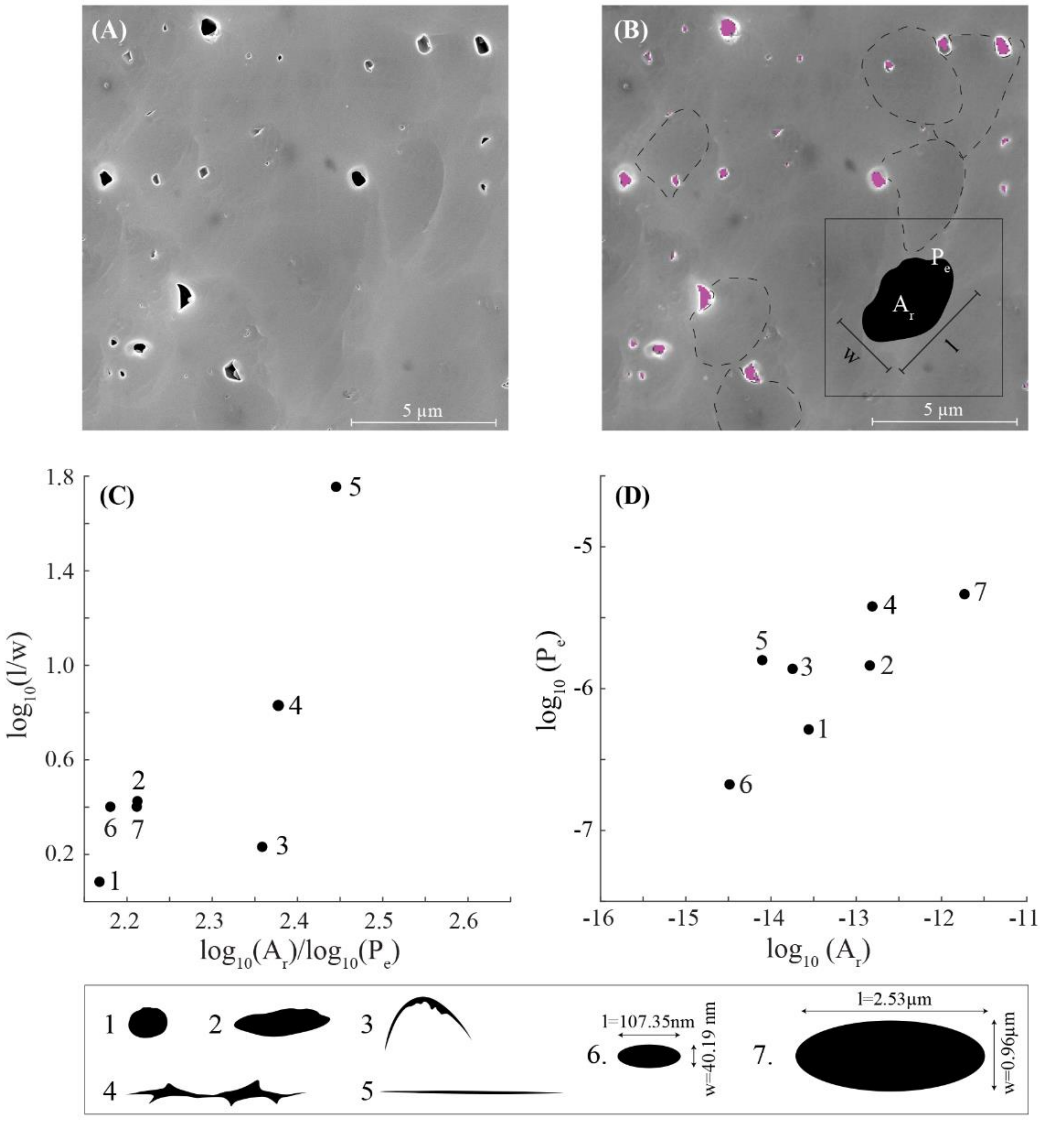

Figure 3.3 Digital Image Analysis (DIA). **(A)** Representative SEM photomicrograph, **(B)** same as (A) showing pores identified by DIA in solid color and grain boundaries in dashed line. Inset shows a cartoon of pore and the corresponding parameters, length [l], width [w], area [A_r] and perimeter [P_e], that is measured by DIA, **(C)** $\log_{10}(A_r)/\log_{10}(P_e)$ versus $\log_{10}(l/w)$, and **(D)** $\log_{10}(A_r)$ versus $\log_{10}(P_e)$ crossplots. Note that shapes are better resolved in (C) while sizes are better resolved in (D).

3.4.3 Ultrasonic Velocity

Transit times corresponding to P- and two independent orthogonally polarized S-waves were recorded for all core plugs in dry conditions using New England Research Autolab 1000. Saturated-rock measurements were not attempted because of the difficulties in ensuring that samples achieve a complete saturation. Each plug was inserted in a rubber sleeve before setting it between a transducer-receiver assembly. The entire assembly was then put inside a pressure chamber filled with mineral oil. The central frequency of the transducer generated wave signals was 1 MHz for both P- and S-waves. The confining pressure within the pressure chamber was systematically and gradually increased from 5 MPa to 40 MPa (loading) and then decreased to 5 MPa (unloading). Assuming a hydrostatic gradient of 3.102 kPa/ft (10.18 kPa/m), this pressure range was intended to mimic a burial depth from ~1612 ft to ~12,895 ft which encompassed the reservoir depth in the core of 10400-10900 ft (~3170-3322 m). Transit times were recorded at 5, 10, 15, 20, 30, and 40 MPa in both segments (Figure 3.4A). Measurements at 30 MPa best corresponds to the reservoir conditions which, assuming a hydrostatic gradient, varied from 32.27 MPa to 33.81 MPa. First arrivals in the waveforms were picked manually and converted to velocities using the known sample dimension and instrument-related parameters (Figure 3.4B). The average uncertainty due to first arrival time picking of P-wave and S-waves were less than 1.25% and 2%, respectively. Only unloading cycle measurements are used in this paper following the

common practice in the art where it is assumed that the loading cycle has permanently closed stress cracks that originated from the core first being exposed to the atmospheric conditions.

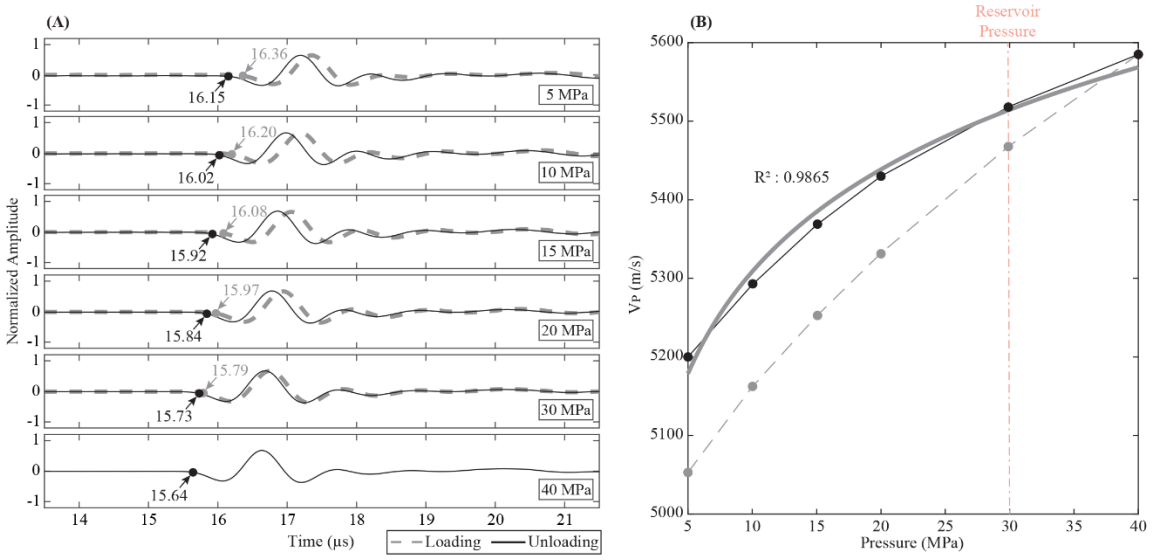

Figure 3.4 P-wave velocity (V_P) estimation. **(A)** Representative ultrasonic waveforms for loading (dashed gray) and unloading (solid black) segments. The corresponding gray and black dots are the interpreted P-wave first arrival times, which are then converted to V_P based on known sample length and instrument calibration constants. Confining pressures for individual waveforms are mentioned. **(B)** V_P pressure sensitivity for loading (dashed gray) and unloading (solid black) segments. The thick gray line represents a function of the form $V_P(P_C) = s + r_P \log_{10}(P_C)$ that is fit to the unloading cycle. For data in (A), a high correlation coefficient ($R^2 = 0.9865$) is obtained. The process is repeated for P-, S1- and S2-waves for all 23 samples (Figures S3-S14). A high value of r implies a higher-pressure sensitivity.

3.4.4 He-gas Porosimetry

Φ_{He} measurement was done using a helium gas injection technique on all core plugs using an AccuPyc II 1340 Pycnometer. The pycnometer uses helium-gas displacement to measure solid phase volume. The instrument has a sample chamber and a precision chamber. The core plug was put first in a compartment of known volume, which was then placed in the sample chamber and sealed. Helium filled the sample chamber and equilibrated. The gas was then allowed to flow into the precision chamber and equilibrate. The pressure-drop as a result of discharge of helium-gas into the empty precision chamber from the sample chamber provides the solid phase volume. Before

using the pycnometer, the bulk volume of the core plugs was estimated by measuring diameter and length with a vernier caliper. Φ_{He} is the ratio of the difference between the bulk and the solid phase volume and the bulk volume. Data are mentioned in Table 3.1, 3.2 and 3.3.

3.3.5 Composition

Mineralogy was quantified using XRD. First, the samples were powdered in SPEX ball mill. Powdered samples were then analyzed in Rigaku MiniFlex Diffraction instrument. A quartz sample was used to calibrate the machine before analyzing any sample. Mineralogy was identified using standard Powder Diffraction File and quantified using Rietveld refinement scheme in RIQAS software. Data are tabulated in Table 3.1, 3.2 and 3.3.

Table 3.1: Facies A sample properties.

Group	Panel	Depth (ft)	Porosity (%)	Quartz (%)	Carbonate (%)	Clay (%)	Others (%)	r_P	r_{S1}	r_{S2}
G_{AI}	A.1 & B.1	10450.20	3.70	48.5	3.4	30.5	17.6	96.3	41.9	41.5
	A.2 & B.2	10670.30	3.70	47.1	12.0	22.9	18.0	100.9	36.1	28.4
G_{AII}	C.1 & D.1	10826.30	1.25	47.6	20.7	18.2	13.5	62.0	115.5	76.6
	C.2 & D.2	10630.15	3.28	48.0	16.9	17.3	17.8	107.9	25.3	31.2
	C.3 & D.3	10532.00	3.83	54.9	19.7	12.1	13.3	114.7	28.1	30.6

Table 3.2: Facies B sample properties.

Group	Panel	Depth (ft)	Porosity (%)	Quartz (%)	Carbonate (%)	Clay (%)	Others (%)	r_P	r_{S1}	r_{S2}
G_{BI}	A.1 & B.1	10640.25	2.07	26.6	57.5	6.4	9.5	159.4	69.0	69.3
	A.2 & B.2	10639.90	2.41	30.7	53.4	5.7	10.2	236.6	84.4	84.5
G_{BII}	C.1 & D.1	10694.15	1.11	31.7	54.8	4.2	9.3	87.7	28.3	34.6
	C.2 & D.2	10696.00	2.09	34.7	55.3	3.2	6.8	187.5	76.6	74.7
	C.3 & D.3	10650.15	4.16	52.4	27.1	7.1	13.4	200.0	114.5	124.0

Table 3.3: Facies C sample properties.

Group	Panel	Depth (ft)	Porosity (%)	Quartz (%)	Carbonate (%)	Clay (%)	Others (%)	r_P	r_{S1}	r_{S2}
G_{CI}	A.1 & B.1	10580.90	2.66	47.0	38.0	4.6	10.4	112.4	44.0	49.0
	A.2 & B.2	10700.15	2.96	37.3	47.5	3.8	11.4	243.4	85.0	122.9
G_{CII}	C.1 & D.1	10490.15	2.80	47.8	33.3	6.6	12.3	55.9	25.9	21.0
	C.2 & D.2	10600.85	2.31	45.4	30.2	10.5	13.9	73.9	25.8	49.3

3.5 Data Analysis

We had eleven samples in facies A, and six each in B and C, respectively. We fitted the unloading cycle of the P-wave with the following linear trend (Figures S3-S6 in Supplementary Figures):

$$V_P(P_C) = s + r_P \log_{10}(P_C), \tag{3.1}$$

where s and r_P are the intercept (measurement at 5 MPa) and gradient, respectively, and P_C is confining pressure. For the purpose of this paper, r_P represents the V_P pressure sensitivity. Equation 3.1 could be fit to data from all samples with sufficiently high correlation (R^2 >0.95).

Contoured two-dimensional (2D) histograms were used to analyze the pore shape and size distribution for every sample. Two sets of plots were generated. The first set was along the lines of Figure 3.3C, which is a crossplot between $\log_{10}A_r/\log_{10}P_e$ and $\log_{10}(l/w)$, binned to best preserve the continuity of the distribution. A bin size of 20 was found to be optimal for this kind of plot. Visualizing data in this manner provided an overview of the pore-shape distribution without much regard to their size. Displaying the pore architectural parameters along the lines of Figure 3.3C was necessary to identify samples with excessive cracks and complex pores. Because these features strongly affect V_P pressure sensitivity, it was necessary to discard such samples for this paper to avoid bias. Samples discarded using Figure 3.3C as a guide are shown in Figure S2. This reduced

the number of samples for further analysis to five in Facies A (Figure 3.5), five in Facies B (Figure 3.6), and four in Facies C (Figure 3.7). The second set of plots were along the lines of Figure 3.3D, which is a crossplot between $\log_{10}A_r$ and $\log_{10}P_e$ of the individual pores, binned to best preserve the continuity of the distribution, e.g., Raj et al. (2019). Visualizing data in this manner provided an overview of the pore-size distribution without much regards to the shape. A bin size of 15 was found to be optimal for this kind of plot.

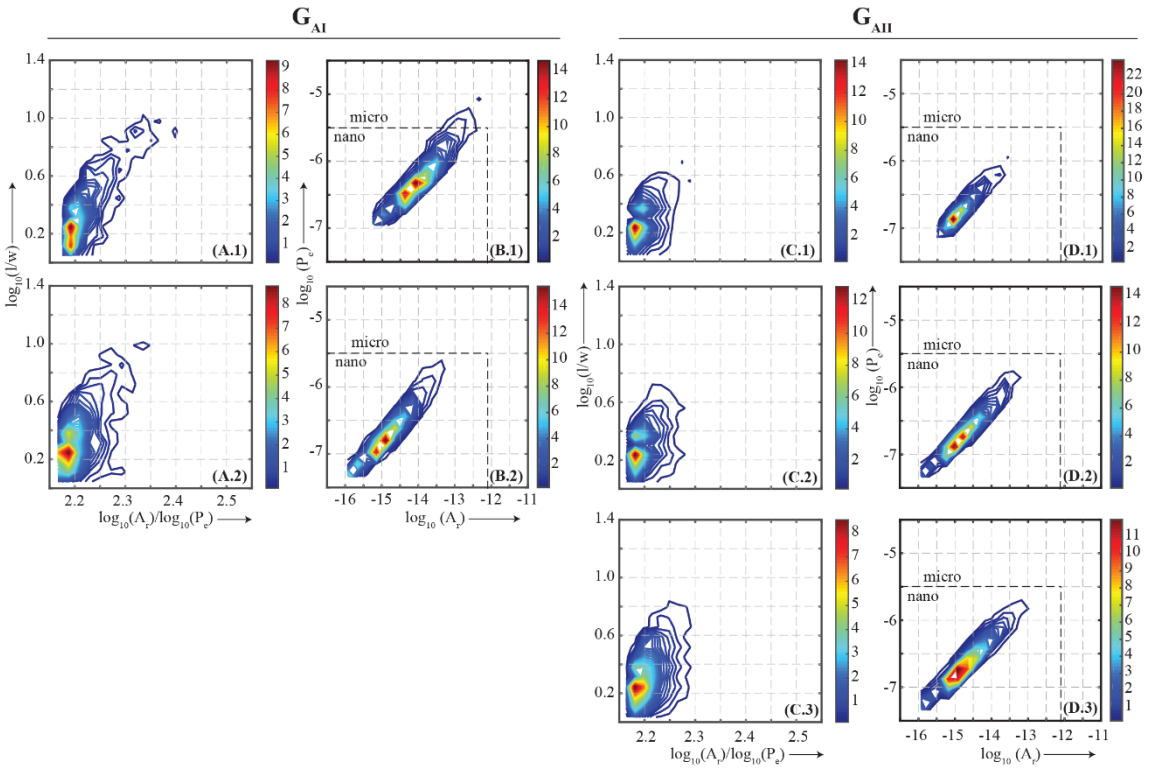

Figure 3.5 Facies A. Contoured histograms of pore l, w, A_r, and P_e are binned and plotted along the lines of Figure 3.3C to visualize pore-shape (**A.1-2** and **C.1-3**) and Figure 3.3D to visualize pore-size (**B.1-2** and **D.1-3**) distributions. Based on the pore-shape distribution, samples are classified into two groups, G_{AI} (**A.1-2** and **B.1-2**) and G_{AII} (**C.1-3 and D.1-3**). In (A) – (D), warm color indicates higher pore population. In (**B.1-2**) and (**D.1-3**), a dashed line separates micro- (1-62.5 µm) and nano- (1 nm-1 µm) pores. Sample depth, porosity, composition and r-value corresponding to P- (r_P), S1- (r_{S1}) and S2- (r_{S2}) waves are mentioned in the table 3.1. The figure indicates that within the same pore-shape distribution, r_P increases as the dominant pore-size decreases.

Raj et al. (2019) classified their samples first based on facies and then their composition. In this paper we use the pore-shape distribution instead of composition as the second criterion for

two reasons. First, samples in this paper were not as compositionally diverse as Raj et al. (2019), and second, a peer study, Baechle et al. (2008), found that pore-shape rather than the composition may have a stronger influence on V_P pressure sensitivity. Within each facies, broad pore-shape subgroups were identified and within each subgroup, samples were arranged in increasing order of r_P.

In Facies A two pore-shape groups, G_{AI} and G_{AII}, were interpreted (Figure 3.5). Group G_{AI} (Figures 3.5A.1 and 3.5A.2) dominantly have pores with an aspect ratio ~1.7 and a subset that extends into the complex and elongated domain with a pore aspect ratio of as much as up to 10. Group G_{AII} (Figures 3.5C.1 – 3.5C.3) dominantly have pores with an aspect ratio between ~1.6 and an overall tendency of the pores to remain concentrated around this geometrical shape. The pore-size distribution plots for Group G_{AI} (Figures 3.5B.1 and 3.5B.2) show a decrease in the dominant pore size depicted by a shift in the warmest color as r_P increases from 96.3 to 100.9. Changes in the pore-size distribution plots for Group G_{AII} are more subtle. From Figure 3.5D.1 to Figure 3.5D.2, as r_P increase from 62.0 to 107.9, the dominant size does not change as much, e.g., the dominant pore size maintains its location, but the pore population includes more pores that are smaller than the smallest pore in Figure 3.5D.1. Likewise, From Figure 3.5D.2 to Figure 3.5D.3, as r_P increase from 107.9 to 114.7, the overall distribution does not change but the dominant pore size becomes more pronounced.

In Facies B two pore-shape groups, G_{BI} and G_{BII}, are interpreted (Figure 3.6). Group G_{BI} (Figures 3.6A.1 and 3.6A.2) dominantly have pores with an aspect ratio between ~1.8 and ~2.5 and a subset that extends into the complex and elongated domain with a pore aspect ratio of as much as up to 16. Group G_{BII} (Figures 3.6C.1 – 3.6C.3) dominantly have pores with an aspect ratio between ~1.7 and ~2.3 and an overall tendency of the pores to remain concentrated around this geometrical shape with a pore aspect ratio below 10. The pore-size distribution plots for Group G_{BI} (Figures 3.6B.1 and 3.6B.2) show an overall decrease in the dominant pore size without much change in the

pore-size distribution as r_P increases from 159.4 to 236.6. Changes in the dominant pore-size distribution for Group G_{BII} are more obvious although the overall pore-size distribution itself does not change much. From Figure 3.6D.1 to Figure 3.6D.2, as r_P increase from 87.4 to 187.5, the dominant pore size shift towards smaller size and becomes more pronounced. Likewise, from Figure 3.6D.2 to Figure 3.6D.3, as r_P increase from 187.5 to 200.0, the dominant pore size shifts toward the smaller size.

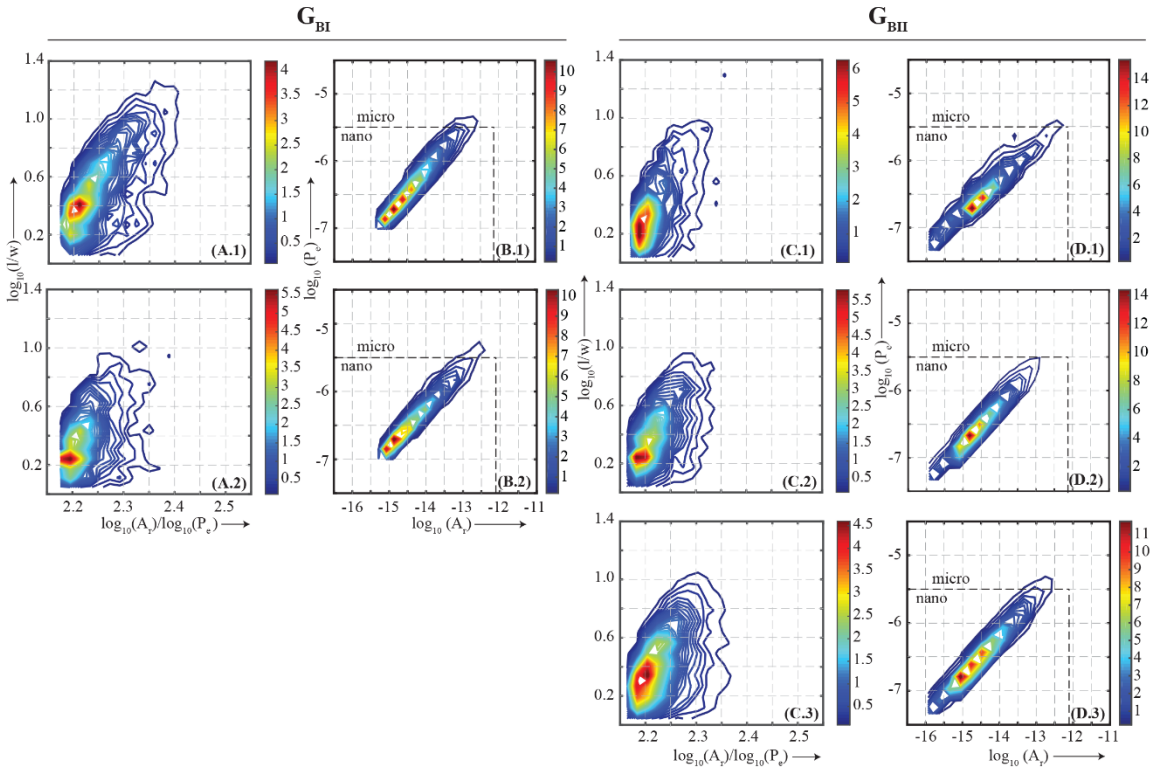

Figure 3.6 Facies B. Symbols and labels are the same as in Figure 3.5. Sample depth, porosity, composition and r-value corresponding to P- (r_P), S1- (r_{S1}) and S2- (r_{S2}) waves are mentioned in the table 3.2. The figure indicates that within the same pore-shape distribution, r_P increases as the dominant pore-size decreases.

In Facies C as well, two pore-shape groups, G_{CI} and G_{CII}, are interpreted (Figure 3.7). Group G_{CI} (Figures 3.7A.1 and 3.7A.2) dominantly have pores with an aspect ratio ~1.4 and an overall tendency of the pores to remain concentrated around this geometrical shape with an aspect ratio below 6.5. Group G_{CII} (Figures 3.7C.1 and 3.7C.2) dominantly have pores with aspect ratio ~1.9 and an overall tendency of the pores to remain concentrated around this geometrical shape

with pore aspect ratio below 10. The pore-size distribution plots for Group G_{CI} (Figures 3.7B.1 and 3.7B.2) show a decrease in the dominant pore size as r_P increase from 112.4 to 243.4. Likewise, changes in the dominant pore-size distribution for Group G_{CII} are also more obvious. From Figure 3.7D.1 to Figure 3.7D.2, as r_P increase from 55.9 to 73.9, the dominant pore size shift towards smaller size and becomes more pronounced. In Facies C, the effect of dominant pore size is more pronounced for both the groups.

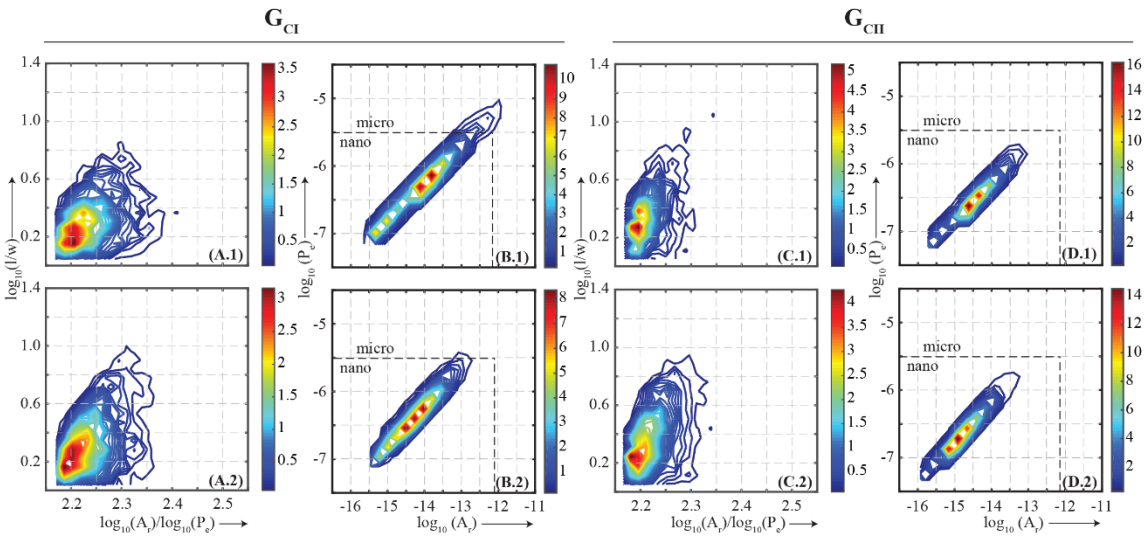

Figure 3.7 Facies C. Symbols and labels are the same as in Figure 3.5. Sample depth, porosity, composition and r-value corresponding to P- (r_P), S1- (r_{S1}) and S2- (r_{S2}) waves are mentioned in the table 3.3. The figure indicates that within the same pore-shape distribution, r_P increases as the dominant pore-size decreases.

Thus, at the core of this paper was examining how pore-size distribution affects V_P pressure sensitivity in samples that have a similar pore-shape distribution. Overall, Figures 3.5 – 3.7, suggest within the same pore-shape distribution the V_P pressure sensitivity increased as the dominant pore size decreased regardless of composition and Φ_{He}.

3.6 Discussion

3.6.1 Nanopore imaging

Of all measurements performed for this paper, using DIA to quantify the pore-size distribution was the most challenging. When pores are fully connected, Φ_{He} and pore-size distribution down to nano-scale can be realized through porosimetry or pulse decay methods (Anovitz and Cole (2015)). Regardless of the connectivity, when pores are large (micro- and greater), micro-computerized-tomography scanning can provide a sense of its architecture (Dong and Blunt (2009)). Imaging becomes increasingly more difficult as pores get smaller and isolated. For nanopores, such as the subject of this paper, direct visualization can only be obtained through SEM in 2D or Focused Ion Beam SEM in 3D. However, because of the small sample size (1-2 mm) representativeness of the pore size and distribution plots, e.g. Figures 3.5 – 3.7, is always in question. Determining what fraction of the imaged pores are connected and if so to what extent and whether they behave similarly outside the sample under investigation is interpretive but due to the intensity of the data collection process, inferences have to be made on a limited number of samples. Emerging studies (Dvorkin et al. (2011); Dvorkin and Derzhi (2012); Andrä et al. (2013); Karimpouli and Tahmasebi (2016); Berg et al. (2017)) have shown that even with limited sampling, an interpreter's experience and judgement can allow extracting dependable results from DIA.

3.6.2 Nanopores and dry ultrasonic velocities

Neither Raj et al. (2019) nor their peer provided a reason as to why the dominant pore-size should affect V_P, although Raj et al. (2019) did observe that the nanopore size (10^{-9}-10^{-6} m) is in the range of strain amplitude caused by P-wave at ultrasonic frequency. Using a set of synthetic carbonate samples, Wang et al. (2015) have previously suggested that it is the dominant wavelength of the propagating wave that decides how pore-size influences the wave velocity. Results in this paper provide opportunities to explore an additional factor. Along with the P-wave arrival times, the authors measured two orthogonal S-wave arrival times under the same confining pressures.

Using an equation similar to Equation 3.1, V_S pressure sensitivity was also computed and the corresponding gradients, r_{S1} and r_{S2}, are mentioned in Tables 3.1-3.3. Fitting of V_S data is shown in Figures S7-S14. Figures 3.5-3.7 and Tables 3.1-3.3 show that unlike their V_P counterparts, V_S pressure sensitivity does not have any obvious correspondence to the dominant pore size. Because S- and P-wave frequencies in the experiment were same, one could argue that if pressure sensitivity is only a pore-size compounded with wavelength phenomenon, V_S pressure sensitivity should have reflected the same trend as V_P pressure sensitivity. Because S-waves are largely transparent to fluids, the V_P pressure sensitivity may therefore be due to pore fluids. The reader is reminded that the experiment being conducted in dry conditions imply that pores are air-filled.

3.6.3 Nanopores influence on bulk moduli – pore isolation and size effects

For discussion, consider pores as void spaces devoid of any inherent physical property. Consequently, its compressibility is essentially the aggregate compressibility of the mineral grains surrounding it in addition to how tightly the grains fit into each other. In a scenario where grains fit seamlessly around the pore, the distortion of the grains under static or harmonic pressure changes is manifested as the distortion of the pore itself, which in turn stimulates the trapped pore fluid. For an isolated pore at constant temperature, how the bulk modulus of trapped fluid changes can be understood to the first order of approximation using the ideal gas equation as follows:

$$PV = nRT \tag{3.2}$$

$$dP.V + P.dV = 0 \tag{3.3}$$

$$-V\left(\frac{dP}{dV}\right) = P, \tag{3.4}$$

where -V(dP/dV) is the same as K. According to Equations 2 – 4, K remains proportional to the pore pressure, which, in turn, is the same as the confining pressure under isothermal conditions. Thus, in principle, the bulk modulus of fluids trapped in an isolated pore will increase with an increase in confining pressure. The effect should be more pronounced in compliant pores. A stiff pore may not display the same phenomenon. Regardless, this explains one way through which V_P

can increase in presence of isolated pores. However, it does not explain why V_P sensitivity will increase with decreasing pore size unless one assumes that the smaller the pore, the more likely it is to occur in isolation. In the Meramec formation, this is like. Processes such as cementation, carbonate pressure dissolution, and clay diagenesis that remain active throughout the burial history can create isolated pores that are independent of the pore network created during sedimentation or even fractures from subsequent tectonics. In the Mississippian-age rocks of the study area, such processes have been widely recorded (Vanden Berg and Grammer (2016); Vanden Berg et al. (2018); Bode et al. (2019)).

Two factors might together be contributing to the observed increase in V_P pressure sensitivity with decreasing pore size. The primary factor might not directly be the size itself. The smaller pore size in the Meramec formation might imply a greater probability of the pore remaining isolated. Figs 3A–B, suggest presence of both intercrystalline and intracrystalline isolated pores in the Meramec formation. It is understood that a number of interpreted pores in Figs 3A–B maybe connected in the third dimension. Regardless, stress from static loading can localize along the grain boundaries and can readily strain the isolated intercrystalline pores increasing the bulk moduli of the trapped fluids. Likewise, the intracrystalline isolated pores in soft grains such as that of clay and organic matter, can also get strained from static loading. Wave propagation through a "stiffer" fluid would manifests as high V_P. The second factor might be the investigation tool itself, which creates particle displacements in the nanopore range (10^{-6} – 10^{-8} m; O'Sullivan et al. (2016); Nourifard and Lebedev (2019)). When ultrasonic waves traverse a pore larger than the strain amplitude, different parts of the pore would get distorted at different instances. On the other hand, smaller pores are expected to be compressed (or dilated) in their entirety at the same instance. Thus, a nanopore dominated system such as the Meramec formation might just be best displaying the effect of the fluid bulk-moduli increase due to static loading on V_P. Because the strain amplitude

remains comparable across a wide range of seismic frequencies (Hz – MHz), the effect of isolated pores on V_P in the Meramec formation might be observable in logs and surface seismic.

3.6.4 Dual-fluid model

Independent research exploring fluid behavior in nanopores also exists which is worth reviewing. Gor et al. (2015) and Dobrzanski et al. (2018) have argued that the thermodynamic behavior of fluids trapped in nanopores may be different than the same fluids in the bulk. Like in this paper, they have found that the bulk modulus of the fluid increases as the pore size decreases. However, the experimental confirmation of the theoretical development in these initiatives was done using tools and techniques that are similar to this study. Thus, it may not be unfair to say that whether fluid thermodynamics at the nanoscale is fundamentally different or it manifests differently due to the investigation tool (seismic), could remain an open-ended question.

If indeed V_P sensitivity is due to fluids in unconnected pores, the next obvious question is how to include the fluid effect in numerical models. In unstressed rocks, the fluid-solid and fluid-fluid particle interactions during elastic wave propagation can be accounted for through two end-member frameworks: a) Biot's, where pores vibrate but do not distort (Biot (1956a, 1956b)); and b) squirt flow, where pores undergo harmonic deformation (Dvorkin et al. (1994); Dvorkin et al. (1995)). Both end-members assume complete pore connectivity. As long as pore connectivity is maintained, Biot's equation can also be adjusted for pre-stressed conditions (Gutierrez and Lewis (2002)). Fluids in unconnected pores are not accounted for directly. In Biot's framework, unconnected pores are part of the solid matrix, e.g., like a separate grain. In other popular models such as differential effective medium, self-consistent, and Kuster-Toksöz, pores are treated as inclusions with specific geometries within a background matrix (Mavko et al. (2020)). Models for unconnected pores consider pore shapes to remain unchanged and the pore-fluids to remain immobile during the elastic wave propagation.

To include V_P pressure sensitivity in numerical models, the paper proposes the use of a dual-fluid model where a part of the porosity, e.g., the microporosity, may be seen as isolated containers filled with compressible fluids versus the rest of the rock that is filled with incompressible fluid. The idea build along the lines of dual-porosity (Pride and Berryman (2003a, 2003b)) and dual stiffness (Liu et al. (2009); Zhao and Liu (2012)) models, but does not require partitioning the pore topology or strain explicitly. In the proposed model, the pore fluid would be separated into a compressible and an incompressible part. The K of the compressible part would remain proportional to the confining pressure while K of the incompressible part would remain unchanged. The proposed model can be implemented within existing frameworks such as Biot's and differential effective medium to explain the behavior of the same rock at different confining pressure and might provide a graceful way of accounting for microporosity whose presence is known to quintessentially enhance V_P pressure sensitivity in both static and dynamic experiments.

3.7 Conclusion

Using a set of 23 samples belonging to a vertical core from the Mississippian-age mixed carbonate-siliciclastic Meramec formation, this study found that the dry-frame V_P pressure sensitivity can depend on pore shape and size distribution. In the study, these distributions were obtained by first measuring P_e, A_r, l, and w of the individual pores through DIA of SEM photomicrographs and then displaying them as 2D histograms of A_r/P_e–l/w and A_r-P_e crossplots. The parameter representing V_P pressure sensitivity was obtained by first measuring the P-wave transit times at ultrasonic frequencies under a 5 – 40 MPa loading and unloading cycle and then fitting a line to the data from the unloading cycle linearized in the log scale. In samples within the same facies that had a similar pore-shape distribution, V_P increased more rapidly with confining pressure as the dominant pore-size, which was in the nanopore range, decreased. The phenomenon was largely independent of composition and Φ_{He} and only applicable to samples that did not have excessive amounts of cracks and complex pores. The observation is explained by postulating that

the pores were mostly isolated at the nanopore scale and an increase in confining stress increased the bulk moduli of the trapped fluids, which in turn increased the V_P. The paper concludes that, in the Meramec formation, a) the likelihood of pores becoming isolated became higher as their size decreases, b) V_P pressure sensitivity was a function of fluid (air) behavior in isolated pores, and c) the effect was prominent because a nanopore dominated system ($<10^{-6}$ μm) was being investigated by frequencies that had comparable strain amplitudes. The study proposes incorporating this effect numerically through a dual-fluid model where fluids in the isolated pores are considered compressible while the remaining are considered incompressible. Results start to explain the common observation of why presence of microporosity quintessentially increases V_P pressure sensitivity.

3.8 References

Almasoodi, M., Vaidya, R., and Reza, Z., 2020, Drawdown-Management and Fracture-Spacing Optimization in the Meramec Formation: Numerical-and Economics-Based Approach: SPE Reservoir Evaluation & Engineering.

Andrä, H., Combaret, N., Dvorkin, J., Glatt, E., Han, J., Kabel, M., Keehm, Y., Krzikalla, F., Lee, M., and Madonna, C., 2013, Digital rock physics benchmarks—Part II: Computing effective properties: Computers & Geosciences, v. 50, p. 33-43.

Angerer, E., Crampin, S., Li, X. Y., and Davis, T. L., 2002, Processing, modelling and predicting time-lapse effects of overpressured fluid-injection in a fractured reservoir: Geophysical Journal International, v. 149, no. 2, p. 267-280.

Anovitz, L. M., and Cole, D. R., 2015, Characterization and analysis of porosity and pore structures: Reviews in Mineralogy and geochemistry, v. 80, no. 1, p. 61-164.

Asef, M. R., and Najibi, A. R., 2013, The effect of confining pressure on elastic wave velocities and dynamic to static Young's modulus ratio: Geophysics, v. 78, no. 3, p. D135-D142.

Ba, J., Cao, H., Yao, F., Nie, J., and Yang, H., 2008, Double-porosity rock model and squirt flow in the laboratory frequency band: Applied Geophysics, v. 5, no. 4, p. 261-276.

Baechle, G. T., Colpaert, A., Eberli, G. P., and Weger, R. J., 2008, Effects of microporosity on sonic velocity in carbonate rocks: The Leading Edge, v. 27, no. 8, p. 1012-1018.

Batzle, M. L., Han, D.-H., and Hofmann, R., 2006, Fluid mobility and frequency-dependent seismic velocity—Direct measurements: Geophysics, v. 71, no. 1, p. N1-N9.

Berg, C. F., Lopez, O., and Berland, H., 2017, Industrial applications of digital rock technology: Journal of Petroleum Science and Engineering, v. 157, p. 131-147.

Biot, M. A., 1956a, Theory of propagation of elastic waves in a fluid-saturated porous solid. I. Low frequency range: The Journal of the acoustical Society of america, v. 28, no. 2, p. 168-178.

-, 1956b, Theory of propagation of elastic waves in a fluid-saturated porous solid. II. Higher frequency range: The Journal of the acoustical Society of america, v. 28, no. 2, p. 179-191.

-, 1973, Nonlinear and semilinear rheology of porous solids: Journal of Geophysical Research, v. 78, no. 23, p. 4924-4937.

Blakey, R. C., 2013, Paleogeography and geologic evolution of North America. Colorado Plateau Geosystems, Inc.

Bode, I. Y., Zhang, C., Vanden Berg, B., and Grammer, G. M., 2019, Multiscale Imaging and Nuclear Magnetic Resonance Pore Characterization in Unconventional Carbonate Mudrocks of the Southern Midcontinent (USA): Mississippi Lime Play: SEPM (Society for Sedimentary Geology), v. 18, no. 2, p. 196-219.

Buggisch, W., Joachimski, M. M., Sevastopulo, G., and Morrow, J. R., 2008, Mississippian δ13Ccarb and conodont apatite δ18O records—their relation to the Late Palaeozoic Glaciation: Palaeogeography, Palaeoclimatology, Palaeoecology, v. 268, no. 3-4, p. 273-292.

Childress, M., and Grammer, G. M., 2015, High resolution sequence stratigraphic architecture of a Mid-Continent Mississippian outcrop in Southwest Missouri.

Chopra, S., Sharma, R. K., and Keay, J., 2018, SCOOP and STACK inversion case studies, SEG Technical Program Expanded Abstracts 2018, Society of Exploration Geophysicists, p. 3392-3396.

Darling, T., TenCate, J., Brown, D., Clausen, B., and Vogel, S., 2004, Neutron diffraction study of the contribution of grain contacts to nonlinear stress-strain behavior: Geophysical research letters, v. 31, no. 16.

Darot, M., and Reuschlé, T., 2000, Effect of pore and confining pressures on VP in thermally pre-cracked granites: Geophysical research letters, v. 27, no. 7, p. 1057-1060.

David, E., and Zimmerman, R. W., 2012, Pore structure model for elastic wave velocities in fluid-saturated sandstones: Journal of Geophysical Research: Solid Earth, v. 117, no. B7.

Davis, T., Healy, D., Bubeck, A., and Walker, R., 2017, Stress concentrations around voids in three dimensions: The roots of failure: Journal of Structural Geology, v. 102, p. 193-207.

de Oliveira, G. L. P., Ceia, M. A., Missagia, R. M., Archilha, N. L., Figueiredo, L., Santos, V. H., and Neto, I. L., 2016, Pore volume compressibilities of sandstones and carbonates from Helium porosimetry measurements: Journal of Petroleum Science and Engineering, v. 137, p. 185-201.

Dobrzanski, C. D., Maximov, M. A., and Gor, G. Y., 2018, Effect of pore geometry on the compressibility of a confined simple fluid: The Journal of chemical physics, v. 148, no. 5, p. 054503.

Dong, H., and Blunt, M. J., 2009, Pore-network extraction from micro-computerized-tomography images: Physical review E, v. 80, no. 3, p. 036307.

Dvorkin, J., and Derzhi, N., 2012, Rules of upscaling for rock physics transforms: Composites of randomly and independently drawn elements: Geophysics, v. 77, no. 3, p. WA129-WA139.

Dvorkin, J., Derzhi, N., Diaz, E., and Fang, Q., 2011, Relevance of computational rock physics: Geophysics, v. 76, no. 5, p. E141-E153.

Dvorkin, J., Mavko, G., and Nur, A., 1995, Squirt flow in fully saturated rocks: Geophysics, v. 60, no. 1, p. 97-107.

Dvorkin, J., Nolen-Hoeksema, R., and Nur, A., 1994, The squirt-flow mechanism: Macroscopic description: Geophysics, v. 59, no. 3, p. 428-438.

Eberhart-Phillips, D., Han, D.-H., and Zoback, M., 1989, Empirical relationships among seismic velocity, effective pressure, porosity, and clay content in sandstone: Geophysics, v. 54, no. 1, p. 82-89.

Fjær, E., 2019, Relations between static and dynamic moduli of sedimentary rocks: Geophysical Prospecting, v. 67, no. 1, p. 128-139.

Fjær, E., Stroisz, A. M., and Holt, R. M., 2013, Elastic dispersion derived from a combination of static and dynamic measurements: Rock Mechanics and Rock Engineering, v. 46, no. 3, p. 611-618.

Fredrich, J., Greaves, K., and Martin, J., Pore geometry and transport properties of Fontainebleau sandstone, *in* Proceedings International journal of rock mechanics and mining sciences & geomechanics abstracts1993, Volume 30, Elsevier, p. 691-697.

Freund, D., 1992, Ultrasonic compressional and shear velocities in dry clastic rocks as a function of porosity, clay content, and confining pressure: Geophysical Journal International, v. 108, no. 1, p. 125-135.

Geological Society of America, 1995, Rock Color Chart with Genuine Munsell Color Chips, v. 8, p. 8 charts.

Gor, G. Y., Siderius, D. W., Rasmussen, C. J., Krekelberg, W. P., Shen, V. K., and Bernstein, N., 2015, Relation between pore size and the compressibility of a confined fluid: The Journal of chemical physics, v. 143, no. 19, p. 194506.

Gutierrez, M. S., and Lewis, R. W., 2002, Coupling of fluid flow and deformation in underground formations: Journal of Engineering Mechanics, v. 128, no. 7, p. 779-787.

Gutschick, R. C., and Sandberg, C. A., 1983, Mississippian continental margins of the conterminous United States.

Han, T., Gurevich, B., Pervukhina, M., Clennell, M. B., and Zhang, J., 2016, Linking the pressure dependency of elastic and electrical properties of porous rocks by a dual porosity model: Geophysical Supplements to the Monthly Notices of the Royal Astronomical Society, v. 205, no. 1, p. 378-388.

Haq, B. U., and Schutter, S. R., 2008, A chronology of Paleozoic sea-level changes: Science, v. 322, no. 5898, p. 64-68.

Hart, D. J., and Wang, H. F., 1995, Laboratory measurements of a complete set of poroelastic moduli for Berea sandstone and Indiana limestone: Journal of Geophysical Research: Solid Earth, v. 100, no. B9, p. 17741-17751.

Karimpouli, S., and Tahmasebi, P., 2016, Conditional reconstruction: An alternative strategy in digital rock physics: Geophysics, v. 81, no. 4, p. D465-D477.

Kirstetter, O., and MacBeth, C., 2001, Compliance-based interpretation of dry frame pressure sensitivity in shallow marine sandstone, SEG Technical Program Expanded Abstracts 2001, Society of Exploration Geophysicists, p. 2132-2135.

Kitamura, K., Takahashi, M., Mizoguchi, K., Masuda, K., Ito, H., and Song, S.-R., 2010, Effects of pressure on pore characteristics and permeability of porous rocks as estimated from seismic wave velocities in cores from TCDP Hole-A: Geophysical Journal International, v. 182, no. 3, p. 1148-1160.

Lane, H. R., and De Keyser, T., Paleogeography of the late Early Mississippian (Tournaisian 3) in the central and southwestern United States1980, Rocky Mountain Section (SEPM).

LeBlanc, S. L., 2014, High resolution sequence stratigraphy and reservoir characterization of the" Mississippian Limestone" in north-central Oklahoma: Oklahoma State University.

Liu, E., Hudson, J. A., and Pointer, T., 2000, Equivalent medium representation of fractured rock: Journal of Geophysical Research: Solid Earth, v. 105, no. B2, p. 2981-3000.

Liu, H.-H., Rutqvist, J., and Berryman, J. G., 2009, On the relationship between stress and elastic strain for porous and fractured rock: International Journal of Rock Mechanics and Mining Sciences, v. 46, no. 2, p. 289-296.

MacEachern, J. A., Bann, K. L., Gingras, M. K., and Pemberton, S. G., 2009, Applied ichnology.

Martínez-Martínez, J., Benavente, D., and García-del-Cura, M., 2012, Comparison of the static and dynamic elastic modulus in carbonate rocks: Bulletin of engineering geology and the environment, v. 71, no. 2, p. 263-268.

Mashinsky, E., 2003, Differences between static and dynamic elastic moduli of rocks: Physical causes: Russian Geology and Geophysics, v. 44, no. 9, p. 953-959.

Mavko, G., Mukerji, T., and Dvorkin, J., 2020, The rock physics handbook, Cambridge university press.

Mazzullo, S. J., Wilhite, B. W., and Boardman II, D. R., 2011, Lithostratigraphic architecture of the Mississippian reeds spring formation (middle Osagean) in southwest Missouri,

northwest Arkansas, and northeast Oklahoma: Outcrop analog of subsurface petroleum reservoirs.

Miller, J. C., Pranter, M. J., and Cullen, A. B., 2019, Regional stratigraphy and organic richness of the Mississippian Meramec and associated strata, Anadarko Basin, central Oklahoma.

Morgenstern, N., and Phukan, A. T., Non-linear stress-strain relations for a homogeneous sandstone, *in* Proceedings International Journal of Rock Mechanics and Mining Sciences & Geomechanics Abstracts1969, Volume 6, Elsevier, p. 127-142.

Muqtadir, A., Al-Dughaimi, S., and Dvorkin, J., 2020, Deformation of granular aggregates: Static and dynamic bulk moduli: Journal of Geophysical Research: Solid Earth, v. 125, no. 1, p. e2019JB018604.

Northcutt, R. A., and Campbell, J. A., 1996, Geologic provinces of Oklahoma.

Nourifard, N., and Lebedev, M., 2019, Research note: the effect of strain amplitude produced by ultrasonic waves on its velocity: Geophysical Prospecting, v. 67, no. 4, p. 715-722.

Nur, A., and Simmons, G., 1969, The effect of saturation on velocity in low porosity rocks: Earth and Planetary Science Letters, v. 7, no. 2, p. 183-193.

O'Sullivan, C., O'Donovan, J., Ibraim, E., Hamlin, S., Muir Wood, D., and Marketos, G., 2016, Micromechanics of seismic wave propagation in granular materials.

Prasad, M., and Manghnani, M. H., 1997, Effects of pore and differential pressure on compressional wave velocity and quality factor in Berea and Michigan sandstones: Geophysics, v. 62, no. 4, p. 1163-1176.

Price, B., Haustveit, K., and Lamb, A., Influence of Stratigraphy on Barriers to Fracture Growth and Completion Optimization in the Meramec Stack Play, Anadarko Basin, Oklahoma, *in* Proceedings Unconventional Resources Technology Conference, Austin, Texas, 24-26 July 20172017, Society of Exploration Geophysicists, American Association of Petroleum …, p. 3453-3460.

Pride, S. R., and Berryman, J. G., 2003a, Linear dynamics of double-porosity dual-permeability materials. I. Governing equations and acoustic attenuation: Physical Review E, v. 68, no. 3, p. 036603.

-, 2003b, Linear dynamics of double-porosity dual-permeability materials. II. Fluid transport equations: Physical Review E, v. 68, no. 3, p. 036604.

Pyrak-Nolte, L., and Morris, J., 2000, Single fractures under normal stress: The relation between fracture specific stiffness and fluid flow: International Journal of Rock Mechanics and Mining Sciences, v. 37, no. 1-2, p. 245-262.

Pyrak-Nolte, L., Myer, L., and Cook, N., 1990, Transmission of seismic waves across single natural fractures: Journa l of Geophysical Research.

Raj, R., Jaiswal, P., Vanden Berg, B., and Grammer, G. M., 2019, Pore Size and Ultrasonic Velocity: Lessons from Miss Lime Reservoirs: SEPM (Society for Sedimentary Geology), v. 18, no. 2, p. 183-195.

Robin, P. Y. F., 1973, Note on effective pressure: Journal of Geophysical Research, v. 78, no. 14, p. 2434-2437.

Vanden Berg, B., and Grammer, G. M., 2016, 2-D Pore Architecture Characterization of a Carbonate Mudrock Reservoir: Insights from the Mid-Continent “Mississippi Lime”.

Vanden Berg, B., Nussbaumer, C., Noack, A., Thornton, J., Weger, R. J., Eberli, G. P., and Grammer, G. M., 2018, A comparison of the relationship between measured acoustic response and porosity in carbonates across different geologic periods, depositional basins, and with variable mineral composition: Interpretation, v. 6, no. 2, p. T245-T256.

Vanorio, T., 2015, Recent advances in time-lapse, laboratory rock physics for the characterization and monitoring of fluid-rock interactions: Geophysics, v. 80, no. 2, p. WA49-WA59.

Vanorio, T., Nur, A., and Ebert, Y., 2011, Rock physics analysis and time-lapse rock imaging of geochemical effects due to the injection of CO 2 into reservoir rocks: Geophysics, v. 76, no. 5, p. O23-O33.

Wang, Z., Wang, R., Wang, F., Qiu, H., and Li, T., 2015, Experiment study of pore structure effects on velocities in synthetic carbonate rocks: Geophysics.

Watney, W. L., Guy, W. J., and Byrnes, A. P., 2001, Characterization of the Mississippian chat in south-central Kansas: AAPG bulletin, v. 85, no. 1, p. 85-113.

Weger, R. J., Eberli, G. P., Baechle, G. T., Massaferro, J. L., and Sun, Y.-F., 2009, Quantification of pore structure and its effect on sonic velocity and permeability in carbonates: AAPG bulletin, v. 93, no. 10, p. 1297-1317.

Weibo, S., Zihan, Q., Yanan, H., and CHENG, H., 2020, Estimating pore volume compressibility by spheroidal pore modeling of digital rocks: Petroleum Exploration and Development, v. 47, no. 3, p. 603-612.

Zhang, L., Ba, J., Fu, L., Carcione, J. M., and Cao, C., 2019, Estimation of pore microstructure by using the static and dynamic moduli: International Journal of Rock Mechanics and Mining Sciences, v. 113, p. 24-30.

Zhao, Y., and Liu, H.-H., 2012, An elastic stress–strain relationship for porous rock under anisotropic stress conditions: Rock mechanics and rock engineering, v. 45, no. 3, p. 389-399.

Zimmerman, R. W., Somerton, W. H., and King, M. S., 1986, Compressibility of porous rocks: Journal of Geophysical Research: Solid Earth, v. 91, no. B12, p. 12765-12777.

CHAPTER IV

CLAY DIAGENESIS IN MERAMEC FORMATION, OKLAHOMA: INSIGHTS FROM ROCK PHYSICS MODELING

4.1 Abstract

We show how clay diagenesis influences the mechanistic behavior of a rock different under saturated and dry conditions. We found that saturated and dry elastic velocities of samples from the Meramec formation, Oklahoma, could be related to their known porosity and composition through a common rock physics model only if clay and quartz were considered structural in dry and partly disseminated in saturated conditions. In-situ smectite-to-illite transformation can explain the observations in that it creates products at pore linings that remain loosely connected with the matrix behaving like a suspension in saturated condition but coalesce with the matrix as the system dehydrates during the desiccation process. The novelty of this study is using rock physics to understand a process rather than the end product.

4.2 Introduction

Rock physics relates intrinsic rock properties and environmental inputs to bulk elastic properties and vice-versa using physics-driven mathematical models reducing the non-uniqueness inherent in interpretation. Rock physics models have been used to understand the mechanistic behavior of a wide variety of formations ranging from high-porosity high-permeability sand

dominated (Avseth et al. (2010)) to low-porosity low-permeability fine-grained “tight” reservoirs (Dvorkin et al. (2021); Vernik and Milovac (2011)). It has also been used to the understand the fabric (Avseth et al. (2000); Winters et al. (2004)), morphology of pore suspensions (Jaiswal et al. (2014); Winters et al. (2004)) and the architecture of the pores themselves (Guo et al. (2021); Xu and Payne (2009)). Their application ranges across kilometer-scale field seismic (Avseth and Lehocki (2021); Grana and Dvorkin (2011)) to meter-scale well logs (Dvorkin et al. (2021); Mur and Vernik (2019)) to centimeter scale core plugs (Dvorkin et al. (2003); Liu and Fu (2020)). Mostly rock physics describes the end-products of a geological process. Here, we have used it to understand the process of the clay diagenesis in the Meramec formation, Oklahoma.

The Mississippian-age Meramec formation represents a distal depositional environment with sedimentary influx from both terrigenous and marine sources. It is generally recognized as a mixed carbonate-siliciclastic system with variable amounts of clay and rapidly changing facies architecture (Almasoodi et al. (2020); Price et al. (2017)). The Mississippian-age formations in the US midcontinent including the proximal equivalent of Meramec, the “Miss Lime” formation, constitute a set of tight unconventional reservoirs that are produced through hydraulic stimulation and fracturing (Almasoodi et al. (2020); Raj et al. (2019); Vanden Berg and Grammer (2016)). They are underlain by the Devonian-age Woodford Shale which serves as the source rock and overlain by Pennsylvanian-age shale units that serve as the seal. As opposed to Miss Lime, Meramec has low water-cut but an unpredictable well-to-well production decline.

Data used in this study are from a borehole in Canadian county, Oklahoma, and were acquired in both saturated (reservoir fluids) and dry (air) states. The core of the problem was to explore the rock-physics space and find what model would best relate the porosity and composition to elastic velocities under both saturated and dry conditions. Saturated data was acquired in the borehole through logging. Dry data were acquired on core plugs. In the end we found that the constant-cement model (Dvorkin et al. (2021)) in both conditions followed by Gassmann (1951)

fluid substitution best explained our datasets when clay and quartz were assumed to be fully structural in dry and partly disseminated in saturated conditions. This can be explained through in-situ smectite-to-illite transition, expected during burial of Meramec, can create products that will remain in suspension in reservoir conditions but coalesce with the matrix during the process of desiccation of the core plugs. The next sections describe our model building, application and results.

4.3 Dataset

Thirty-five core plugs, ~2″ in length and 1.5″ in diameter, were extracted from a continuous split-core. The core plugs were first desiccated and then used for measuring He-gas porosity (ϕ_{He}) using gas-injection porosimetry as well as elastic velocities over loading (pressurized) and unloading (depressurized) cycle. A portion of the same core plugs were also used to identify the key minerals through X-ray diffraction (XRD). The wellbore that provided the core was logged using both the triple combo and sonic sondés thus providing the standard log suite. In this paper, we have only used neutron porosity (ϕ_{NPHI}), density porosity (ϕ_{DPHI}), compressional (ΔT_C) and shear sonic slowness (ΔT_S) logs.

4.3.1 Porosity

Porosity is the ratio of the pore (or void) volume to the bulk volume of a rock. It is calculated by determining any two parameters: pore volume (v_P), grain volume (v_G) and bulk volume (v_B). We used AccuPyc II 1340 pycnometer to measure grain volume that uses helium gas injection technique. AccuPyc II 1340 pycnometer measures the grain volume by using pressure drop between the sample chamber and a precision chamber. Bulk volume was calculated by taking average of repeated core plug's diameter and length measured using a digital caliper. The He-gas porosity (ϕ_{He}) measurement was done prior to any destructive laboratory measurement (e.g. ultrasonic velocity) to obtain reliable porosity data.

$$\nu_P = \nu_B - \nu_G; \phi_{He} = 100\frac{\nu_P}{\nu_B} \quad (4.1)$$

4.3.2 Velocity

One P- and two orthogonal S-waves transit times, all under dry conditions and 1 MHz central frequency, were recorded using New England Autolab 1000. Sample preparation was done by first putting individual core plugs in a rubber jacket that was set between a transducer-receiver assembly. This assembly was inserted in a mineral oil filled pressure chamber and locked. The chamber was slowly loaded in steps of 5, 10, 15, 20, 30 and 40 MPa and then unloaded by retracing the same pressure steps. Transit times were recorded at all pressure steps in both loading and unloading cycles. First arrivals were manually picked in all the waveforms and were converted to velocity using sample dimension and instrument constants. Based on depth and hydrostatic gradient, the reservoir pressure was calculated as 30 MPa. Loading cycle closes cracks that develop due to core exhumation so the 30 MPa unloading cycle velocities were selected to represent reservoir velocities. Due to incomplete saturation problems, measurements under saturation condition were not performed.

4.3.3 Composition

Approximately 0.5 cm portion from one of the ends of the core plug samples was cut, powdered in a SPEX ball mill then in mortar-and-pestle and analyzed in Rigaku MiniFlex Diffraction machine. Before analysis, the machine was calibrated with a quartz sample. Powder Diffraction File was used to match and identify minerals. Rietveld refinement scheme was used to quantify the identified minerals in RIQAS software. Figure 4.1 summarizes the composition in the form of stacked bar plot.

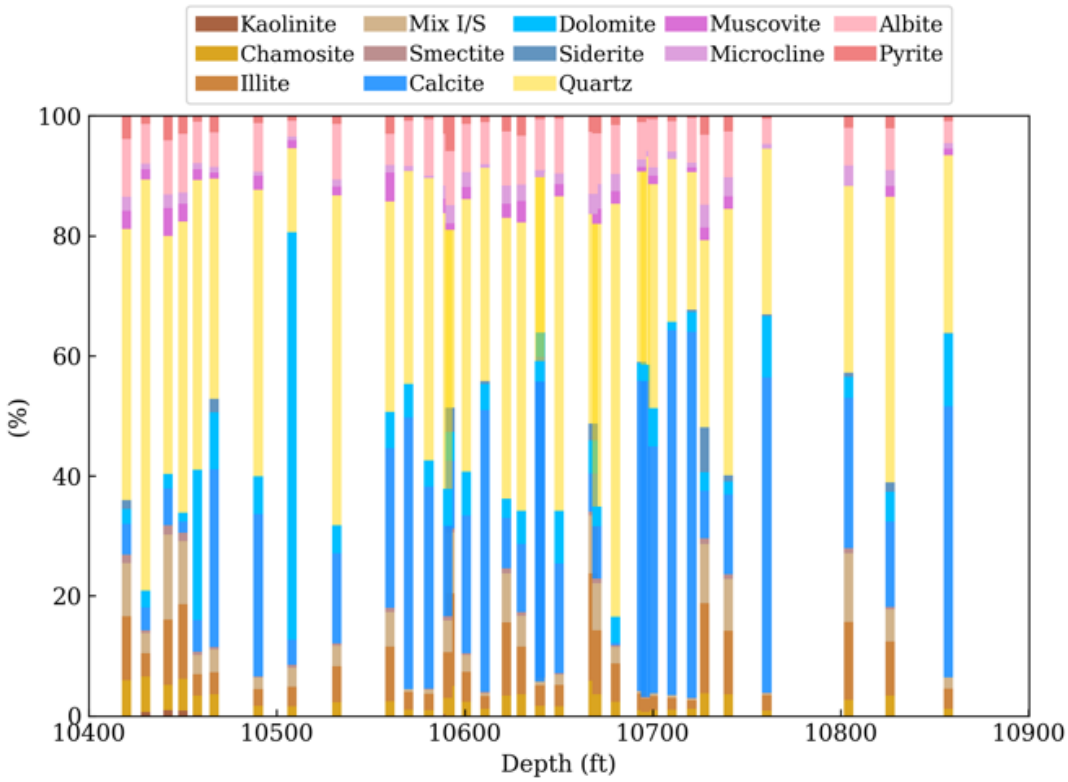

Figure 4.1 Composition. Mineralogical composition from core plug samples are shown as stacked bar plot.

4.3.4 Well Log

A comprehensive set of industry standard well suite was provided by Devon Energy Corporation, Oklahoma City, USA. Amongst them, only ϕ_{NPHI}, ϕ_{DPHI}, ΔT_C and ΔT_S were relevant and used in this work (Figure 4.2). Well log depth was corrected using a correction chart that matched the log depth to the core depth. Logs were resampled to core plug depths and provided in-situ saturated reservoir conditions which were not available from the laboratory measurements performed on the core plug samples.

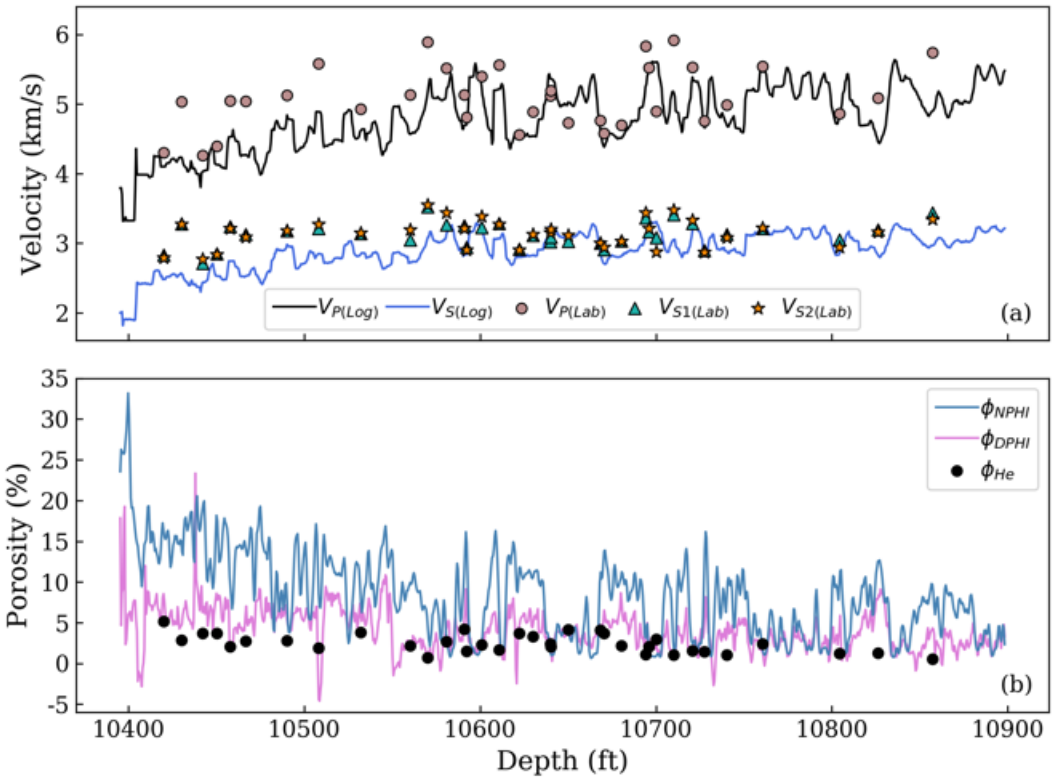

Figure 4.2 Dataset. Figure shows **(A)** V_P and V_S from well log and dry ultrasonic measurements, and **(B)** ϕ_{NPHI} and ϕ_{DPHI} from well logs and ϕ_{He} from gas-porosimetry.

4.4 Rock Physics Model Building

Hill (1952) average was used to calculate the zero-porosity "solid" end-member bulk and shear moduli of the rock, K_S and G_S, using the mineralogical properties in Table 4.1.

$$K_{Voigt} = \sum_{i=1}^{M} x_i K_i \; ; \; G_{Voigt} = \sum_{i=1}^{M} x_i G_i \tag{4.2}$$

$$\frac{1}{K_{Reuss}} = \sum_{i=1}^{M} \frac{x_i}{K_i} \; ; \; \frac{1}{G_{Reuss}} = \sum_{i=1}^{M} \frac{x_i}{G_i} \tag{4.3}$$

$$K_S = \frac{K_{Voigt} + K_{Reuss}}{2} \; ; \; G_S = \frac{G_{Voigt} + G_{Reuss}}{2} \tag{4.4}$$

where, $\sum_{i=1}^{M} x_i = 1$,

x_i is fractional volume of i^{th} mineral component, and

K_i and G_i are the bulk and shear modulus of i^{th} mineral component, respectively.

Table 4.1: Rock Properties

Components	Bulk Modulus (in GPa)	Shear Modulus (in GPa)	Density (in g/cc)
Quartz	37	44	2.65
Muscovite	58	35	2.84
Microcline	55	28	2.56
Albite	57	29	2.61
Pyrite	147	132	4.93
Calcite	77	32	2.71
Dolomite	95	45	2.87
Siderite	124	51	3.96
Kaolinite	21	7	2.58
Chamosite	21	7	2.58
Smectite	21	7	2.58
Illite	21	7	2.58
Mix Illite/Smectite	21	7	2.58
Air	0.000131	0	0.00119
Brine	3.05	0	1.06
Hydrocarbon Oil	0.60	0	0.66
Hydrocarbon Gas	0.08	0	0.26

The zero-porosity end-member density (ρ_S) was computed as the weighted mean of mineral densities.

$$\rho_S = \sum_{i=1}^{M} x_i \, \rho_i \tag{4.5}$$

For computing the critical-porosity "Hertz-Mindlin" end-member bulk and shear moduli, K_{HM} and G_{HM} respectively, we used Dvorkin et al. (2021) formulations as follows:

$$K_{HM} = \left[\frac{C^2(1-\phi_C)^2 G_S^2}{18\pi^2(1-\nu_S)^2} P\right]^{\frac{1}{3}} \tag{4.6}$$

$$G_{HM} = \frac{2+\frac{3}{f}-\nu_S\left(1+\frac{3}{f}\right)}{5(2-\nu_S)} \left[\frac{3C^2(1-\phi_C)^2 {G_S}^2}{2\pi^2(1-\nu_S)^2} P\right]^{\frac{1}{3}} \tag{4.7}$$

where, C is the coordination number,

ϕ_C is the critical porosity (in fraction),

G_S is the shear modulus of the solid grain,

v_S is the Poisson's ratio of the solid grain,

P is pressure, and

f is the shear stiffness reduction factor.

Free parameters C and f aid data fitting more than describing the physical state of the rock (Dvorkin et al. (2021)).

The drained elastic moduli is calculated using the modified lower Hashin-Shtrikman bound (Mavko et al. (2020)).

$$K_{Dry} = \left[\frac{\frac{\phi}{\phi_C}}{K_{HM}+\frac{4}{3}G_{HM}} + \frac{1-\frac{\phi}{\phi_C}}{K+\frac{4}{3}G_{HM}}\right]^{-1} - \frac{4}{3}G_{HM} \tag{4.8}$$

$$G_{Dry} = \left[\frac{\frac{\phi}{\phi_C}}{G_{HM}+z_{HM}} + \frac{1-\frac{\phi}{\phi_C}}{G+z_{HM}}\right]^{-1} - z_{HM} \tag{4.9}$$

where, $z_{HM} = \frac{G_{HM}}{6}\left(\frac{9K_{HM}+8G_{HM}}{K_{HM}+2G_{HM}}\right)$, and

ϕ is porosity (in fraction).

We calculated the fluid bulk modulus and density, K_f^i and ρ_f^i respectively, at reservoir pressure and temperature after Batzle and Wang (1992) and averaged values as follows:

$$\frac{1}{K_f} = \sum_{i=1}^{L}\frac{S_i}{K_f^i}\ ;\ \rho_f = \sum_{i=1}^{L} S_i\,\rho_f^i \tag{4.10}$$

where, $\sum_{i=1}^{L} S_i = 1$.

The reader may note that individual saturations of oil, gas and water were available from routine core analysis.

The undrained moduli, K_{SAT} and G_{SAT} respectively, were computed as follows (Gassmann (1951)):

$$K_{SAT} = K_S \frac{\phi K_{Dry} - (1+\phi) K_f K_{Dry}/K_S + K_f}{(1-\phi) K_f + \phi K_S - K_f K_{Dry}/K_S}; \; G_{SAT} = G_{Dry} \tag{4.11}$$

The bulk density (ρ_{eff}) was computed as:

$$\rho_{eff} = (1-\phi)\rho_S + \phi\rho_f \tag{4.12}$$

Finally, V_P and V_S were computed as:

$$V_P = \sqrt{\frac{K_{SAT} + \frac{4}{3} G_{SAT}}{\rho_{eff}}}; \; V_S = \sqrt{\frac{G_{SAT}}{\rho_{eff}}} \tag{4.13}$$

Equations 4.2 – 4.13 were solved using porosity, mineralogical composition, and parameter values in Table 4.1 and 4.2.

Table 4.2: Rock physics modeling parameters

Condition	P	ϕ_C	C	f	Clay	Quartz	
						Depth (<10550′)	Depth (>10550′)
Dry	30	0.36	24	0.6	a=0 b=0	a=0 b=0	a=0 b=0
Saturated	30	0.36	24	0.6	a=0.10 b=0.02	a=0.25 b=0.05	a=0.10 b=0.03

4.5 Results

Results are shown in Figure 4.3 and 4.4. In Figure 4.3, dashed lines are log V_P and V_S and solid lines are their counterparts predicted by the constant-cement model assuming the reservoir fluids in pore spaces.

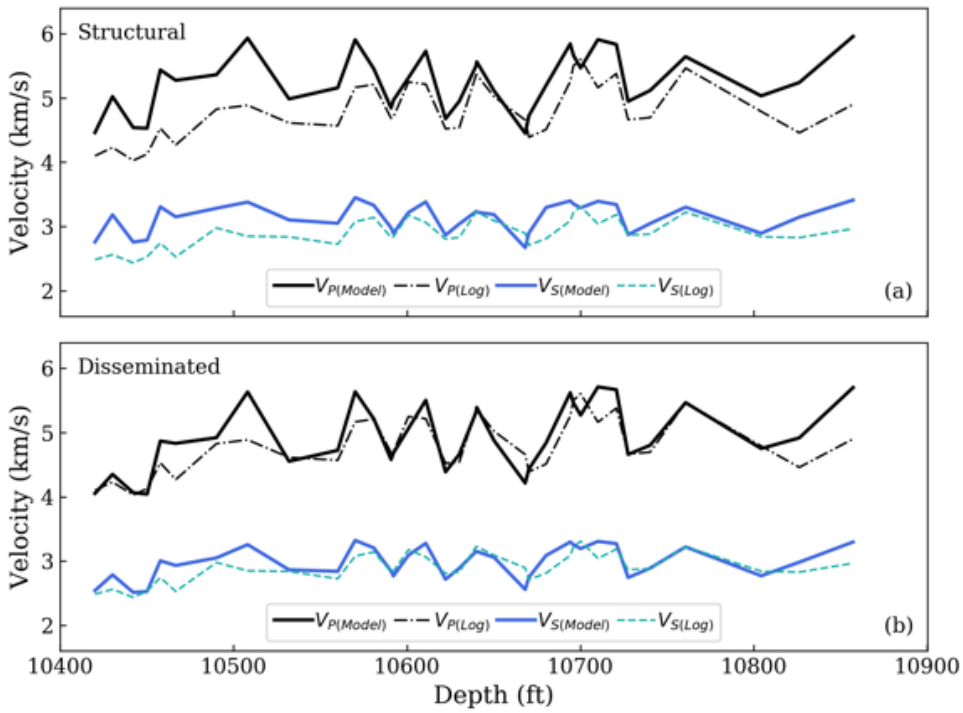

Figure 4.3 Saturated Condition. Figure shows rock physics modeling results for log V_P and V_S when **(A)** clay is completely structural, and **(B)** clay (smectite, mixed illite-smectite (I/S) and illite) and quartz, are partly disseminated.

In Figure 4.4, dashed lines are laboratoy measured dry-rock V_P and V_S and solid lines are their counterparts predicted by the constant-cement model assuming air in pore spaces.

Figure 4.3A and 4.4A show model predictions when clay is completely structural. Figure 4.3B and 4.4B show model predictions when clay (smectite, mixed illite-smectite (I/S), and illite) and quartz, were partly disseminated.

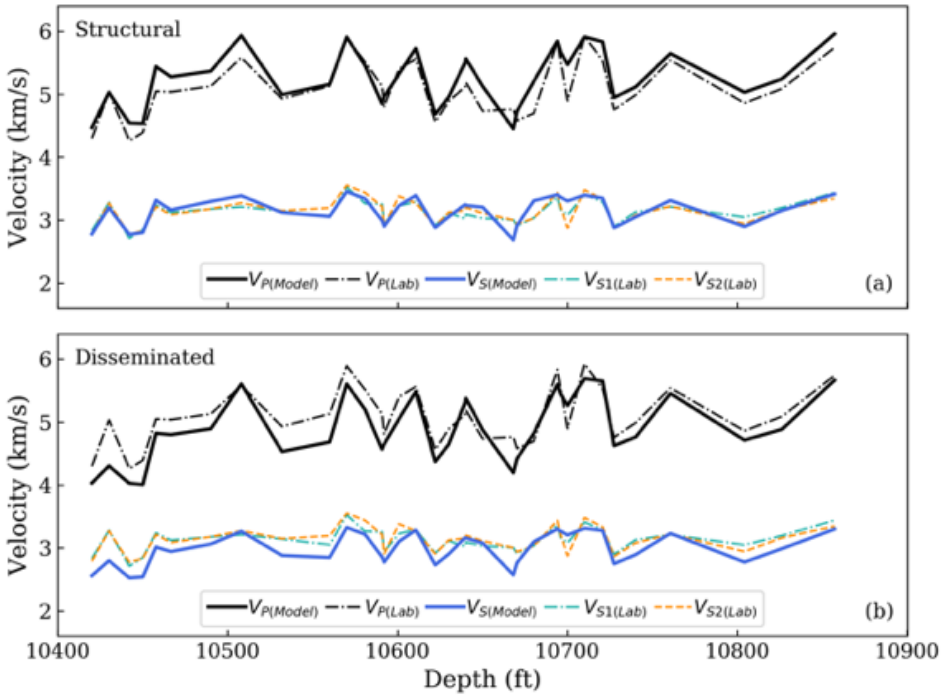

Figure 4.4 Dry Condition. Figure shows rock physics modeling results for dry V_P and V_S when **(A)** clay is completely structural, and **(B)** clay (smectite, mixed illite-smectite (I/S) and illite) and quartz, are partly disseminated.

The disseminated fraction, x_d, was computed as:

$$x_d = a_d(\phi_{NPHI} - \phi_{DPHI}) + b_d \tag{4.14}$$

where, d : clay (smectite, mixed I/S, illite) or quartz.

A comparison of the data fit in Figure 4.3 suggests that at least for a few samples, data fit improves significantly by partly disseminating clay and quartz (Figure 4.3B). The same idea does not hold for the dry case (pores are air filled) as shown in Figure 4.4B where data fit improves when clay and quartz are structural (or at least less dessiminated than saturated) (Figure 4.4A).

4.6 Discussion

A comparison between Figures 4.3 and 4.4 suggested that the effect of clay and quartz dissemination on elastic velocities is more pronounced at reservoir conditions as opposed to dry conditions. This is as expected. During its burial, the Meramec formation was subjected to

temperatures of 80-100°C, within which smectite becomes unstable and starts transforming to illite via mixed I/S mineralogy (Nadeau et al. (1985), Nadeau et al. (2002)). This is also reflected in our clay composition. For example, in all samples the volumetric fraction of illite is consistently higher than mixed I/S which is in turn higher than smectite. In some samples, smectite was completely absent but mixed I/S and illite were present. Thus, it is likely that illite and mixed I/S have grown at the expense of smectite.

Smectite particles have an expanding nature where the tetrahedral and octahedral sheets are separated by fluid-filled interlayer space. The elastic stress transfer is naturally disrupted by the interlayer cavity and therefore although smectite may remain attached to the matrix, a fraction of the grain appears to be in suspension to the propagating waves. Further, because the alteration happens within the sheets, the altered products also appear to be in suspension (Figure 4.5A). Naturally, during dessication when the interlayer water is reduced, the original smectite particle along with the altered products tend to coalesce with pore wall and start to contribute to the stress transfer (Figure 4.5B). As a result, in the dry case, they are considered to be structural.

Free quartz, which is a byproduct, of smectite alteration, also behaves as a pore-filling constituent at reservoir condition but probably clogs the pore throats during desiccation. Quartz disseminaton seems to be more pronounced at depth shallower than 10,550 ft, where the dry V_P is considerably higher than the log V_P. This could be due to paleoclimatic conditions in that the availability of limiting reagents change the amout of silica released during the transformation (Freed and Peacor (1989)). Unless both the log and dry velocities were modeled simultaneouly, these subtle behavior of rocks with diagenatic clays, which may have implications on production, would have remained undiscovered.

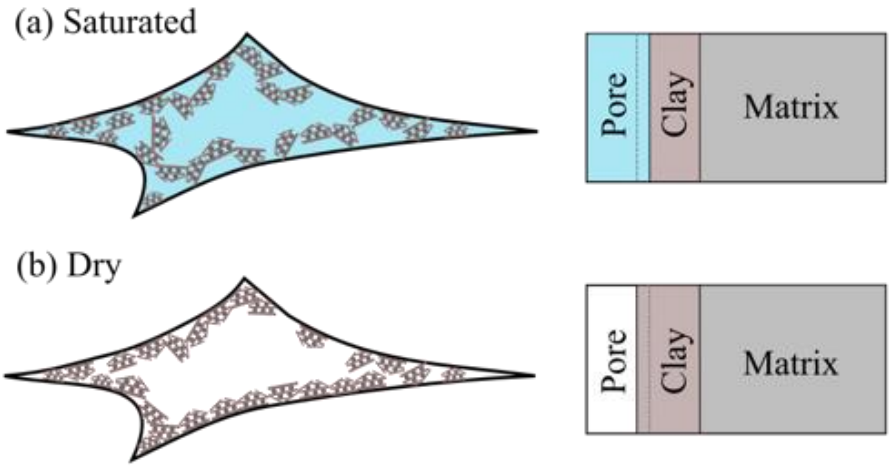

Figure 4.5 Conceptual model. Schematic shows clay morphology in **(A)** saturated and **(B)** dry condition.

4.7 Conclusion

The constant-cement model was able to simultaneously relate the saturated (pores are reservoir fluid filled) and dry (pores are air filled) elastic velocities of the Mississippian-age Meramec formation to the observed composition and porosities at a wellbore in Canadian County, Oklahoma. Model required clay and quartz to remain structural in the dry case and partly disseminated in the saturated case. Given the burial history of the rock, smectite-to-illite transition can explain the observations. The potential to use rock physics to infer diagenesis, such as in this case study, can greatly aid reservoir characterization of unconventional systems.

4.8 References

Almasoodi, M., Vaidya, R., and Reza, Z., 2020, Drawdown-Management and Fracture-Spacing Optimization in the Meramec Formation: Numerical-and Economics-Based Approach: SPE Reservoir Evaluation & Engineering.

Avseth, P., Dvorkin, J., Mavko, G., and Rykkje, J., 2000, Rock physics diagnostic of North Sea sands: Link between microstructure and seismic properties: Geophysical Research Letters, v. 27, no. 17, p. 2761-2764.

Avseth, P., and Lehocki, I., 2021, 3D Subsurface Modeling of Multi-Scenario Rock Property and AVO Feasibility Cubes—An Integrated Workflow: Frontiers in Earth Science, v. 9, p. 160.

Avseth, P., Mukerji, T., Mavko, G., and Dvorkin, J., 2010, Rock-physics diagnostics of depositional texture, diagenetic alterations, and reservoir heterogeneity in high-porosity siliciclastic sediments and rocks—A review of selected models and suggested work flows: Geophysics, v. 75, no. 5, p. 75A31-75A47.

Batzle, M., and Wang, Z., 1992, Seismic properties of pore fluids: Geophysics, v. 57, no. 11, p. 1396-1408.

Dvorkin, J., Walls, J., and Davalos, G., 2021, Velocity-Porosity-Mineralogy Model for Unconventional Shale and Its Applications to Digital Rock Physics: Frontiers in Earth Science, v. 8, p. 654.

Dvorkin, J., Walls, J., Tutuncu, A., Prasad, M., Nur, A., and Mese, A., 2003, Rock property determination using digital rock physics, SEG Technical Program Expanded Abstracts 2003, Society of Exploration Geophysicists, p. 1660-1663.

Freed, R. L., and Peacor, D. R., 1989, Geopressured shale and sealing effect of smectite to illite transition: AAPG bulletin, v. 73, no. 10, p. 1223-1232.

Gassmann, F., 1951, Uber die elastizitat poroser medien: Vierteljahrsschrift der Naturforschenden Gesellschaft in Zurich, v. 96, p. 1-23.

Grana, D., and Dvorkin, J., 2011, The link between seismic inversion, rock physics, and geostatistical simulations in seismic reservoir characterization studies: The Leading Edge, v. 30, no. 1, p. 54-61.

Guo, Z., Qin, X., Zhang, Y., Niu, C., Wang, D., and Ling, Y., 2021, Numerical investigation of the effect of heterogeneous pore structures on elastic properties of tight gas sandstones: Frontiers in Earth Science, v. 9, p. 219.

Hill, R., 1952, The elastic behaviour of a crystalline aggregate: Proceedings of the Physical Society. Section A, v. 65, no. 5, p. 349.

Jaiswal, P., Al-Hadrami, F., Atekwana, E. A., and Atekwana, E. A., 2014, Mechanistic models of biofilm growth in porous media: Journal of Geophysical Research: Biogeosciences, v. 119, no. 7, p. 1418-1431.

Liu, N., and Fu, L.-Y., 2020, Elastic characteristics of digital cores from Longmaxi shale using lattice spring models: Communications in Computational Physics, v. 28, no. 1, p. 518-538.

Mavko, G., Mukerji, T., and Dvorkin, J., 2020, The rock physics handbook, Cambridge university press.

Mur, A., and Vernik, L., 2019, Testing popular rock-physics models: The Leading Edge, v. 38, no. 5, p. 350-357.

Nadeau, P., Wilson, M., McHardy, W., and Tait, J., 1985, The conversion of smectite to illite during diagenesis: evidence from some illitic clays from bentonites and sandstones: Mineralogical Magazine, v. 49, no. 352, p. 393-400.

Nadeau, P. H., Peacor, D. R., Yan, J., and Hillier, S., 2002, IS precipitation in pore space as the cause of geopressuring in Mesozoic mudstones, Egersund Basin, Norwegian continental shelf: American Mineralogist, v. 87, no. 11-12, p. 1580-1589.

Price, B., Haustveit, K., and Lamb, A., Influence of Stratigraphy on Barriers to Fracture Growth and Completion Optimization in the Meramec Stack Play, Anadarko Basin, Oklahoma, *in* Proceedings Unconventional Resources Technology Conference, Austin, Texas, 24-26 July 20172017, Society of Exploration Geophysicists, American Association of Petroleum …, p. 3453-3460.

Raj, R., Jaiswal, P., Vanden Berg, B., and Grammer, G. M., 2019, Pore Size and Ultrasonic Velocity: Lessons from Miss Lime Reservoirs, *in* McNeill, D. F., Harris, P., Rankey, E. C., and Hsieh, J. C. C., eds., Carbonate Pore Systems: New Developments and Case Studies, Volume 112, SEPM Society for Sedimentary Geology, p. 183-195.

Vanden Berg, B., and Grammer, G. M., 2016, 2-D Pore Architecture Characterization of a Carbonate Mudrock Reservoir: Insights from the Mid-Continent "Mississippi Lime", *in* T. Olson, ed., Imaging Unconventional Reservoir Pore Systems, Volume 112, American Association of Petroleum Geologists, p. 185-231.

Vernik, L., and Milovac, J., 2011, Rock physics of organic shales: The Leading Edge, v. 30, no. 3, p. 318-323.

Winters, W. J., Pecher, I. A., Waite, W. F., and Mason, D. H., 2004, Physical properties and rock physics models of sediment containing natural and laboratory-formed methane gas hydrate: American Mineralogist, v. 89, no. 8-9, p. 1221-1227.

Xu, S., and Payne, M. A., 2009, Modeling elastic properties in carbonate rocks: The Leading Edge, v. 28, no. 1, p. 66-74.

CHAPTER V

CONCLUSION AND FUTURE SCOPE

5.1 Summary

This dissertation focuses on understanding the effect that nanopore (10^{-9}-10^{-6} m) shape and size distributions have on (1) dry-frame V_P and (2) sensitivity of dry-frame V_P to confining pressure. A dual goal is to understand and build a predictive model for the effect that clay diagenesis (smectite-to-illite transformation) has on the elastic velocities (V_P and V_S) under saturated and dry conditions.

The following summarizes the major findings and contributions of this dissertation:

(1) Simultaneous visualization of directly acquired pore architectural parameters (such as area [A_r], perimeter [P_e], length [l], and width[w]) provide more information about pore population distribution than their derivatives (such as roundness, or dominant pore-size based on population percentile). In this work, a pore-shape distribution plot, which is a contoured 2D histogram crossplot between $\log_{10}A_r/\log_{10}P_e$ and $\log_{10}(l/w)$, identified samples with cracks, complex pore shapes, and helped in grouping samples based on similarity in pore shape. Similarly, pore-size distribution, which is a contoured 2D histogram crossplot between $\log_{10}A_r$ and $\log_{10}P_e$, provided a comprehensible overview of the spread of different pore sizes.

(2) Dry-frame V_P in the Mississippian-age Miss Lime formation could be dependent on pore-size distribution. Chapter III highlighted that drivers of V_P could be pore-size, in addition to composition or bulk ϕ. In samples belonging to the same facies and the quartz-based composition subgroups, V_P increased with a decrease in the dominant pore size below 1 µm. Nanopore scale (10^{-9}-10^{-6} m) and seismic strain amplitude (10^{-7}-10^{-6}) are of comparable order, and a higher nanopore population offers more opportunity to propagating seismic waves to induce deformation in the porous rock media.

(3) Dry-frame V_P pressure sensitivity in the Mississippian-age Meramec formation could be dependent on pore-shape and pore-size distribution. Chapter IV highlighted that the pore-shape distribution crossplots identified samples with excessive complex pores and fractures and samples with a similar spread of the pore-shapes within the individual facies. In fracture and complex-pore free samples belonging to the same facies and the pore-shape distribution subgroups, V_P rapidly increased with the confining pressure when the pore size decreased in the nanopore range. Likelihood of pores becoming isolated at nanopore scale, and increase in the bulk modulus of fluid trapped within the nanopores could have, in turn, increased V_P pressure-sensitivity.

(4) A common rock physics model-based approach was used in Chapter V that simultaneously explains all the elastic velocities related to porosity and mineralogy from the same site under saturated and dry conditions. Clay and quartz fraction modeled as completely structural in the rock framework explained the dry condition elastic velocities, and when modeled as partly disseminated in the pore space explained the saturated condition elastic velocities. Model inferred a geologic process - smectite-to-illite transformation, which might be creating products that are causative influences on the elastic velocities.

5.2 Future Work Scope

The following could be potential opportunities to explore research based on the work presented in this dissertation.

5.2.1 Dual-fluid model

At the nanopore scale, the thermodynamic behavior of trapped fluids differs from those in the bulk (Gor et al. (2015); Dobrzanski et al. (2018)). In particular, it has been observed that the bulk modulus of the fluid trapped in the nanopore increases with a decrease in pore size. A physics-driven mathematical model for rocks populated with nanopores could be developed where fluid would be modeled in two ways – compressible and incompressible. The bulk modulus of the compressible part would be attributed to non-compliant and isolated nanopores, and proportional to confining pressure while the bulk modulus of the incompressible part in interconnected pores would be unchanged.

5.2.2 Nanopore effects on dry-frame V_P temperature sensitivity

The work presented in Chapter III considers the effects of nanopores on dry-frame V_P pressure sensitivity only. Temperature variations have been shown to dominantly change fluid properties more than intergranular pore and microcrack density in carbonate rock (Qi et al. (2021)). A research question for the future would be how nanopore would influence dry-frame V_P and V_S temperature sensitivity and to what extent would be temperature-dependent V_P and V_S dispersion.

5.3 References

Dobrzanski, C. D., Maximov, M. A., and Gor, G. Y., 2018, Effect of pore geometry on the compressibility of a confined simple fluid: The Journal of chemical physics, v. 148, no. 5, p. 054503.

Gor, G. Y., Siderius, D. W., Rasmussen, C. J., Krekelberg, W. P., Shen, V. K., and Bernstein, N., 2015, Relation between pore size and the compressibility of a confined fluid: The Journal of chemical physics, v. 143, no. 19, p. 194506.

Qi, H., Ba, J., & Müller, T. M. (2021). Temperature effect on the velocity-porosity relationship in rocks. Journal of Geophysical Research: Solid Earth, 126, e2019JB019317.

APPENDIX A

Raymer et al. (1980) model

The Raymer-Hunt-Gardner (RHG) model (Raymer et al. 1980) was introduced to correct for the observed anomalies and shortcomings of the Wyllie time-average formula. In the RHG model, V_P is computed using elastic moduli of mineral fractions, porosity, and type of pore filling material at each sample. There are two velocity components in the RHG V_P equation: (1) composition velocity and (2) pore filling material velocity. For composition velocity, the elastic modulus (K and μ) of each mineral fraction is averaged following Hill's average (average of Voigt and Reuss bounds on mineral fractions):

$$M_{Voigt} = \sum_{i=1}^{n} f_i M_i \tag{A.1}$$

$$\frac{1}{M_{Reuss}} = \sum_{i=1}^{n} \frac{f_i}{M_i} \tag{A.2}$$

$$M_{Hill} = \frac{M_{Voigt} + M_{Reuss}}{2} \tag{A.3}$$

where, f_i is mineral fraction, M_i is elastic moduli (either K or μ), and n is the number of different minerals present in the rock. The mineral density (ρ_0) is computed by summing the weighted density of each mineral constituent (ρ_i), thus:

$$\rho_0 = \sum_{i=1}^{n} f_i \rho_i \tag{A.4}$$

Composition velocity (V_0) part is computed using the following relation:

$$V_0 = \sqrt{\frac{K_{Hill} + \frac{4}{3}\mu_{Hill}}{\rho_0}} \tag{A.5}$$

Since the measured values are of dry P-wave velocity, the pore fluid is chosen as air, and its velocity is computed at atmospheric conditions, which gives the pore filling material velocity (V_{fl}):

$$V_{fl} = \sqrt{\frac{K_{fl}}{\rho_{fl}}} \tag{A.6}$$

Now the following RHG equation is used to compute V_P:

$$V_{P(RHG)} = (1 - \phi)^2 V_0 + \phi V_{fl} \tag{A.7}$$

APPENDIX B

Supplementary Figures

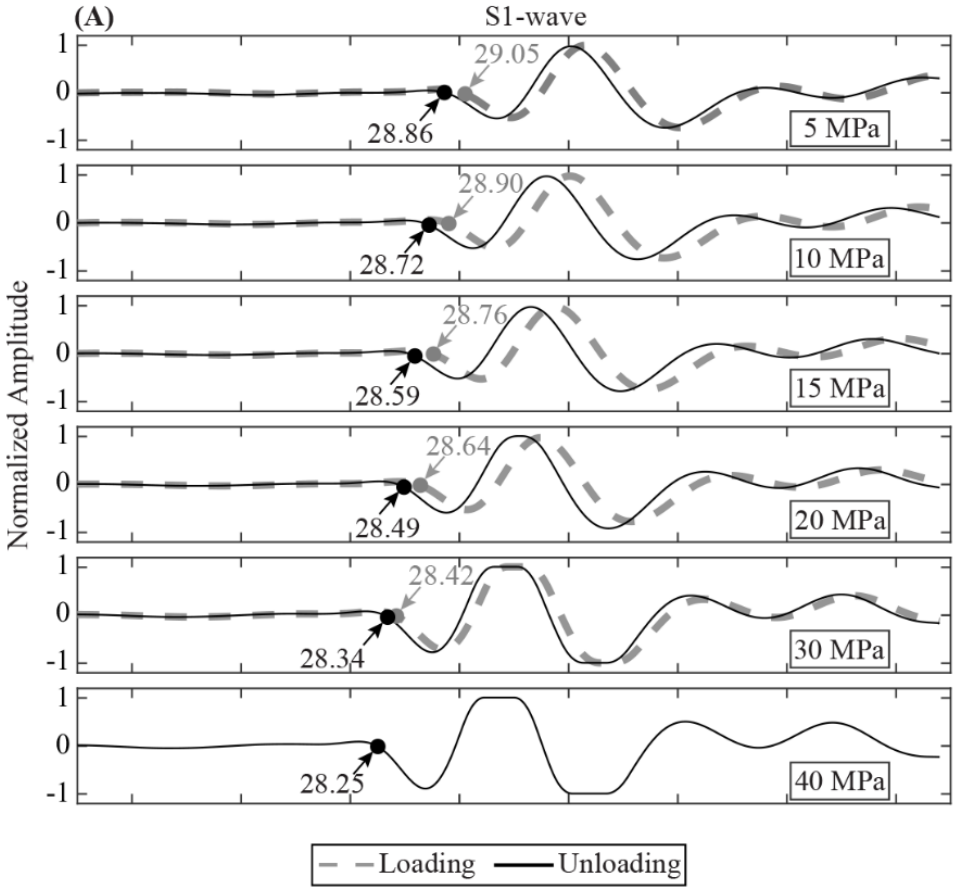

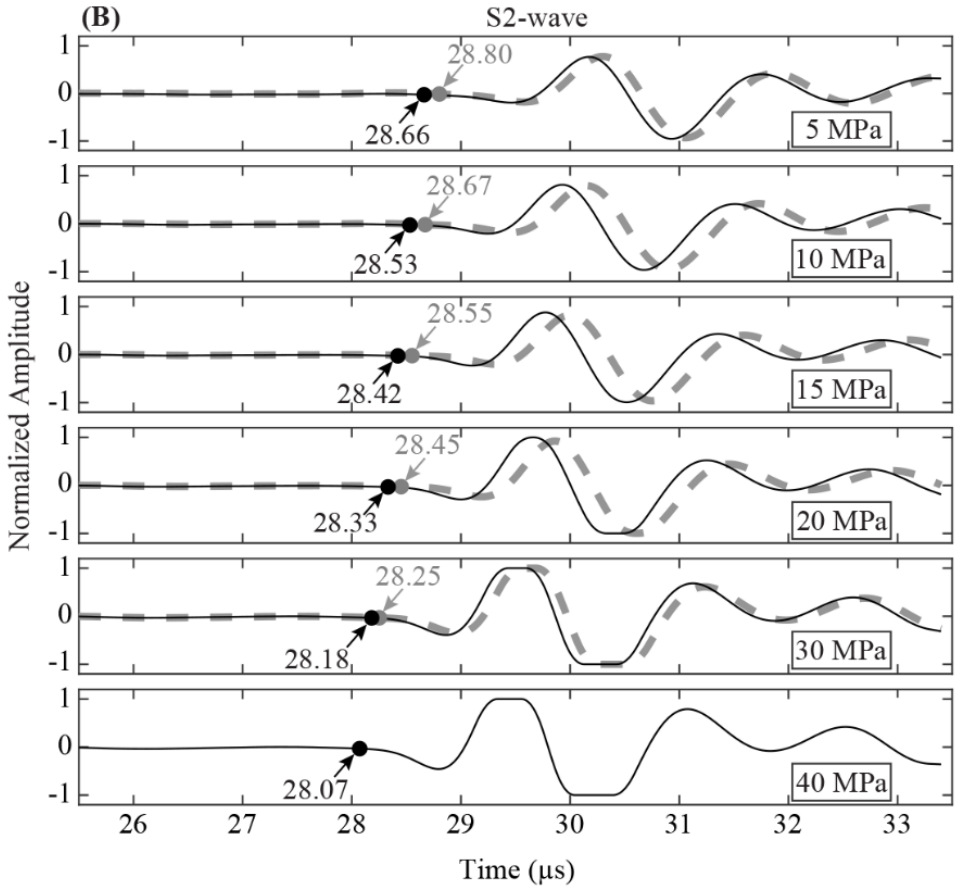

Supplementary Figure S1. S-wave first arrival picking. Representative ultrasonic waveforms for loading (dashed gray) and unloading (solid black) segments of **(A)** S1-wave and **(B)** S2-wave. The corresponding gray and black dots are the interpreted S-wave first arrival times. Confining pressures for individual waveforms are mentioned.

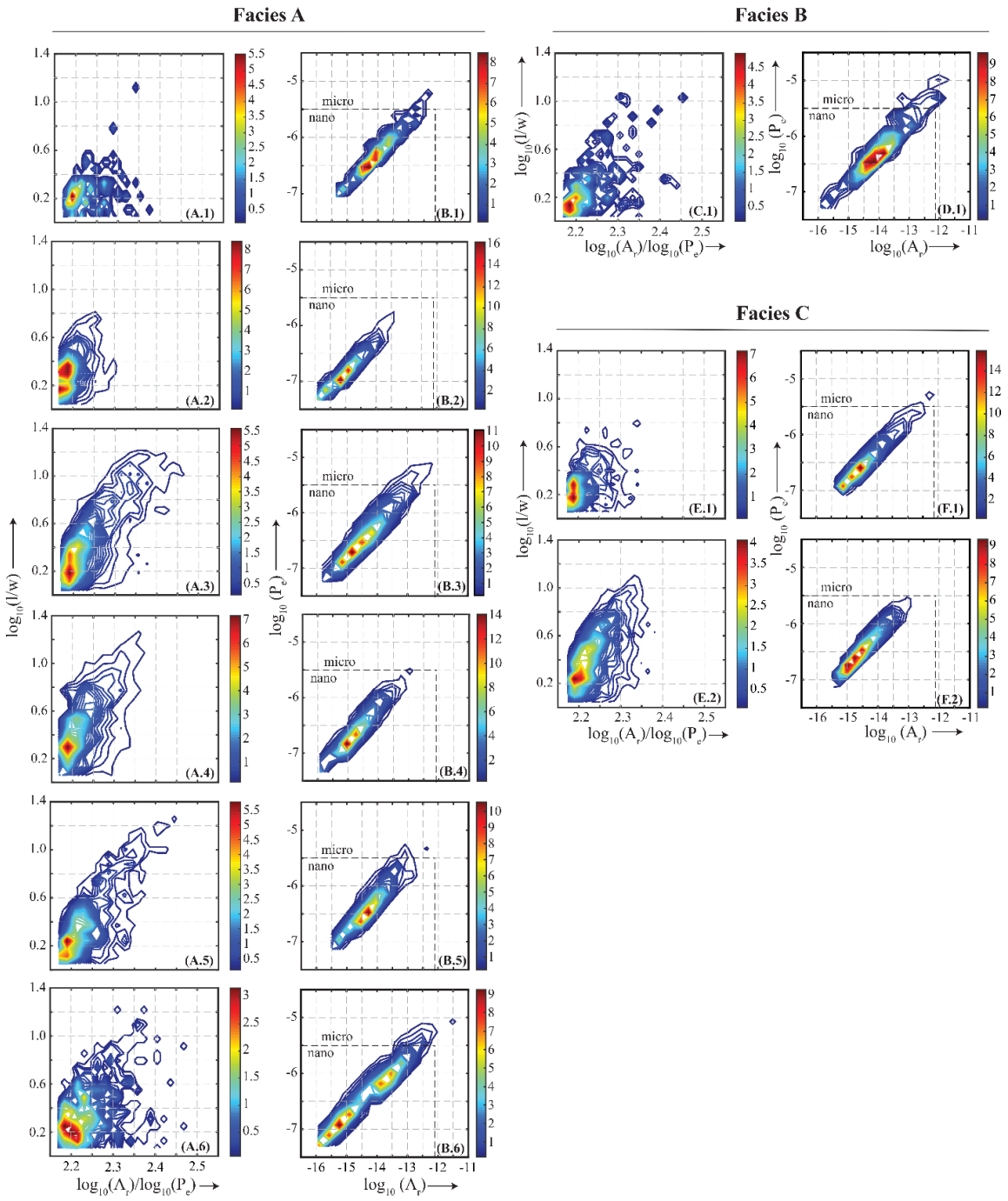

Supplementary Figure S2. Pore-shape and pore-size distribution. Pore length [l], width [w], area [A_r] and perimeter [P_e] data from DIA are plotted as contoured two-dimensional (2D) histogram on log-log scale. In **(A.1-6), (C.1) and (E.1-2)** shows pore-shape distribution where the horizontal axis shows A_r and P_e in the form of $\log_{10}(A_r)/\log_{10}(P_e)$ and vertical axis shows $\log_{10}(l/w)$. A bin size of 20 was found to be optimal for this kind of plot. **(B.1-6), (D.1) and (F.1-2)** shows the pore-size distribution where the horizontal axis shows $\log_{10}(A_r)$ and the vertical axis shows $\log_{10}(P_e)$. A bin size of 15 was found to be optimal for this kind of plot. In **(B.1-6), (D.1) and (F.1-2)**, dashed line separates micro- (1-62.5 µm) and nano- (1 µm-1 nm) pores; and warm color indicates higher pore

population. Sample depth, Φ_{He}, composition and r-value corresponding to P- (r_P), S1- (r_{S1}) and S2- (r_{S2}) waves are mentioned in the table T1. Figure shows the rejected samples that were either dominated with cracks as characterized by high values of both $\log_{10}(A_r)/\log_{10}(P_e)$ and $\log_{10}(l/w)$ or complex pores as characterized by high $\log_{10}(A_r)/\log_{10}(P_e)$ and low $\log_{10}(l/w)$ or samples that are dissimilar in pore type distribution and do not fall in any of the groups within facies.

Table T1: Sample properties of Facies A, B and C containing complex pores.

Facies	Panel	Depth (ft)	Φ_{He} (%)	Quartz (%)	Carbonate (%)	Clay (%)	Others (%)	r_P	r_{S1}	r_{S2}
A	A.1 & B.1	10592.20	1.51	29.6	20.2	31.2	19.0	50.8	13.4	18.9
	A.2 & B.2	10668.20	4.10	34.9	14.7	34.0	16.4	50.9	23.8	21.8
	A.3 & B.3	10420.15	5.14	45.1	9.1	26.9	18.9	80.1	45.1	35.3
	A.4 & B.4	10508.15	1.88	14.0	72.1	8.5	5.4	83.5	30.5	38.4
	A.5 & B.5	10622.25	3.71	46.8	11.6	24.6	17.0	101.3	46.9	56.5
	A.6 & B.6	10590.85	4.20	46.0	21.2	16.6	16.2	165.6	51.7	47.4
B	C.1 & D.1	10710.10	1.05	27.1	62.2	3.5	7.2	96.2	16.4	27.6
C	E.1 & F.1	10570.15	0.73	35.5	50.8	4.5	9.2	43.6	13.7	31.3
	E.2 & F.2	10720.75	1.54	22.9	64.7	3.0	9.4	106.3	37.3	41.8

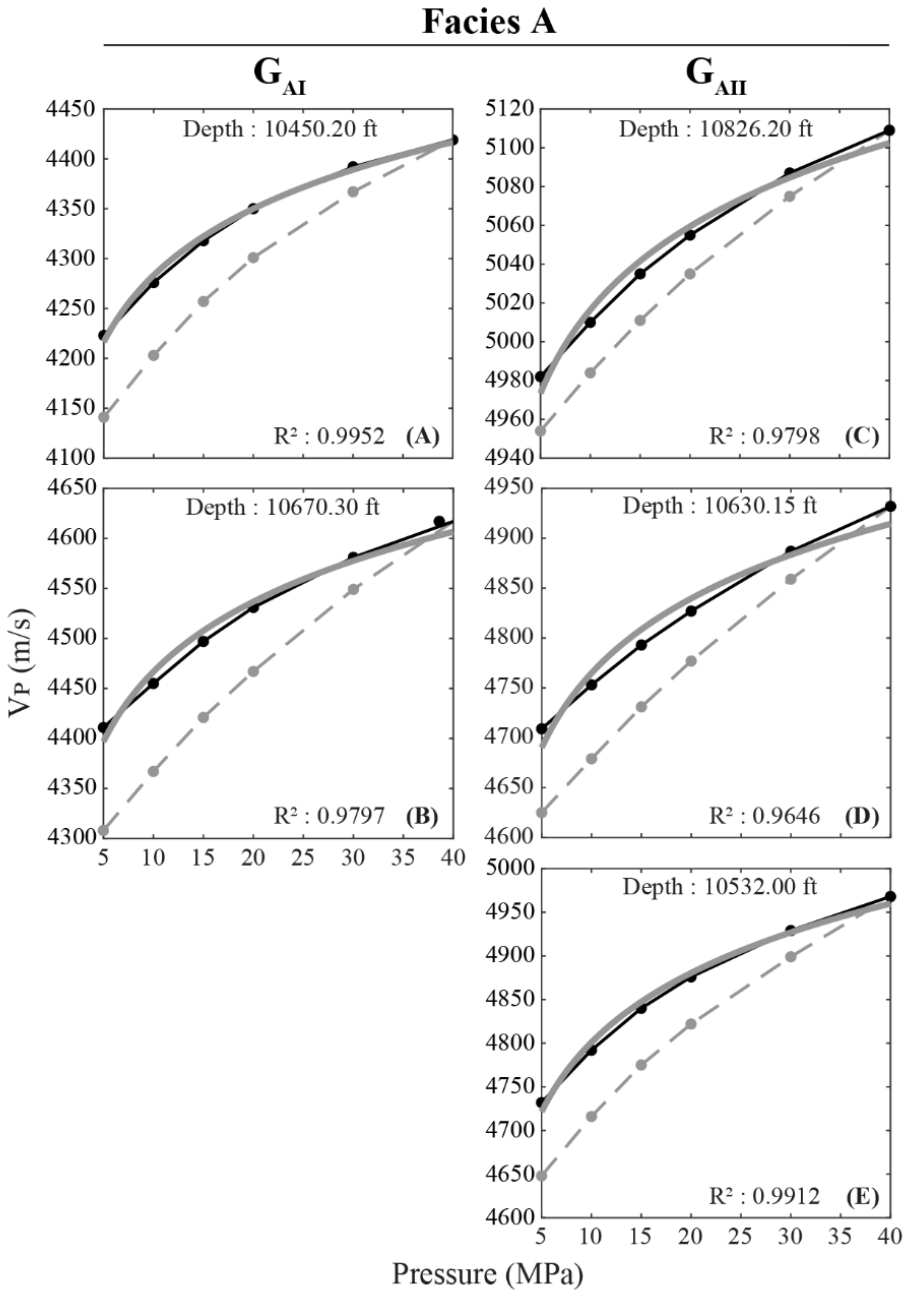

Supplementary Figure S3. P-wave hysteresis. V_P variation over loading and unloading cycle corresponding to Facies A. **(A)** and **(B)** belongs to group G_{AI} and **(C)-(E)** belongs to group G_{AII} of Facies A. **(A)-(E)** show loading and unloading cycle in dashed gray and solid black lines respectively. The thick gray line represents a function of the form $V_P(P_C) = s + r_P \log_{10}(P_C)$ that is fit to the unloading cycle. Depth and R^2 values are mentioned on each hysteresis curve.

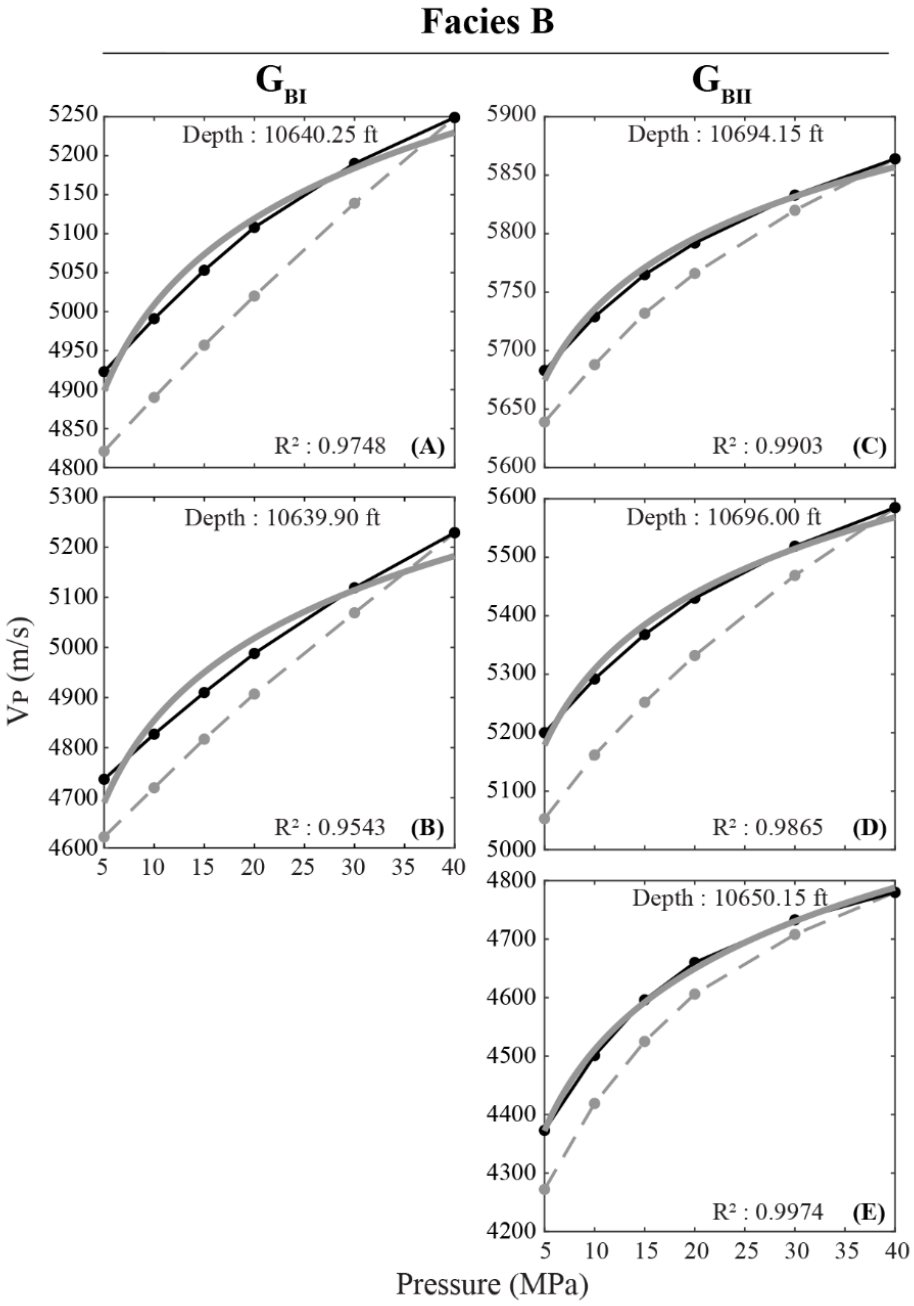

Supplementary Figure S4. P-wave hysteresis. Symbols and labels are same as in Supplementary Figure **S3**. Here, **(A)** and **(B)** belongs to group G_{BI} and **(C)-(E)** belongs to group G_{BII} of Facies B.

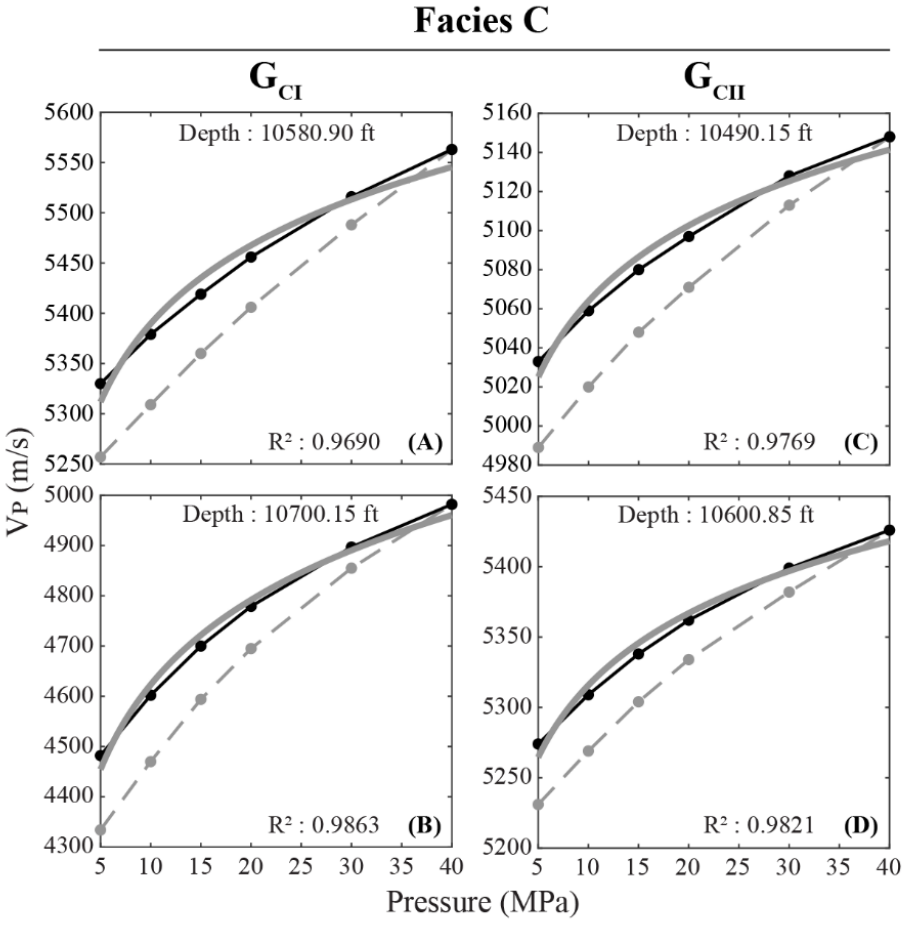

Supplementary Figure S5. P-wave hysteresis. Symbols and labels are same as in Supplementary Figure **S3**. Here, **(A)** and **(B)** belongs to group G_{CI} and **(C)** and **(D)** belongs to group G_{CII} of Facies C.

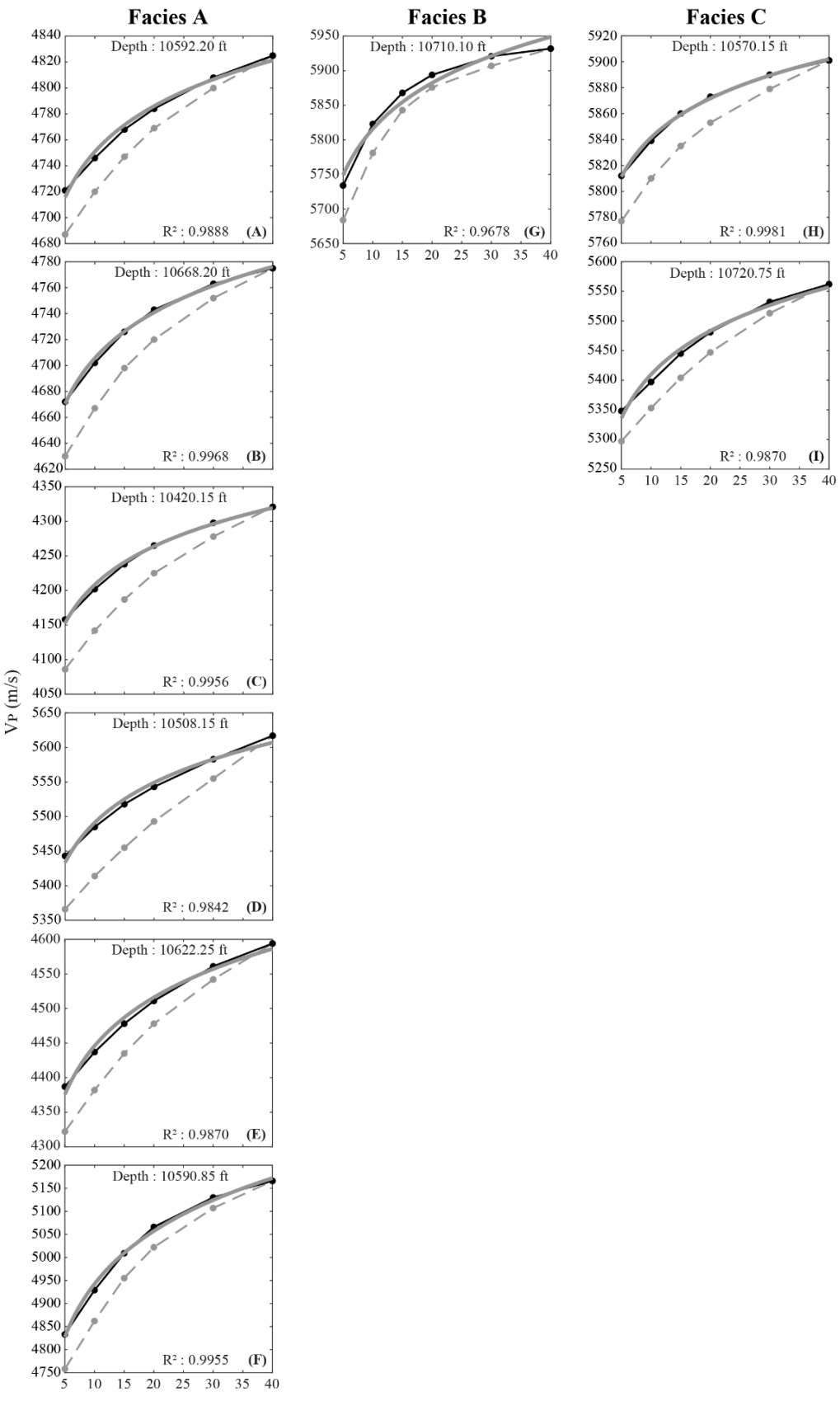
Facies A
Facies B
Facies C
Depth : 10592.20 ft
R² : 0.9888 (A)
Depth : 10668.20 ft
R² : 0.9968 (B)
Depth : 10420.15 ft
R² : 0.9956 (C)
Depth : 10508.15 ft
R² : 0.9842 (D)
Depth : 10622.25 ft
R² : 0.9870 (E)
Depth : 10590.85 ft
R² : 0.9955 (F)
Depth : 10710.10 ft
R² : 0.9678 (G)
Depth : 10570.15 ft
R² : 0.9981 (H)
Depth : 10720.75 ft
R² : 0.9870 (I)
VP (m/s)
Pressure (MPa)

Supplementary Figure S6. P-wave hysteresis. Symbols and labels are same as in Supplementary Figure **S3**. Here, **(A)-(F)** belongs to Facies A, **(G)** belongs to Facies B and **(H)-(I)** belongs to Facies C.

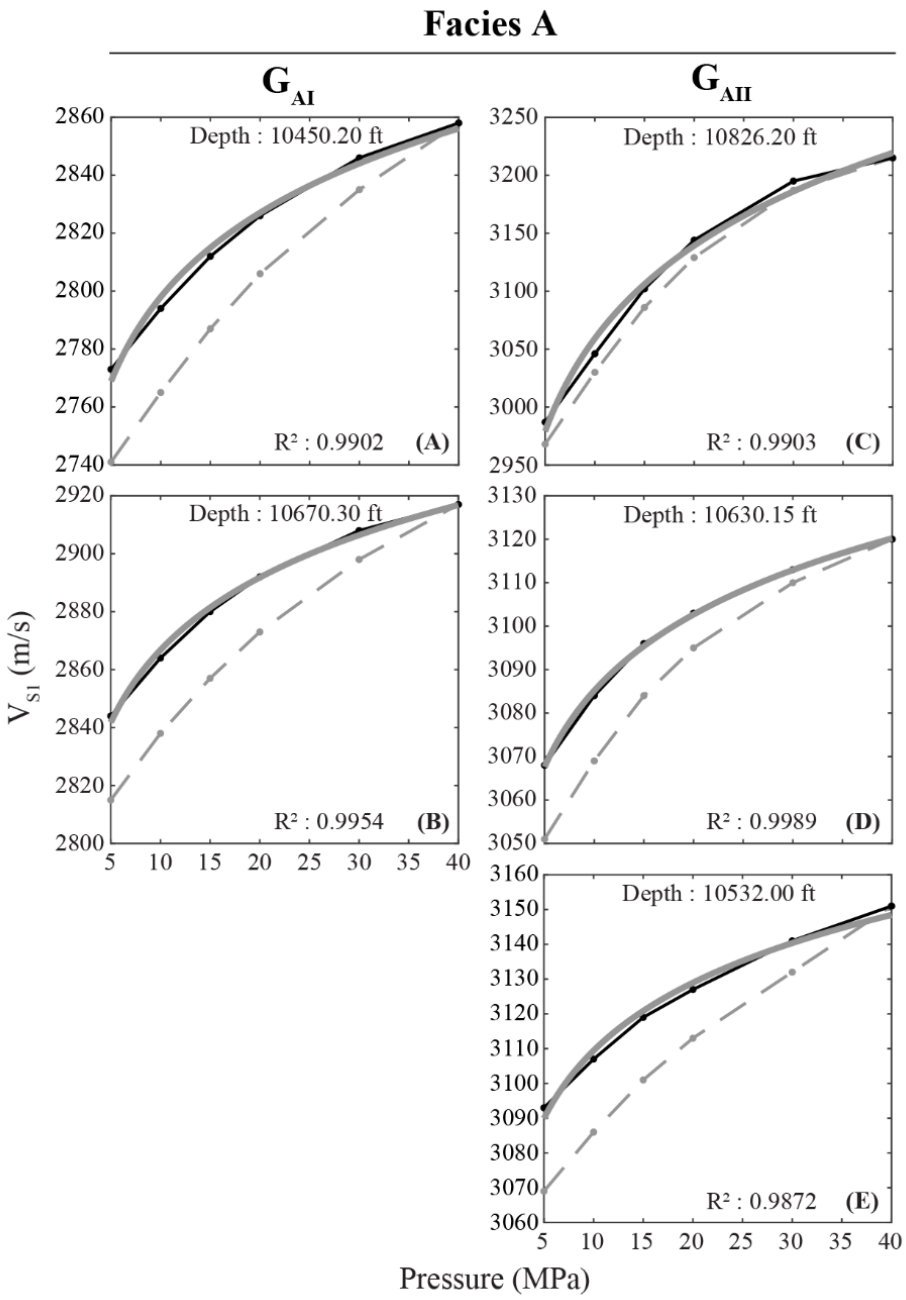

Supplementary Figure S7. S1-wave hysteresis. V_{S1} variation over loading and unloading cycle corresponding to Facies A. **(A)** and **(B)** belongs to group G_{AI} and **(C)-(E)** belongs to group G_{AII} of Facies A. **(A)-(E)** show loading and unloading cycle in dashed gray and solid black lines respectively. The thick gray line represents a function of the form $V_{S1}(P_C) = s + r_{S1} \log_{10}(P_C)$ that is fit to the unloading cycle. Depth and R^2 values are mentioned on each hysteresis curve.

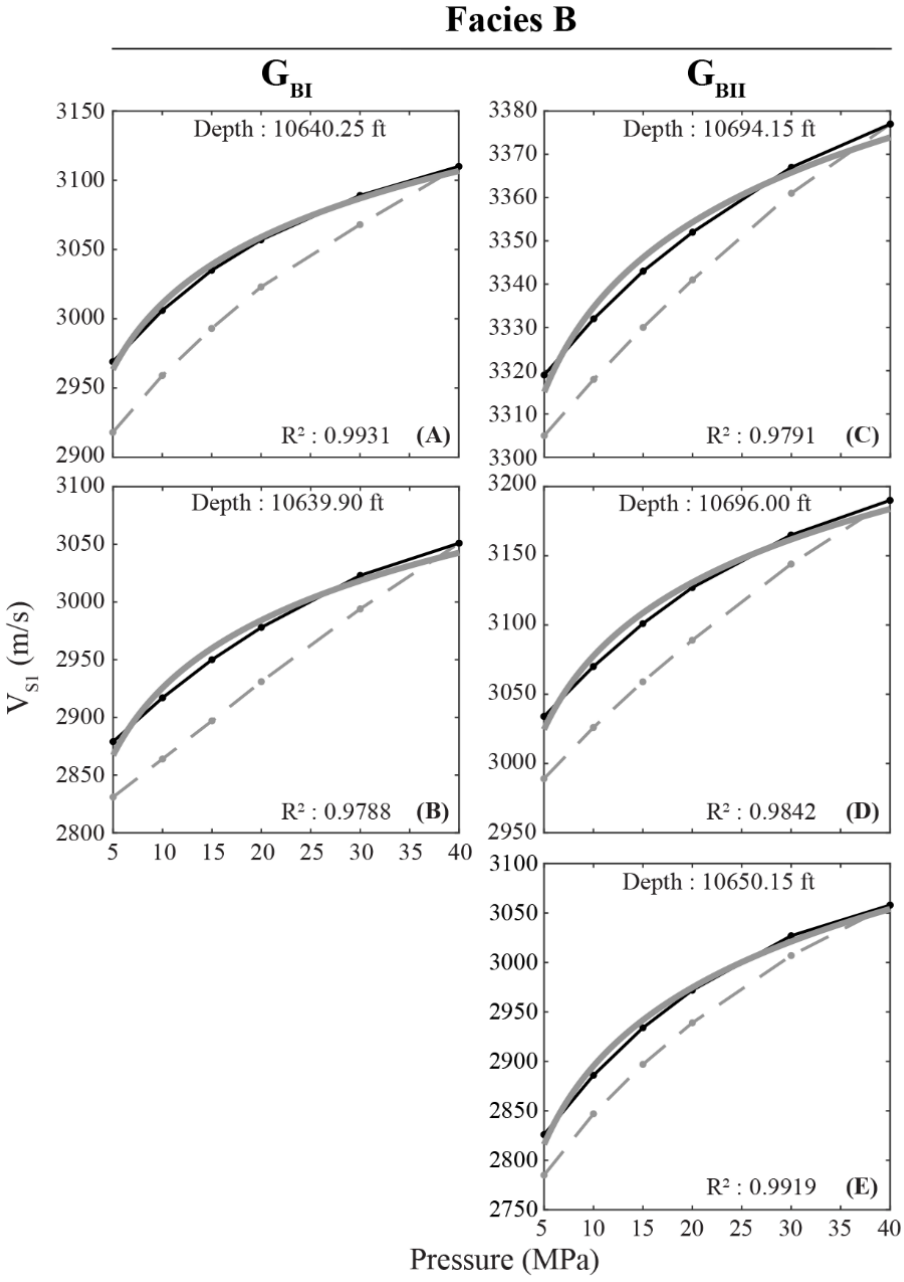

Supplementary Figure S8. S1-wave hysteresis. Symbols and labels are same as in Supplementary Figure **S7**. Here, **(A)** and **(B)** belongs to group G_{BI} and **(C)-(E)** belongs to group G_{BII} of Facies B.

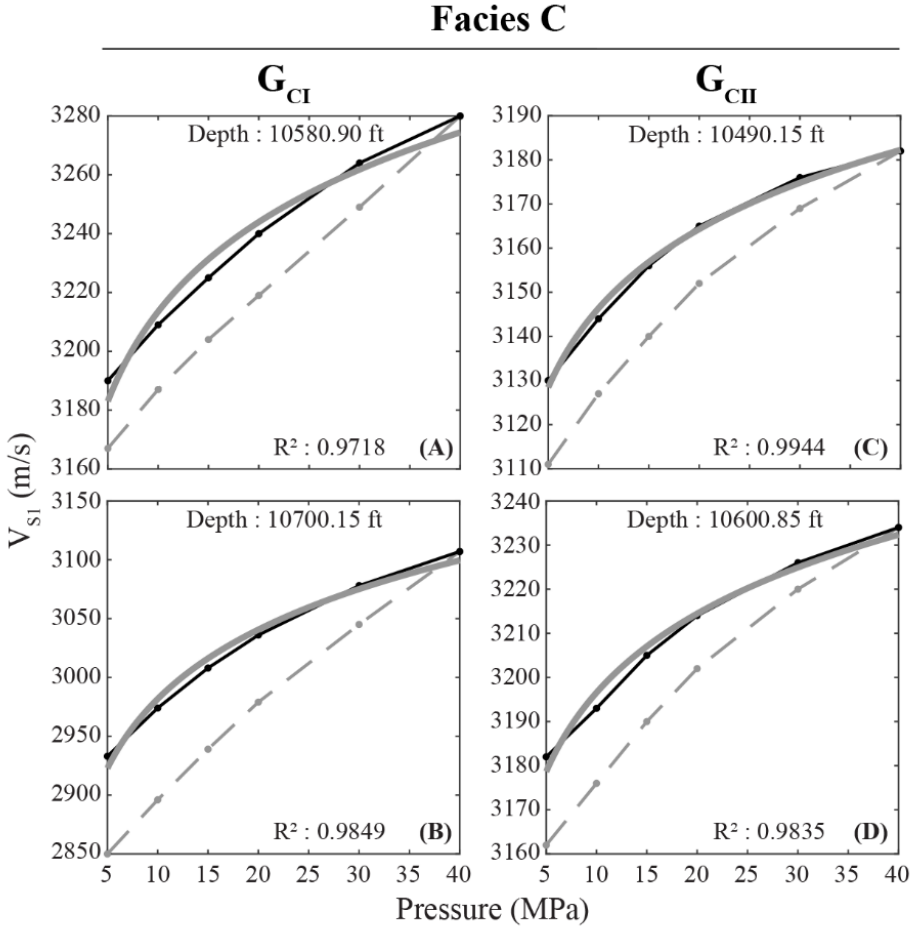

Supplementary Figure S9. S1-wave hysteresis. Symbols and labels are same as in Supplementary Figure **S7**. Here, **(A)** and **(B)** belongs to group G_{CI} and **(C)** and **(D)** belongs to group G_{CII} of Facies C.

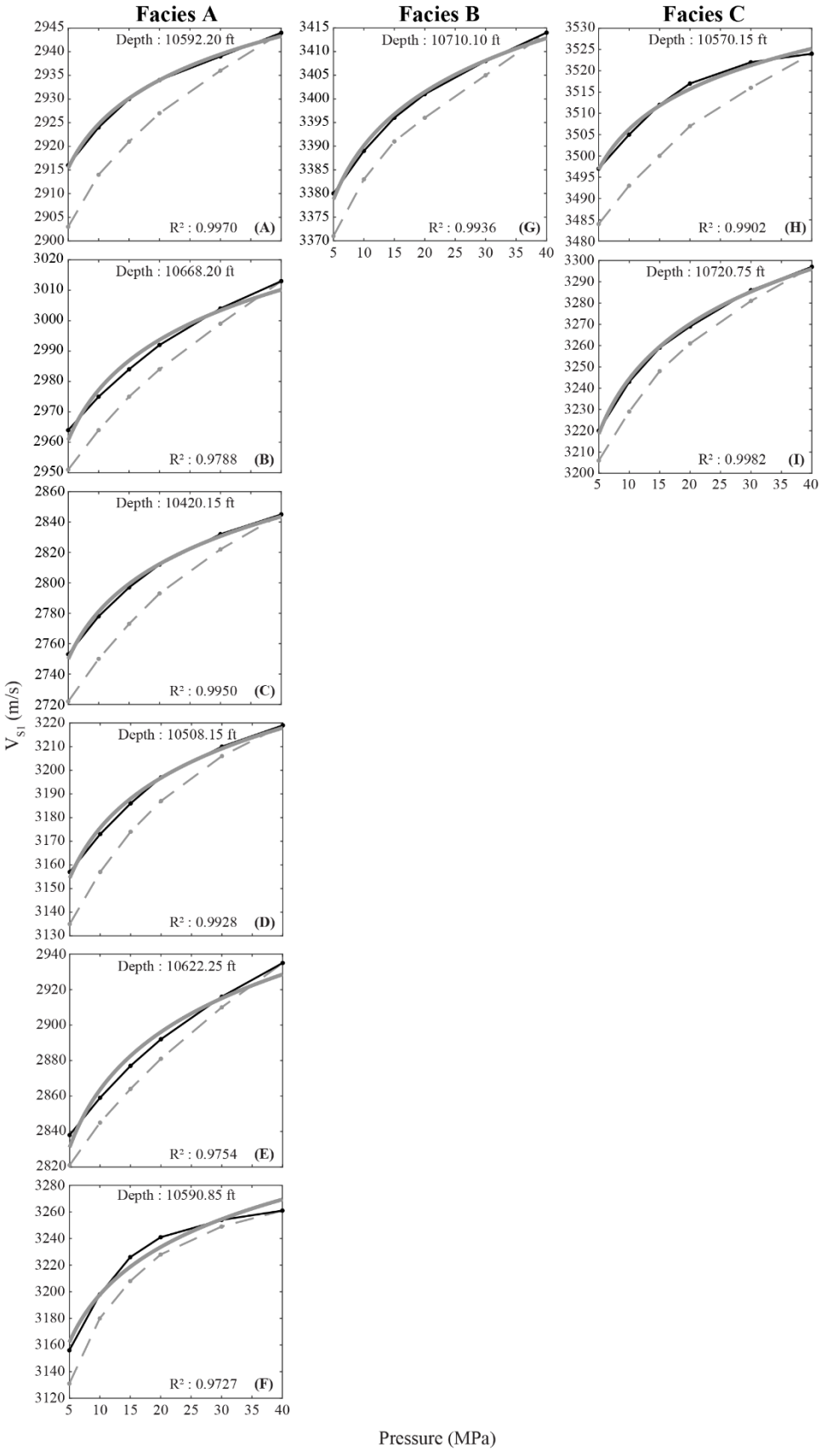
Facies A
Facies B
Facies C
Depth : 10592.20 ft
R² : 0.9970 (A)
Depth : 10710.10 ft
R² : 0.9936 (G)
Depth : 10570.15 ft
R² : 0.9902 (H)
Depth : 10668.20 ft
R² : 0.9788 (B)
Depth : 10720.75 ft
R² : 0.9982 (I)
Depth : 10420.15 ft
R² : 0.9950 (C)
Depth : 10508.15 ft
R² : 0.9928 (D)
Depth : 10622.25 ft
R² : 0.9754 (E)
Depth : 10590.85 ft
R² : 0.9727 (F)
V_{S1} (m/s)
Pressure (MPa)

Supplementary Figure S10. S1-wave hysteresis. Symbols and labels are same as in Supplementary Figure **S7**. Here, **(A)-(F)** belongs to Facies A, **(G)** belongs to Facies B and **(H)-(I)** belongs to Facies C.

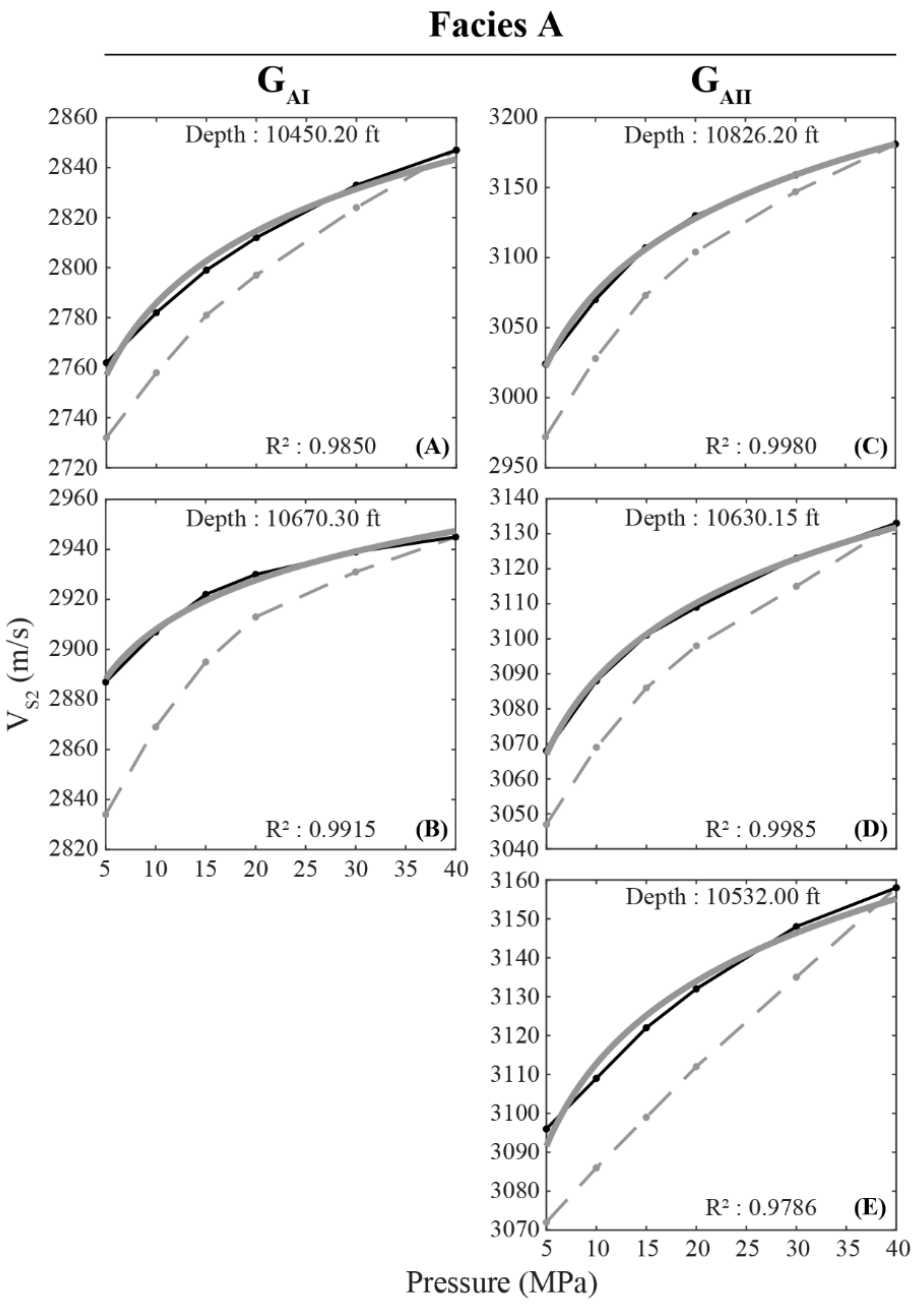

Supplementary Figure S11. S2-wave hysteresis. V_{S2} variation over loading and unloading cycle corresponding to Facies A. **(A)** and **(B)** belongs to group G_{AI} and **(C)-(E)** belongs to group G_{AII} of Facies A. **(A)-(E)** show loading and unloading cycle in dashed gray and solid black lines respectively. The thick gray line represents a function of the form $V_{S2}(P_C) = s + r_{S2} \log_{10}(P_C)$ that is fit to the unloading cycle. Depth and R^2 values are mentioned on each hysteresis curve.

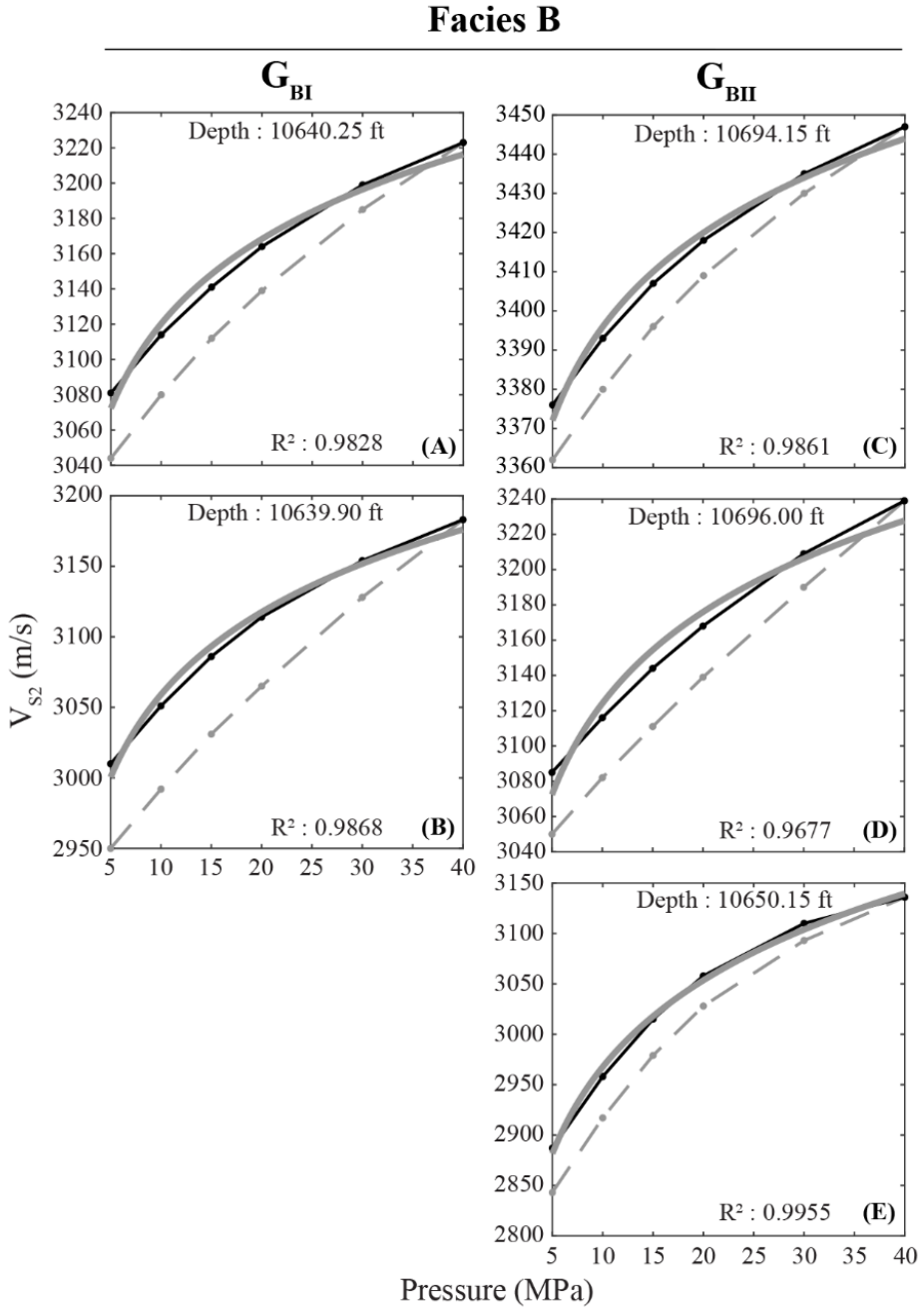

Supplementary Figure S12. S2-wave hysteresis. Symbols and labels are same as in Supplementary Figure **S11**. Here, **(A)** and **(B)** belongs to group G_{BI} and **(C)-(E)** belongs to group G_{BII} of Facies B.

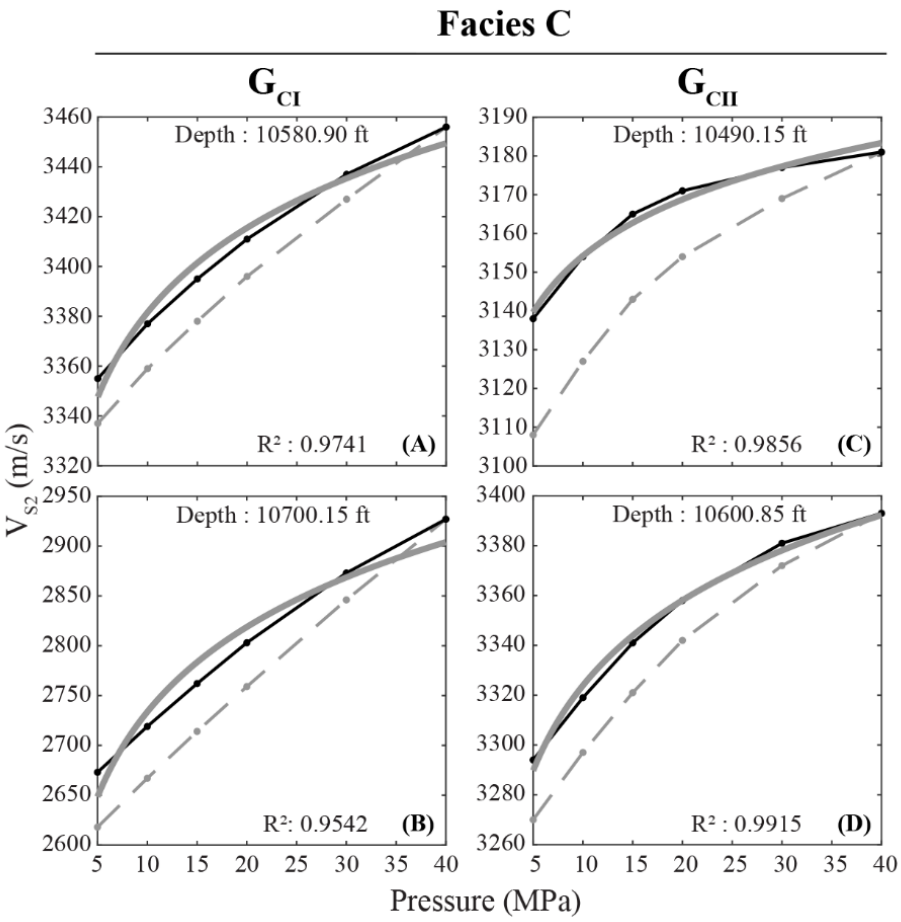

Supplementary Figure S13. S2-wave hysteresis. Symbols and labels are same as in Supplementary Figure **S11**. Here, **(A)** and **(B)** belongs to group G_{CI} and **(C)** and **(D)** belongs to group G_{CII} of Facies C.

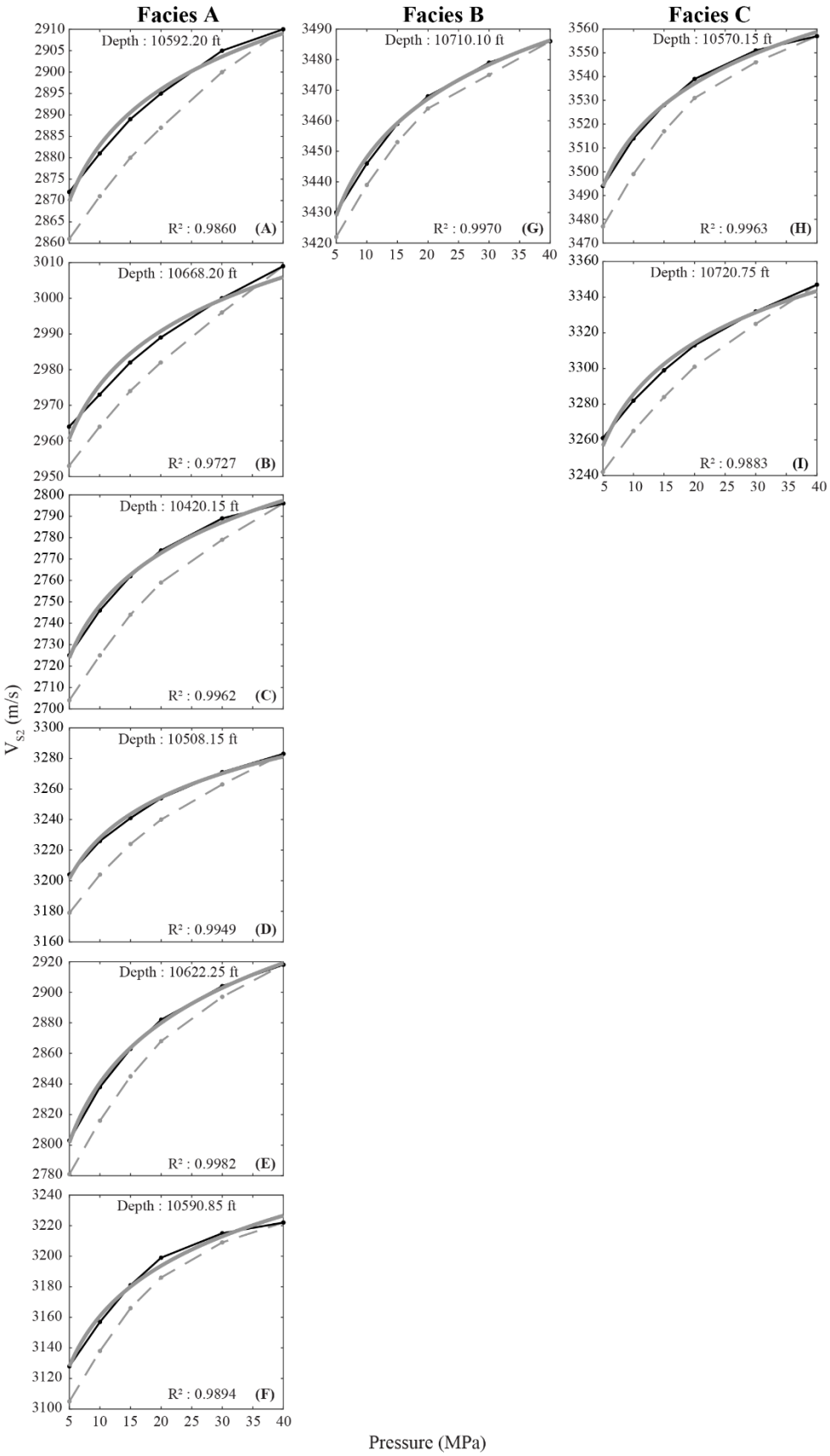
Facies A
Facies B
Facies C
Depth : 10592.20 ft
R² : 0.9860 (A)
Depth : 10710.10 ft
R² : 0.9970 (G)
Depth : 10570.15 ft
R² : 0.9963 (H)
Depth : 10668.20 ft
R² : 0.9727 (B)
Depth : 10720.75 ft
R² : 0.9883 (I)
Depth : 10420.15 ft
R² : 0.9962 (C)
Depth : 10508.15 ft
R² : 0.9949 (D)
Depth : 10622.25 ft
R² : 0.9982 (E)
Depth : 10590.85 ft
R² : 0.9894 (F)
V_{S2} (m/s)
Pressure (MPa)

Supplementary Figure S14. S2-wave hysteresis. Symbols and labels are same as in Supplementary Figure **S11**. Here, **(A)-(F)** belongs to Facies A, **(G)** belongs to Facies B and **(H)-(I)** belongs to Facies C.

VITA

Rohit Raj

Candidate for the Degree of

Doctor of Philosophy

Thesis: NANOPORE ARCHITECTURE AND ELASTIC VELOCITIES IN THE MISSISSIPPIAN-AGE CARBONATE-SILICICLASTIC RESERVOIRS OF THE US MID-CONTINENT

Major Field: Geology

Biographical:

Education:

Completed the requirements for Doctor of Philosophy in Geology at Oklahoma State University, Stillwater, Oklahoma in December, 2021.

Completed the requirements for Integrated Master of Technology in Geophysical Technology at Indian Institute of Technology Roorkee, Roorkee, India in 2016.

Experience:

Employed as Graduate Research/Teaching Associate by Boone Pickens School of Geology, Oklahoma State University from August 2016 to December 2021.

Professional Memberships:

Society of Exploration Geophysicists (student member)
American Association of Petroleum Geologists (student member)